Stellar Occultations by Bodies in the Outer Solar System at the South African Astronomical Observatory

Anja Genade

Thesis presented for the degree of Master of Science
In the Department of Astronomy
University of Cape Town
December 2017

South African Astronomical Observatory
Cape Town
South Africa

Supervisors: Dr. A. A. Sickafoose and Dr. S. Mohamed

Abstract

Information on the origin and evolutionary processes of the Solar System is harbored by primitive bodies called trans-Neptunian objects (TNOs). Their preserved state is due to these bodies having orbits at and beyond that of Neptune, as this specific area is considered to be the least thermally modified in the Solar System and could contain a large population of primordial remnants. These archaic remnants not only provide us with information on our infant Solar System, but also improve our understanding of extrasolar planetary formation processes. Stellar occultations by TNOs enable the determination of sizes and shapes with kilometric accuracy (confining albedos, leading us to compositions and densities), the detection of atmospheres down to pressures of a few nanobars, as well as an investigation of the immediate vicinity of the target body (indicating the presence of rings, satellites, jets, comas). These TNOs roam the icy outskirts of our Solar System which, together with their small sizes, make them faint and their stellar occultations short-lived. With a duration ranging from a couple of seconds for small bodies up to a few hundreds of seconds for the larger TNOs, specific imaging cameras combined with Global Positioning devices and optical telescopes, ensure the fast-cadence capture of these events with microsecond timing accuracy. This high-time resolution observing in combination with the relative speed of the star and the occulting body ensures accurate results with resolutions down to the kilometric-level, which overthrows the resolvability of ground-based telescopes and rivals that of space probes.

Here, we present work done by the South African Astronomical Observatory (SAAO) stellar occultation observing program during the period of July 2016 - July 2017. Specifically, we describe the telescopes, instruments and data analysis pipelines that are used for the SAAO stellar occultation program. The stellar occultation results are obtained from the slightly modified, data reducing SHOC pipeline as originally developed by Dr. Marissa Kotze. The SHOC pipeline laid the groundwork for two additional pipelines to be developed and therefore the MORIS instrument on the 3-m IRTF as well as the FLI autoguider cameras mounted on multiple 1-m LCO telescopes are included to provide many opportunities to observe the predicted stellar occultations. These pipelines include reduction features, correct and accurate derivation of timing information, optimization of the signal-to-noise ratio (SNR) through aperture corrected photometry and most important, provide the user with light curve plots of the point sources. The light curves are normalized and individually analyzed for any signs of a positive stellar occultation detection while testing the effects of reduction on the SNR. This is followed by checking the statistical distribution of the data as well as determining a few values for the line-of-sight optical depth. Instrumental deadtimes for the LCO guider cameras are calculated to effectively determine and use time allocated through proposals.

Finally, a single positive stellar occultation by Orcus was observed on 7 March 2017 from two separate sites. Here, chord length calculations as well as timing offsets are calculated from the normalized light curves which led to a possible detection of both Orcus and Orcus's satellite, Vanth. An in depth discussion is provided to justify this reasoning. This thesis serves to characterize and consolidate the now well-established program of stellar occultation observations at the SAAO.

Acknowledgements

Firstly, I would like to express my utmost gratitude to my supervisor Dr. Amanda Sickafoose for the continuous support of my MSc study and related research, for her patience, motivation, and immense knowledge. Her guidance helped me in all the time of research and writing of this thesis. I could not have imagined having a better supervisor for my MSc study, so thank you for giving me this opportunity.

Besides my supervisor, I would also like to thank my co-supervisor, Dr. Shazrene Mohamed for her insightful comments and encouragement, not just in terms of research but also on managing life with studies. To Dr. Nicolas Erasmus for being a very entertaining co-observer on frosty nights as well as being a calming presence throughout my research and related responsibilities.

My sincere thanks also goes to the National Astrophysics and Space Science Programme, the South African Astronomical Observatory, the University of Cape Town and the National Research Fund, who provided me with the financial support needed to do my research otherwise not possible. Also, for creating an opportunity that would change my academic career for the remainder of my life. I am eternally grateful for the opportunities they have presented me with throughout my studies.

I thank my fellow classmates for the stimulating discussions, for the sleepless nights we were working together before deadlines, and for all the fun we have had in the last couple of years. Also, I thank my friends Ethan, Michael S., Michael H., Jamie, Dineo/Isabella, Bianca, Lennox and Nico for all of the support as well as motivational speeches received on numerous occasions. Special thanks goes to Nicole for always being willing to help me in times of discouragement, for giving me space and also for not giving me space. You have become a dear friend and your undying support has not been overlooked. To Joost, you only saw the last few months of this process but managed to support me in ways I thought were not possible. Thank you for being unwavering in your words, motivation, inspiration and love.

Last but not the least, I would like to thank my family: my mom, Karin; my brother, Jan; my sister, Prisca and the rest of my family for always supporting me throughout writing this thesis and my life in general. Precious advice and support was given throughout my studies and even though they were given from 1000 kilometers away, never seemed to diminish over distance. My family has been my number one supporters from the very beginning, believing in me without any limits and reigniting my passion for Astrophysics with their continuous curiosity of the field. I love you all and I dedicate the completion of this thesis to you.

Plagiarism Declaration

I, Anja Genade, know the meaning of plagiarism and declare that all of the work in this document, save for which is properly acknowledged, is my own.

Contents

1 Introduction

The Solar System has been in existence for about 4.6 billion years but the details about its formation and evolutionary process have yet to be devised with absolute certainty. Only by knowing the earliest available particulars of our Solar System can we start to conceive all possibilities that led to our present state of bodies such as planets, dwarf planets, satellites, asteroids, meteors and other smaller bodies orbiting our G-type, main-sequence Sun. Solar evolution caused thermal changes within the inner region accompanied by gravitational effects from the larger planets, creating regions in space which would not contain many remnants of our once infant Solar System, pushing our search for fossil-like bodies further out in the Solar System region where these environmental effects are less dominant. The study of this region about 25 years ago led to the discovery of 1992 QB_1 (Jewitt & Luu, 1993), the first body found to orbit the Sun beyond that of Pluto and hence the first detection of a Kuiper Belt object (although Pluto was the first but was not recognized as such at the time). This discovery inaugurated the Kuiper Belt, which could then be defined as a desolate region located on the outskirts of our Solar System which spans from 30 to 50 times the distance between the Earth and the Sun.

Since then about 1500 various icy bodies have been discovered in the outer Solar System, but a fundamental property such as the mass of the Kuiper Belt has yet to be confirmed (e.g. Kenyon & Bromley, 2004; Delsanti & Jewitt, 2006). With much of the Solar System's mass being contained within the Sun and the orbiting planets, the question arises about how much leftover mass is contained within the Kuiper Belt's archaic inhabitants that tell the chemical, dynamical as well as the thermal story of our Solar System. Knowledge gained by studying these primitive bodies does not only assist in our understanding of the Solar System's origin and evolutionary path, but also the formation processes involved in extrasolar planets.

The catch: with great distance comes a great deal of observational challenges. Trans-Neptunian objects (TNOs) are bodies not defined as a planet nor exclusively classified as a comet with orbits $>$30 AU. They have an average magnitude of $\sim$23.6 as detected by the Outer Solar System Origins Survey (OSSOS; Bannister et al., 2016) which has magnitude sensitivity ranging around $\sim$24 for the various motion rates of these bodies. These bodies therefore require either direct diameter measurements to be made through optically resolved observations or, in addition with thermal infrared observations, diameters can be estimated by using a thermal model (with the related uncertainties mentioned below). For two decades these objects have been studied through visible, near-infrared, and thermal photometry and spectroscopy (e.g. Stansberry et al., 2008; Santos-Sanz et al., 2009; Brown, 2012; Lellouch et al., 2013). Near-infrared refers to wavelengths closer to that of the visible wavelengths, and together with the latter is used to study the spectra of these bodies ranging from neutral colors to more red colors (e.g. Barucci & Peixinho, 2005; Gulbis et al., 2006). Thermal measurements refer to wavelengths in the far-infrared region of the spectrum as thermal has to do with the actual temperature of the body and is used for size estimations. These bodies are very cold and their black body radiation peaks in the far-infrared making ground-base observations impossible due to the Earth's atmosphere. The short-wavelength tail of the black body radiation, however, can be observed from the ground at the visible as well as near-infrared wavelengths. There are large uncertainties associated with the physical quantities (diameter, albedo and density; e.g. Santos-Sanz et al., 2016) derived through the visible, near- and far-infrared observing methods. The radiometric technique applied to Spitzer and Herschel observations (e.g. Stansberry et al., 2008; Lellouch et al., 2013) provides, at best, a 10% accuracy in diameter and

20% in albedo which constrains the accuracy in size determinations as well as the intrinsic matter composition of these bodies. The latter mentioned uncertainties are also transferred further in the case of binaries where Kepler's law is used and result in a 30% density uncertainty. These uncertainties limit the detailed study of the physical and chemical properties of these bodies significantly.

More certainty in these values is required, but even the largest available Earth-based telescopes would not be able to probe the detailed specifics of these bodies and systems using these methods. Thus, an observing technique that results in adequate spatial resolution capable of resolving the various physical characteristics and features of TNOs, is essential. Such a technique, called stellar occultations, does exist and allows the much needed spatial resolution unrivaled by any other Earth-based method and enables the study of TNOs and their immediate surroundings with an optimal size and shape accuracy of about 0.1% (e.g. Sicardy et al., 2011; Ortiz et al., 2012). Lowering the uncertainty for the diameter measurements corresponds to a lowering of the uncertainty associated with the density (the latter would involve mass derivations using Kepler's Third Law and requires a satellite to be present) which is vital when studying the interiors of these bodies. This technique is therefore a powerful tool to study these tiny objects within the outer Solar System where faintness and small angular diameters tend to constrain any further optical exploration. According to NASA's Jet Propulsion Laboratory (JPL) Small-Body Database Search Engine[1], which lists a total of 2412 TNOs with orbital semi-major axes from 30.11 to 2636 AU, H-magnitude range from 19.4 to -1.1 magnitudes and diameters range from a few kilometers to a few thousands of kilometers. Albedo diversity is also common with TNOs and can range from $\sim$ 0.03 for dark TNOs to $\sim$0.96 for bright TNOs (e.g. Sicardy et al., 2011). Almost 200[2] of the known TNOs have derived diameters and albedos. This equates to less than 10% of the total known amount of TNOs and is indicative that a significant amount of TNOs still need to be physically (size, albedo, density etc.) constrained. Every positive detection of a stellar occultation made by a TNO provides unique information that would not be possible with any other method besides sending a spacecraft.

Whilst stellar occultations are few and far between, ongoing studies incorporating the refinements offered by the Large Synoptic Survey Telescope (LSST) would increase the frequency of stellar occultations as well as our knowledge about the occulting TNOs greatly. Ongoing stellar occultation studies as well as a possible undiscovered ninth planet (e.g. Brown & Batygin, 2016), not only justify but also place the ongoing study of outer Solar System bodies in perspective.

Here we present the work done by the South African Astronomical Observatory (SAAO) on stellar occultations using specialized equipment such as the autoguider cameras from the 1-m telescopes of the Las Cumbres Observatory (LCO) (Brown et al., 2013) network[3], Massachusetts Institute of Technology Rapid Imaging System (MORIS) (Gulbis et al., 2011) on NASA's 3-m InfraRed Telescope Facility (IRTF)[4] and the Sutherland High-speed Optical Cameras (SHOC) (Coppejans et al., 2013) mounted on the SAAO's 74- and 40-in telescopes as well as the 1-m telescope[5].

[1] https://ssd.jpl.nasa.gov/ - Retrieved 6 November, 2017.
[2] http://www.johnstonsarchive.net/astro/tnodiam.html - Retrieved on 1 December, 2017.
[3] Dr. T. Lister of Las Cumbres Observatory executed these non-standard observations done with the guide cameras on the 1-m telescopes.
[4] Dr. A.A. Sickafoose, visiting Astronomer at the Infrared Telescope Facility, which is operated by the University of Hawaii under contract NNH14CK55B with the National Aeronautics and Space Administration
[5] Named according to the diameter of their primary mirrors which is in either inches or meters. The SAAO telescopes are therefore known as the 74 inch, the 40 inch and the new 1-m telescope, which is still under commissioning and is officially known as Lesedi.

The remainder of this section focuses on the background of stellar occultations, the scientific motives and aims for studying the TNOs covered in this thesis from the predicted events we observed, with brief overviews on the time-domain imagers used, and how they were used, to capture these short-lived events.

1.1 Background

A stellar occultation occurs when an intervening body blocks the light from a background star from reaching an observer, either by dimming or blocking the incoming signal for a time duration ranging from less than a second for tiny TNOs to hours for larger planets. With a light source illuminating the backside of an occulting body, it would naturally cast a shadow path that sometimes falls over the Earth. The size and shadow pathway traced out on the Earth depend on the geometry specifics of the stellar occultation like the astrometric positions of the background star and the occulting body together with its size and distance.

The orbital periods of these bodies, however, are typically hundreds of years with the orbital positions as recorded for the past few years of the larger TNOs only equating to a small percentage of the entire orbit. An intensive program at MIT (Zuluaga et al., 2011) has been dedicated to refining the astromteric locations of both the candidate star as well as the occulting body in order to predict stellar occultations and to reduce the margin of error in these predictions (e.g. Assafin et al., 2010).

The outer Solar System bodies studied through stellar occultations in this thesis are:

- Dwarf planets - bodies with suitable shapes that support hydrostatic equilibrium but as of yet, have not cleared the direct environment surrounding their orbits.
- Centaurs - bodies that orbit the Sun at average distances between Jupiter and Neptune. The giant planets perturb these bodies and cause them to have unstable orbits. As the name suggests, these bodies can behave like both comets and asteroids.
- Trans-Neptunian Objects (TNOs) - bodies orbiting the Sun with average orbits at and beyond that of Neptune ($\sim$ 30 AU). Subclasses include: classical bodies with low inclined, almost circular orbits that are free from any significant perturbations from Neptune; resonant bodies that are in orbital resonance with Neptune causing orbits to be more inclined and elliptical than those of the classical bodies but less than the scattered bodies; scattered bodies with highly inclined, elliptical orbits due to gravitational scattering and perturbations from the larger planets.

When talking about the occulting body in this thesis it refers to any one of the above listed outer Solar System bodies.

The bodies studied here have orbital distances $>$ 30 AU (excluding Centaurs at orbital distances $<$ 30 AU), and are small in size (typically less than $\sim$900 km excluding a few larger bodies such as Haumea and Pluto which are $>$ 2000 km in diameter), which results in angular diameters that are typically in the order of tenths of arcseconds. It therefore comes as no surprise that stellar occultations not only happen very seldom but are very short in duration as well. These short-lived events however provide unique information of the occulting body otherwise not obtainable through other observing techniques.

Stellar occultations are capable of spatial resolutions unmatched by any other Earth-based method, because this method simply does not rely on resolving the occulting body as they are in most cases much too small and faint, but rather focuses on analyzing the significant fluctuations in stellar flux caused by the occulting body. Thus the spatial resolution provided by stellar occultations allow the physical properties to be probed and studied (size, albedo, composition and density) together with immediate surroundings (the presence of an atmosphere, rings, jets, comas, satellites, or debris). Size determination with kilometric accuracy (confining albedos, providing insight into composition and densities; e.g. Davis et al., 2014; Braga-Ribas et al., 2013; Elliot et al., 2010), the detection of atmospheres with atmospheric pressures as little as a few nanobars (e.g. Ortiz et al., 2012; Sicardy et al., 2006, 2011; Sickafoose et al., 2015; Olkin et al., 2014; Person et al., 2012) and analyzing their direct close environment with the same sensitivity for the detection of any features such as rings (e.g. Ortiz et al., 2015, 2017; Braga-Ribas et al., 2014), satellites, jets and comas (e.g. Elliot et al., 1995; Bus et al., 1996; Ruprecht et al., 2015), can be achieved with this powerful technique. Our scientific goals for the individual bodies researched through stellar occultations are discussed in the section that follows.

1.2 Scientific justification and goals for predicted events

Information gathered through stellar occultations for the respective bodies covered in this thesis is summarized below. If no stellar occultation has been done on the body as of yet, a summary on the latest information on the body is provided.

Pluto is the largest and most studied TNO, with its latest recorded mean radius of 1188.3±1.6 km by the Long Range Reconnaissance Imager (LORRI) on NASA's *New Horizons* spacecraft during its encounter in 2015 (e.g. Nimmo et al., 2017) or another measurement as made by the same imager of 1187±4 km resulting in a mean density of 1.860±0.013 g/cm^3 (e.g. Stern et al., 2015). Pluto also has a geometric albedo of 0.52[6] with very little oblateness in its shape. Knowledge gained about Pluto from being studied via stellar occultations since 1988 includes the presence of an atmosphere (e.g. Elliot et al., 1989), atmospheric waves in the upper layer (e.g. Person et al., 2008), haze being present in the lower atmosphere (e.g. Gulbis et al., 2015) as well as the atmospheric evolution (e.g. Sicardy et al., 2003, 2016; Pasachoff et al., 2005; Elliot et al., 2007; Young et al., 2008; Lellouch et al., 2009; Bosh et al., 2015). No atmosphere has been discovered around another TNO other than Pluto. The intricate relationship between sublimation and condensation of volatiles such as nitrogen, methane and hydrocarbons at a pressure of ∼10 μbar in Pluto's atmosphere is responsible for global as well as local atmospheric features. Since perihelion in 1989, Pluto's atmosphere has expanded, contradicting theoretical expectations of a condensing atmosphere, hence the reason to continue studying Pluto's atmosphere via stellar occultations is to look for signs of atmospheric collapse. Study of these atmospheric cycles could help correlate surface brightness to condensation of volatiles on a local as well as global scale. Understanding this process will improve general knowledge of planetary atmospheres and place *New Horizon's* data, Pluto's 2015 charged-particle environments as well as its atmosphere and geography, into context. We thus intend to monitor Pluto's atmosphere and look for any signs of atmospheric collapse with the stellar occultations carried out in this thesis.

Haumea is a dwarf planet with satellites, yet at the time of this research it had never been observed with a stellar occultation. Haumea has a recorded diameter of $1239.5^{+68.7}_{-57.8}$ km (e.g. Fornasier et al.,

[6] https://nssdc.gsfc.nasa.gov/planetary/factsheet/plutofact.html - Retrieved 17 November, 2017.

2013) and has a short rotational period just under 4 hours (e.g. Lacerda et al., 2008) that causes large flux fluctuations to be seen in its light curve suggesting a triaxial ellipsoid shape rather than an oblate spheroid shape. This shape has however never been directly imaged, but physical characteristics including a density of 2.6 g/cm^3 (e.g. Lockwood et al., 2014) which makes Haumea more rocky than icy (unusual for TNOs), together with $0.804^{+0.062}_{-0.095}$ (e.g. Fornasier et al., 2013) for its albedo, suggest a former impact encounter is responsible for these unique characteristics. If positively detected, an occultation would improve on any current information we have on Haumea (such as size and orbital position) as well as put some constraints on its physical properties (density and composition). Note that during the production of this thesis, the Haumea event predicted here was successfully observed by Ortiz et al. 2017 and exhibited ring features with a ring radius of 2287^{+75}_{-45} km, ring width of ∼70 km and about a 0.5 line-of-sight opacity. The aim for the future study of this body would thus include searching for the newly discovered ring structures and, even if missed, place constraints.

At the time of this thesis, Orcus had also never been positively detected through a stellar occultation, but had been studied through thermal observing methods (e.g. Brown et al., 2010; Fornasier et al., 2013). The latter has resulted in size constraints of ∼900 km as noted in Brown et al. 2010 and 917±25 km in Fornasier et al. 2013. Together with the size estimates done for Orcus were the size estimates for its only known satellite, Vanth. Physical size estimates for the satellite size are approximately 280 km (Brown et al., 2010) and 276±17 km (Fornasier et al., 2013) with a nearly face-on, circular orbit with a semi-major axis estimated to be either 8983±26 km (Brown et al., 2010) or 9030±89 km (Carry et al., 2011). Density estimates for this system include either being 1.5±0.3 g/cm^3 or $1.53^{+0.15}_{-0.13}$ g/cm^3 (Brown et al., 2010; Fornasier et al., 2013) and an albedo of 0.28±0.04 or $0.27^{+0.07}_{-0.05}$ or even $0.23^{+0.02}_{-0.01}$ (Brown et al., 2010; Lim et al., 2010; Fornasier et al., 2013). If an occultation were positively detected, current information available on Orcus can be improved and could assist in putting some constraints on its physical properties (size, density and composition) as well as search for the presence of any atmospheric and ring features.

Ixion is one of the larger TNOs with a size of 617^{+19}_{-20} km (e.g. Lellouch et al., 2013) and could possibly be a dwarf planet. Ixion has only been detected once before by a single-chord stellar occultation in June 2014 (Barry et al., 2015), but results have not been published. The albedo of Ixion is estimated to be 0.141±0.011 (Lellouch et al., 2013) with no known density measurements currently available. Further attempts are needed to better constrain its physical properties and possibly detect an atmosphere as well as possible ring structures.

2014MU$_{69}$, named Ultima Thule after the submission of this thesis, has been chosen as the approved, extended-mission flyby target of *New Horizons* on 01 January 2019. Information on 2014MU$_{69}$ is limited to the *Hubble Space Telescope* due to its 26.8[7] apparent magnitude. Assuming this body is a classical TNO with standard albedo between 0.04-0.15[8], its size is likely between 25-45[10] kilometers in diameter. Its spectrum is reddish in nature (Porter et al. 2016), which is common for aged surfaces in the outer Solar System. There were only three 2017-scheduled stellar occultations predicted for this object before the arrival of the *New Horizons* spacecraft. A positive detection on any of these events would improve on size estimates (and thus albedos, composition and density) and position, and could reveal some information on its immediate surroundings. Be-

[7] http://www.planetary.org/blogs/emily-lakdawalla/2015/09011608-new-horizons-extended-mission-pt1.html - Retrieved 21 November, 2017.

[8] http://www.stsci.edu/institute/stuc/oct-2014/New-Horizons.pdf - Retrieved 21 November, 2017.

cause so little is known, and the information is vital to the *New Horizons* mission, gathering or improving on any current information we have on $2014MU_{69}$ is important to ensure a successful flyby of this object by the *New Horizons* spacecraft in 2019.

Chariklo is the first non-giant planet in our Solar System known to possess a ring system. Chariklo is a Centaur and the system consists of two rings that orbit at radial distances of 391- and 405 km from a 250-km diameter nucleus, with 7- and 3 km widths, and optical depths of 0.4 and 0.06, respectively (e.g. Braga-Ribas et al., 2014). No formal density value has been determined, however Chariklo does have an estimated albedo of 0.040 ± 0.009 (e.g. Leiva et al., 2017). Further investigation revealed some finer details of the structure of Chariklo's rings where the two rings, C1R and C2R are flat, C1R exhibits a W-shaped structure and has $\sim$2.5 km width variations along the ring longitude between 5- and 7.5 km together with sharp edges and contains about 10 times more material than C2R (Bérard et al., 2017). The formation mechanism for rings around small bodies is still under debate, although Chariklo's rings show strong similarities to that of Chiron's proposed rings (e.g. Ortiz et al., 2015) and suggest a common mechanism around Centaurs. Rings could even perhaps be due to cometary activity resulting in a debris disk, collisional remnants of previous satellites or from an impact. Further studies of ring systems, such as dynamical timescales, formation constraints, and evolving substructures residing within the rings need to be done. The aim for this body is therefore to study its ring system through the stellar occultations in this thesis.

$2003MW_{12}$, or Varda (proposed name), has the possibility of being a dwarf planet as it is one of the larger known TNOs. There have been no positive stellar occultations for Varda to date. Data from the *Hubble Space Telescope* suggests a size of 722^{+81}_{-76} km from spatially resolved images (Grundy et al., 2015) and another size measurement from thermal observations estimates its size to be around 705^{+81}_{-75} km (Vilenius et al., 2014). These values place the approximate density for this system to be at $1.24^{+0.5}_{-0.4}$ g/cm^3 (Grundy et al., 2015). The only known satellite of Varda has an estimated size of half of the main body in a face-on, near-circular orbit (Grundy et al., 2015). The geometric albedo measurements for Varda are $0.102^{+0.024}_{-0.024}$ (Vilenius et al., 2014) and $0.166^{+0.043}_{-0.033}$ (Grundy et al., 2015). Successful detection could help constrain the sizes of the Varda bodies separately, as well as resolve the existence of a possible atmosphere or rings around the primary.

The remainder of this chapter covers the observational section of stellar occultations by outer Solar System bodies including predictions, brief descriptions of the various instruments that were used to observe these events, and how data were taken for each event.

1.3 Observations

1.3.1 Predictions

The success rate for stellar occultations is directly tied to the prediction accuracy for a given event. A more accurate prediction improves the chances of a successful detection which in turn enhances any future predictions made for the given body. But there are a number of criteria that need to be met before something is labeled to be a predicted stellar occultation event.

The criteria include the reliability of the occulting star's orbital position, brightness, proper motion, the certainty in the ephemeris of the occulting body, the time of day that the event is predicted to happen, the size and location of the shadow path on Earth, shadow velocity and the availability of

suitable telescopes that are equipped with the correct instruments close to or within the shadow path.

However, these predictions are always associated with some margin of error (both along and cross track) in the shadow path. Errors in the shadow path along the track lead to errors in timing, while cross track errors move the physical location of the shadow path. This is due to positional uncertainties in the occulting star as well as the occulting body.

Historically speaking, stellar catalogs contain some errors (systematic and random) when reporting coordinates and proper motions. Older catalogs had bigger errors or would lack important information such as the proper motion for a given star. The latter is quite common for fainter stars which could result in ground track errors on the order of the Earth's radius. More modern surveys certainly improved on their predecessors's shortcomings. Brighter stars naturally have lower errors whilst gathering information on fainter stars would result in poorer precision.

Whilst a target star with a well-known position is preferable, another requirement, is having an accurate ephemeris for the occulting body. This, however, varies from body to body, as most TNOs have only been discovered relatively recently. Therefore, the larger bodies are more likely to have well-defined ephemerides because of easier detection and earlier discovery, which would in turn suggest a high number of observations were done on a frequent basis. If an occulting body is not observed sufficiently the errors in its ephemeris are large, and hence, the errors in the predicted midtime for a stellar occultation tend to increase and there is more uncertainty in the location.

Apart from the above criteria, predictions made for the events mentioned in this thesis were done by members from the MIT Planetary Astronomy Laboratory (MIT-PAL). Reference information about the target star would be gathered from the Second U.S. Naval Observatory CCD Astrograph Catalog (UCAC2) while positions for the occulting body would include calculating the ephemeris residuals using observational data[9] from the reference ephemeris as stated by JPL Horizon's ephemeris. This process of calculating the positional residuals between the reference catalogs and the direct observational measurements, ensure that the positions for both the object as well as the occulting body are as current as possible. The sites that were used during these observations are the South African Astronomical Observatory (SAAO); three sites of the Las Cumbres Observatory at Sutherland (CPT), South Africa; Fort Davis (ELP), Texas and Cerra Tololo (LSC), Chile; and the NASA InfraRed Telescope Facility (IRTF) in Mauna Kea, Hawaii. The specifics about these sites are provided in the next section. The predictions are given in Table 1, and their corresponding globes that display the predicted shadow paths on Earth are shown in Fig. 1.

[9]Data from three telescopes spanning over a couple of years were reduced with respect to stars in the UCAC2 catalog. The three telescopes are: U.S. Naval Observatory (USNO) 61-in telescope; Small and Moderate Aperture Research Telescope System (SMARTS) 0.9-m telescope, as well as the Lowell 42-in telescope.

Table 1: Stellar occultation predictions.

Event	Mag	Reference star position		Site specifics Predicted midtimes (UT) and velocity (km/s)					
		RA (h:m:s: J2000)	Dec (d:m:s: J2000)	SAAO	LCO			IRTF	Geocenter
					CPT	ELP	LSC		
Pluto.20160719	13.96[a]	19:07:22.1198±0.0131	-21:10:28.474±0.010	-	-	-	-	-	20:52:03±00:00:37 23.51
Haumea.20170121	18.0[a]	14:12:03.1960±0.0122	+16:33:58.645±0.013	02:52:51±00:02:28 14.28	-	-	-	-	02:58:48±00:02:28 14.36
Orcus.20170307	14.3[b]	10:08:18.5407±0.0097	-09:40:14.111±0.010	-	-	26.316[e]	-	06:59:45±00:05:58 26.271	06:56:48±00:05:58 25.96
Ixion.20170505	12.62[a]	17:39:52.91±0.0193	-28:14:24.04±0.086	-	-	-	05:49:36±00:01:32[f]	-	05:47:22±00:01:32 17.99
$2014MU_{69}$.20170603	15.330[b]	19:03:34.5[c]	-20:34:39.3[c]	03:09:38 20.3	03:09:38 20.3	-	-	-	-
Chariklo.20170622	13.99[a]	18:55:15.6525±0.0068	-31:31:21.695±0.011	21:19:58±00:04:28 22.33	21:19:58±00:04:28 22.33	-	-	-	21:17:48±00:04:28 22.00
Varda.20170629	16.09[a]	17:16:29.9121±0.0182	-01:45:50.515±0.005	23:44:58±00:03:04 23.76	23:44:58±00:03:04 23.76	-	23:50:22±00:03:04 23.86	-	23:47:06±00:03:04 23.54
$2014MU_{69}$.20170717	12.602[b]	19:00:08.3[c]	-20:39:38.0[c]	-	-	-	03:50:13 24.2	-	-
Chariklo.20170723	13.89[a]	18:48:09.2203[d]	-31:26:32.448[d]	-	-	-	05:58:52±00:04:37 21.02	-	05:57:27±00:04:37 21.02

[a] UCAC2 magnitude where the bandpass is between V and R (579-642nm).

[b] GAIA g band spanning from 400-1000nm and peaks in R(∼700nm).

[c] The RA and Dec values for all of the $2014MU_{69}$ events are from http://www.boulder.swri.edu/MU69_occ/index.html and no errors are provided with the star positions. The $2014MU_{69}$ stellar occultations were not made available in the standard way (via MIT-PAL). Hence only the values are provided with no errors.

[d] The Chariklo.20170723 event was the first and only event that used GAIA stellar positions and no errors were provided for the prediction made by MIT-PAL.

[e] A stellar occultation was detected at this site but not of the expected target body. Hence why only velocity information is given.

[f] With no occultation detected, velocity for this particular event was omitted in the LCO proposal but predicted midtime was still needed.

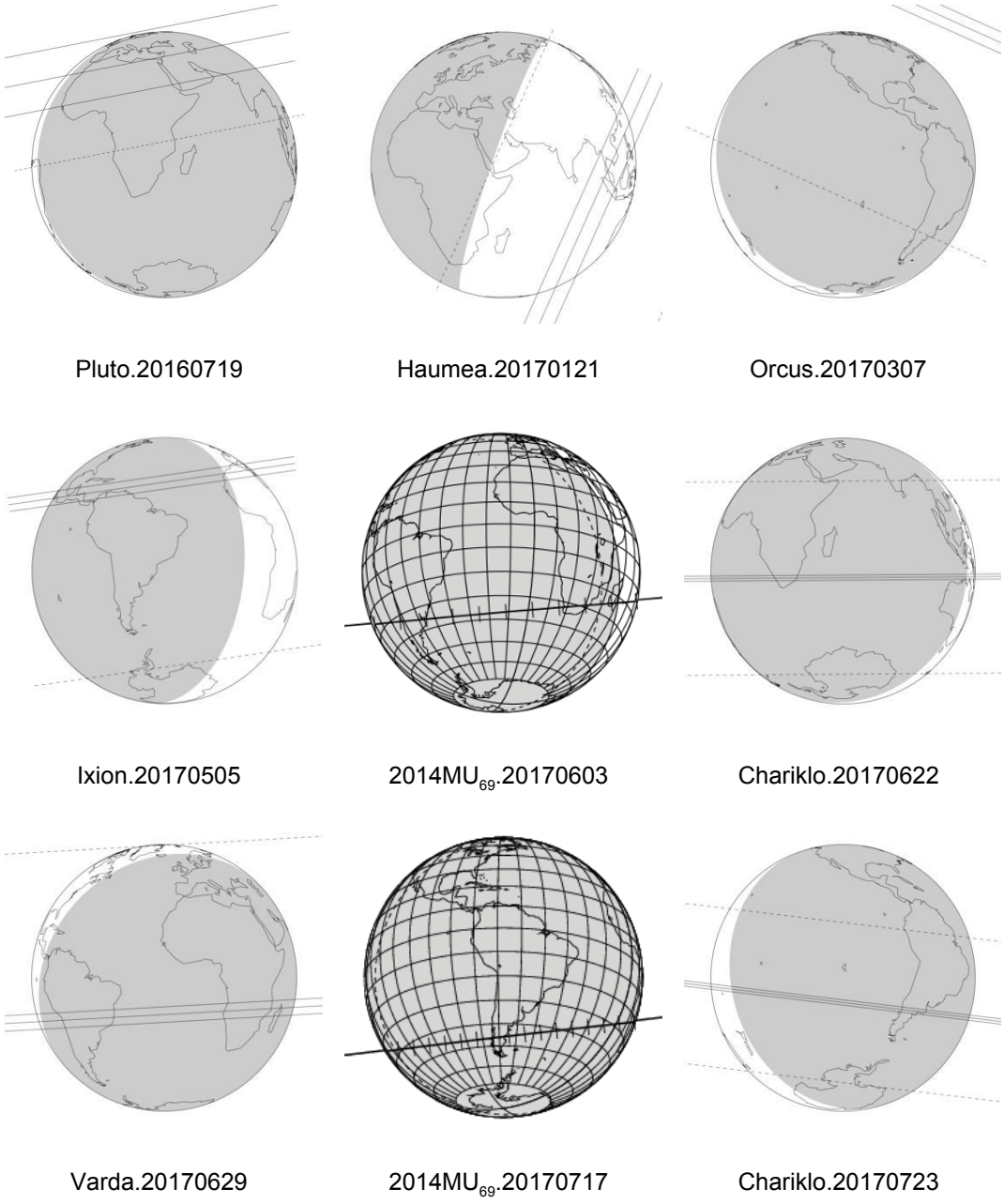

Figure 1: Globes of the Earth showing the shadow paths for the occultation events covered during this thesis. The names below the globes represent the events as listed in Table 1. The shaded regions on these globes illustrate the regions on Earth where the Sun is more than 0° below the horizon. The three solid lines represent the top to bottom regions of the object: top represents the northern limb, the center and then the bottom represents the southern limb respectively. The dashed lines correspond to one-sigma errors on the predicted shadow path location.

1.3.2 Instrumentation and sites

Stellar occultations are generally difficult to observe because of the faint target stars as well as the short timescales involved. Specialized equipment like fast-imaging instruments with accurate timing devices are needed for stellar occultations. Imagers are attached to large telescopes and are either portable or they are confined by design to only be compatible with a certain telescope. The telescope and imager combination, along with some other components that are mentioned in this section, enable the capture of these short-lived events. This section therefore focuses on discussing the instrumentation that was used during the attempted stellar occultation observations.

The SAAO stellar occultation program encompasses various telescopes across the world in order to provide many opportunities to observe the predicted events. The widespread geographical locations include various sites from the LCO telescope network, Mauna Kea, Hawaii and Sutherland in South Africa. Details about the various sites of the telescopes are listed in Table 2 at the end of this section.

1.3.2.1 Massachusetts Institute of Technology Optical Rapid Imaging System (MORIS)

The MORIS (Gulbis et al., 2011) instrument was based on a similar system designed specifically for observing stellar occultations called the Portable Occultation, Eclipse, and Transit Systems (POETS) (Souza et al., 2006) which was a joint project between MIT-PAL and collaborators from Williams College. MORIS is a high-speed, optical camera that is optimally interfaced with a medium-resolution near-infrared spectrograph and imager called SpeX (Rayner et al., 2003), which is used with NASA's 3-m InfrarRed Telescope Facility (IRTF) on Mauna Kea, Hawaii. POETS, however, was designed to be a mobile system that is compatible with various telescopes, whilst MORIS was specifically designed to integrate with SpeX which is permanently attached to the IRTF. The SpeX spectrograph has a Teledyne 2048x2048 Hawaii-2RG array and the IR slit viewer has a Raytheon Aladdin 3 1024x1024 InSb array but only a 512x512 quadrant is used. With some residual flux from the object being used by the Aladin 3 InSb array for guiding purposes. This array known as Guidedog is primarily used for acquisition as well as guiding in the infrared, however, it can also be used for J, H or K band images taken simultaneously with MORIS. MORIS even serves as a very efficient visible guide camera for SpeX but is used as an optical imager for the science done in this thesis. The spectrograph of SpeX is known as Bigdog and is used for low-resolution spectra (rather than Guidedog) if the target star is bright enough. This setup allows for simultaneous observations done in the near-infrared as well as at optical wavelengths. Observations done in this manner provide valuable structural details about bodies with atmospheres, details that would otherwise be lost in the optical (Gulbis et al., 2015).

The prime component of MORIS is an Andor iXon^{EM+} DU-897 camera with a thermoelectrically cooled (-70°C), black-illuminated, 512x512 pixel charge-coupled device (CCD) that returns a 58.3" square field of view that has a high quantum efficiency with low read noise, dark current and dead-time for the high-quality images it produces. A unique feature of this camera is the two different modes that it offers its users: conventional (CON) mode or electron-multiplying (EM) mode. The latter mode results in subelectron read noise levels and is primarily used for unusually faint sources. However it does come at the expense of the dynamic range compared to that of the conventional mode whilst also adding an additional noise factor. Both these modes have a preamplifier with a 1x, 2.4x or 5x gain setting. The resultant analog signal is then converted to a digital signal using

either a 14-bit or 16-bit analog-to-digital converter (ADC) with readout rates of 3, 5, or 10 MHz for the first and 1 MHz for the latter ADC. EM mode is therefore ideal for shorter exposures of faint objects and hence has all of the above mentioned readout rates available, however, only the 1 and 3 MHz readout rates are available for CON mode. For even faster readout rates the user could resort to binning and subframing the images accordingly to achieve the required cadence. Performance also depends on the selected preamplifier setting, mode and readout rate.

A 10-slot filter wheel supports four Sloan Digital Sky Survey filters (SDSS; Fukugita et al., 1996): *g'*, *r'*, *i'* and *z'* produced by Asahi Spectra; two Johnson filters: *V* and *VR* (Jewitt et al., 1996); and a broad OG590 red filter consisting of a 3mm Schott OG590 and a 2mm BK7. An open or empty filter wheel slot is the standard for observing stellar occultations.

A Global Positioning System (GPS) is situated in a cooling container connected to a small antenna situated at the top of the telescope by a RG-58 coaxial cable. The Spectrum Instruments, Inc. Intelligent Reference/TM-4 GPS needs connections to a minimum of four satellites to require accurate geographic information (longitude, latitude and altitude) as well as time. After the completion of this prerequisite, times, as specified by the manufacturer, have an accuracy of ±25 nanoseconds from UTC, given that only one satellite is connected to the GPS. A handy camera-triggering feature is provided by the GPS where a single width-specific pulse will start a series of exposures done by the camera or each exposure could be triggered to readout with repeating width-specific pulses over some specified interval which is the standard mode used for stellar occultations. Furthermore the GPS has the added functionality of a programmable output pulse in addition to the general one-pulse-per-second output. The images have a datacube-format, a 3-dimensional array containing n-amount of successive Flexible Image Transport System (FITS) images. The number of images is also known as the kinetic series length of the datacube.

Observations that are scheduled to be done at the IRTF are done remotely from Cape Town where a connection to the instruments allows data to be acquired while a Telescope Operator (TO) located on site is in charge of the telescope.

1.3.2.2 Sutherland High-speed Optical Cameras (SHOC)

Whilst both SHOC (Coppejans, 2013) instruments (Shocnawe[10] and Shocndisbelief[11]) were based on the same design as MORIS, and therefore on POETS as well, they do differ from their predecessors in terms of the mounting mechanism, the more modern hardware such as the larger 1024x1024 pixel CCD, as well as being custom interfaced with the SAAO telescopes.

The major component is an Andor iXon X3 888 UVB camera with a thermoelectrically cooled (-50°C and lower), back-illuminated, 1024x1024 pixel CCD that returns a 1.29' and 2.85' square field of view on the 74- and 40-in SAAO telescopes respectively, that has high quantum efficiency with low dark current, deadtime and read noise to ensure the optimal quality of its images. Both CON- and EM-mode with the same readout rates and ADC as that of MORIS is available on SHOC, with preamplifier gain settings of 1.0x, 2.4x or 4.9x for Shocnawe and 1.0x, 2.5x or 5.2x for Shocndisbelief. Subframing and binning are also available features to SHOC-users to acquire the desired cadence. Performance rates for both systems depend on the preamplifier setting, mode and rate chosen by the user.

[10]Serial number: 5982
[11]Serial number: 6448

There are no filter wheels present within SHOC itself, but whilst working in unison with the various SAAO telescopes means that the same filter wheel(s) as employed by the respective SAAO CCDs (either one or two can be mounted), containing the Bessell U, B, V, R and I filters as well as an open slot, are used. The second filter wheel contains the SDSS filters: u', g', r', i' and z' as well as an open slot.

As with MORIS, a Spectrum Instruments Inc. Intelligent Reference/TM-4 GPS instrument ensures timing accuracy and provides the same camera-triggering options as mentioned previously thanks to the programmable output functionality provided by this GPS. Both of these components are inter-connected to various peripherals as well as a computer from which control commands are run and provide the images in the same datacube format as mentioned above.

1.3.2.3 Las Cumbres Observatory (LCO) 1-m telescope guide cameras

The Finger Lakes Instrumentation MicroLine 4720 frame-transfer cameras are the designated autoguider cameras mounted on one of the four off-axis ports on the 1-m LCO telescopes (Brown et al., 2013).

The FLI guide cameras are independently focusable with a back-illuminated, 1024x1024 pixel CCD (e2V 4720) which returns a 5.72' square field of view with a readout speed of 500 kpixels/s, ∼2-second deadtime and average read noise of 16.95 electrons for all the cameras. The observations requested with these guide cameras were all done with 2x2 binning (0.674 arcsec/pixel) and 2 MHz amplifiers with fixed internal gain settings ranging from 2.725 to 2.85[12]. The use of multiple telescopes at each site with staggered start times is an allowable, but uncommissioned mode. This mode allows for higher spatial resolution between the collective observations compared to the spatial resolutions achieved by the observations as done per individual telescope.

Available filters are SDSS/PanSTARRS filters: u', g', r', i', z_s, Y, w, Johnson-Cousins/Bessell filters: U, B, V, R, I and an open slot.

An on-site GPS receiver/NTP sever (a Symmetricomm/MicroSemi S250) is used to distribute time via NTP over Ethernet to the instrument computers with an estimated time accuracy of 1-5 milliseconds depending on network load as recorded within the FITS-headers.

1.3.2.4 Site information

Various sites were used to increase the probability of a positive detection for the predicted stellar occultations, as a single chord detection has large errors associated with size measurements due to the unknown geometry of the body or, even with good astrometry, errors are also associated with the positional measurements. Table 2 provides the geographic information of the sites that were used for observing the predicted stellar occultations.

[12]Personal communication with Dr. Tim Lister, Staff Astronomer at the LCO.

Table 2: Observatory Sites.

Site	Telescope Diameter (m)	Latitude	Longitude	Altitude (m)
Cerro Tololo Interamerican Observatory Cerra Tololo, Chile (LSC)	LCO: 3x 1.0	30°10'2.64" S	70°48'17.28" W	2198
McDonald Observatory Fort Davis, Texas (ELP)	LCO: 1x 1.0	30°40'12" N	104°1'12" W	2070
NASA InfraRed Telescope Facility Mauna Kea, Hawaii	IRTF: 3.0	19°49'34" N	155°28'19" W	4168
South African Astronomical Observatory Sutherland, South Africa (CPT)	SAAO: 1.9 and 2x 1.0 LCO: 3x 1.0	32°22'48" S	20°48'36" E	1800

1.3.3 Instrument settings for data acquisition

Depending on the body size and the geometry of the event, stellar occultations could last up to anything from a few seconds to a few minutes. A 4-hour observation window centered on the predicted midtime of the event is enough time for calibrations and to probe the environment surrounding the main body out far enough to search for the presence of an atmosphere, rings, jets, comas, satellites, or debris. The high-speed data are typically a 40-45 minute block, centered on the predicted midtime. The data taken well before and/or after the occultations have long exposure times for astrometric and calibration calculations and to resolve both the star and the occulting body. The high cadence observing block does take into account the timing uncertainties as well as the need for a baseline from which to derive the signal-to-noise ratio (SNR). SNRs of a few tens per data point were needed to achieve our scientific goal to have a solid-body detection: higher SNRs allow derivation of atmospheric profiles and the detection of fainter features. This observing method was used for the MORIS and SHOC observations.

For the LCO autoguider cameras, 1.25 hours were used for each telescope at the specific site. A 40-min window was centered on the predicted midtime, ∼5 minutes for slewing and setup for each of the requested pointings, as well as ∼15 min approximately 2 hours before and after. As mentioned previously, the start times of the multiple telescopes at each site are staggered to increase the spatial resolution of the occultations and is an allowable, but uncommissioned, mode.

Table 3 contains the particulars on the instrumental settings for each dataset that was acquired for each event.

Table 3: Instrument settings.

Event	Instrument	Number of frames in datacube	Cadence* (Hz)	Filter	Binning	Readout Rate (MHz)	Mode	Sensitivity (e/ADU)	Timing	Seeing** (arcsec)
Pluto.20160719	SHOCA	8000	$3.\dot{3}$	Open	8x8	3	CON	1.82	GPS	1.94
Haumea.20170121	SHOCD	520	$0.\dot{3}$	Open	4x4	1	CON	1.53	GPS	-
	SHOCA	295	0.5	Open	10x10	1	CON	1.69	GPS	1.73
Orcus.20170307	LCO-ELP GC	366	0.17	Open	2x2	2	-		Internal	1.33
	MORIS	11000	5.0	Open	4x4	1	CON	1.47	GPS	1.56
Ixion.20170505	LCO-LSC GC	1499	(0.31, 0.31, 0.24) 0.85	Open	2x2	2	-		Internal	1.13
$2014MU_{69}$.20170603	LCO-CPT GC	882	(0.24, 0.24) 0.47	Open	2x2	2	-		Internal	1.14
	SHOCD	27000	10.0	Open	8x8	3	CON	1.77	GPS	1.26
Chariklo.20170622	SHOCD	7560	5.0	Open	6x6	3	CON	1.77	Internal	1.00
Varda.20170629	LCO-CPT GC	603	(0.12, 0.16, 0.12) 0.4	Open	2x2	2	-		Internal	1.35
	SHOCD	6000	2.5	Open	8x8	3	CON	1.77	GPS	1.00
$2014MU_{69}$.20170717	LCO-LSC GC	1056	(0.31, 0.31) 0.62	Open	2x2	2	-		Internal	1.02
Chariklo.20170723	LCO-CPT GC	219	(0.31, 0.31) 0.62	Open	2x2	2	-		Internal	1.10

SHOCA - Shocnawe
SHOCD - Shocndisbelief
GC - Guide Camera(s)
CON - Conventional Mode

* Cadence calculations for the LCO events included staggered start times with a cycle time of the exposure time plus an assumed median deadtime as noted in 7 for 45 minutes. The total number of frames are then divided by the total observation time. The individual cadences for the respective guide cameras are in parentheses followed by the combined cadence value. Due to the SHOC and MORIS events being GPS triggered, the cadence calculations were done by dividing 1 with the exposure time.

** Seeing as recorded in the FITS headers at the start of the observation and is not considered to be an instrument setting but rather an environmental condition.

2 Data Analysis

2.1 Data pipelines

Observational datacubes need to be processed for scientific analysis. The main goal of the following data pipelines are to go from FITS images to stellar differential light curves. Three types of instruments were used during observations, thus the three corresponding pipelines are discussed.

2.1.1 SHOC

During the commissioning of SHOC, users had no pipeline that would provide them with analysis-ready reduced data. Based on her own observations, pipeline software was developed and shared by Dr. Marissa Kotze with a short manual available at http://shoc.saao.ac.za/Pipeline/SHOCpipeline.pdf. The SHOC pipeline does have added functionality to support the different requirements from its various users and is employed here. This section expands on the information contained in this manual as changes have been made to produce outputs that are more suitable for analysis done on stellar occultation data.

The SHOC pipeline has two different versions that are available for users: an informal, preliminary version that produces raw, unreduced light curves to serve as a quick-look of the data taken when at the telescope, and a full version which is more extensive than its compact counterpart, which produces more suitable light-curve results. The latter version was used more extensively throughout this thesis and is the main focus when referring to the SHOC pipeline. Some observations were exceptions as they would, initially, not produce any results from the full SHOC pipeline. Results were yielded by firstly, running these events through the quick-look version as to produce average optimal apertures, that secondly, served as guidelines for fixed-aperture photometry in the full SHOC pipeline version.

Both of these versions are provided in the SHOCpipeline.tar[13] folder together with a README file to help the user setup the correct environment to run the various scripts. These scripts were run on the SAAO ASTRO server as it has the correct dependencies needed by the Python-based scripts which call on various packages like PyFITS[14] and PyRAF[15] during execution.

2.1.2 SHOCpipeline.py

With the SHOC instruments allocating a single FITS header to each of the constituents of the datacube, the approach of the SHOCpipeline.py script is simple:

- To determine what reduction tasks are going to be executed, i.e. flat fielding, bias-correction or none.
- If needed, to split the calibration datacubes into their multiple primary FITS image components.
- To update each of the FITS headers of the flat-, bias- and raw datacubes with the correct information. Corrections include inputs supplied by the user as well as specific information

[13] http://shoc.saao.ac.za/Pipeline/
[14] http://stsdas.stsci.edu/download/wikidocs/The_PyFITS_Handbook.pdf
[15] http://stsdas.stsci.edu/stsci_python_sphinxdocs_2.13/docs/pyraf_guide.pdf

about the SHOC instrument[16] that was pre-supplied within a text file. The latter documentation is only used to extract the needed information for when the RON (readout noise) and SENSITIVITY headers are absent.

- To prepare the raw datacube for any pre-reductions if the corresponding calibration frames are provided or to simply continue on with the process similar to that of the quick-look version.

The outputs of the SHOCpipeline.py script are called SHOCscript, PHOTscript and PLOTscript. These three scripts call upon multiple other scripts to execute various actions on the datacube and are discussed here in order of appearance in the respective script. A flow chart of the SHOCpipeline.py script with section numbers in italics for reference is provided in Fig. 2.

[16] http://shoc.saao.ac.za/Documentation.html

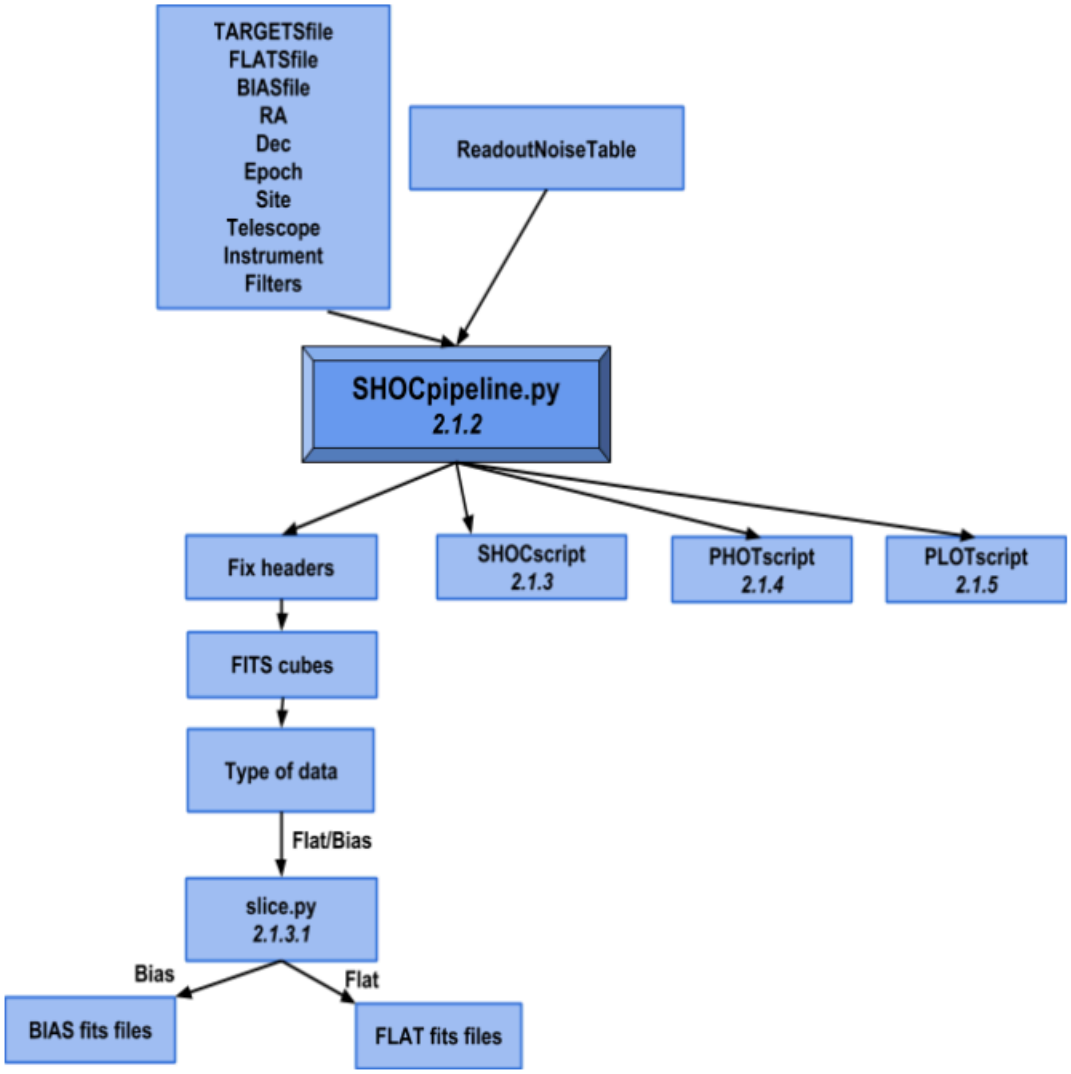

Figure 2: Flow chart of SHOCpipeline.py with section numbers (in italics) provided for reference to the corresponding script descriptions in this thesis.

2.1.3 SHOCscript

The main objective of this compiled script is to produce master calibration frames with which to reduce the individual FITS images of the datacube, as well as deriving the various timing information that is needed to occupy the timing headers of each individual image respectively. A flow chart of the SHOCscript with section numbers in italics for reference is provided in Fig. 3.

2.1.3.1 slice.py

This script integrates Python with IRAF to deconstruct the datacube into separate images using the imutil task imslice[17] from the images package. Imslice returns a lower-dimension output as the input file which in this case is a 3D-datacube which results in multiple individual FITS images with identical headers to that of the original 3D-datacube header.

2.1.3.2 frametime.py

Since the SHOC instruments provide their users with three time-triggering options, the time derivations for individual images can be done in three ways. As mentioned above frames could either be triggered via GPS (accurate to the order of a few microseconds), via the local computer clock (absolute timing accuracy of ± 0.5 seconds) or via both. The pipeline needs to accommodate all timing options in order to ensure the correct timing derivations occupy the headers of the individual frames.

For starters, PyFITS (Greenfield et al., 2002) is used to correct the start time of the exposure initially supplied in the "FRAME" header of the FITS files. When the internal triggering (using local computer time) option is used to take data frames, the actual time recorded in the "FRAME" header entry is firstly, rounded to the nearest second and secondly, represents the time at the end of the first exposure of the datacube. Another timing header called "DATE-OBS" also provides a timing value, but this value represents the time the user physically pushed start on the SHOC-interface and is therefore inaccurate. This script corrects for this inaccuracy in the "FRAME" header as follows:

$$t_{internal} = t_0 + t_{exp} \times (x - 1), \tag{1}$$

where $t_{internal}$ is the start time of the exposure, t_0 is the time recorded at the end of the first exposure as stated in the "FRAME" header, t_{exp} is the exposure time of the observation and $x = 0$ for the first frame, $x = 1$ for the second frame etc. For the first image in the datacube $x = 0$, $t_0 =$ FRAME and t_{exp} would be the exposure time. Hereafter, each consecutive frame would follow at δt-increments equivalent to "ACT" or "KCT" which is a combination of the readout and the exposure time known as the integration cycle time. All times are recorded as UT and yield the hours-from-midnight format in the new "UTC-OBS" FITS header.

In the case of externally triggered or rather, GPS-triggered frames, the first two FITS images of a datacube gets disposed. The first FITS image is ignored due to the CCD continuously exposing while waiting for the GPS-trigger and is therefore not a "normal" exposure, the second is removed due to consecutive "keep-clean" cycles being run prior to the first GPS-pulse being received. Essentially this causes the start of the first exposure to be late on the order of five microseconds and consequently, this delay would carry over into the exposure time of the second frame which, in turn, causes a slightly shorter exposure time than intended (Coppejans, 2013).

[17] http://iraf.noao.edu/iraf/ftp/pub/beguide.pdf

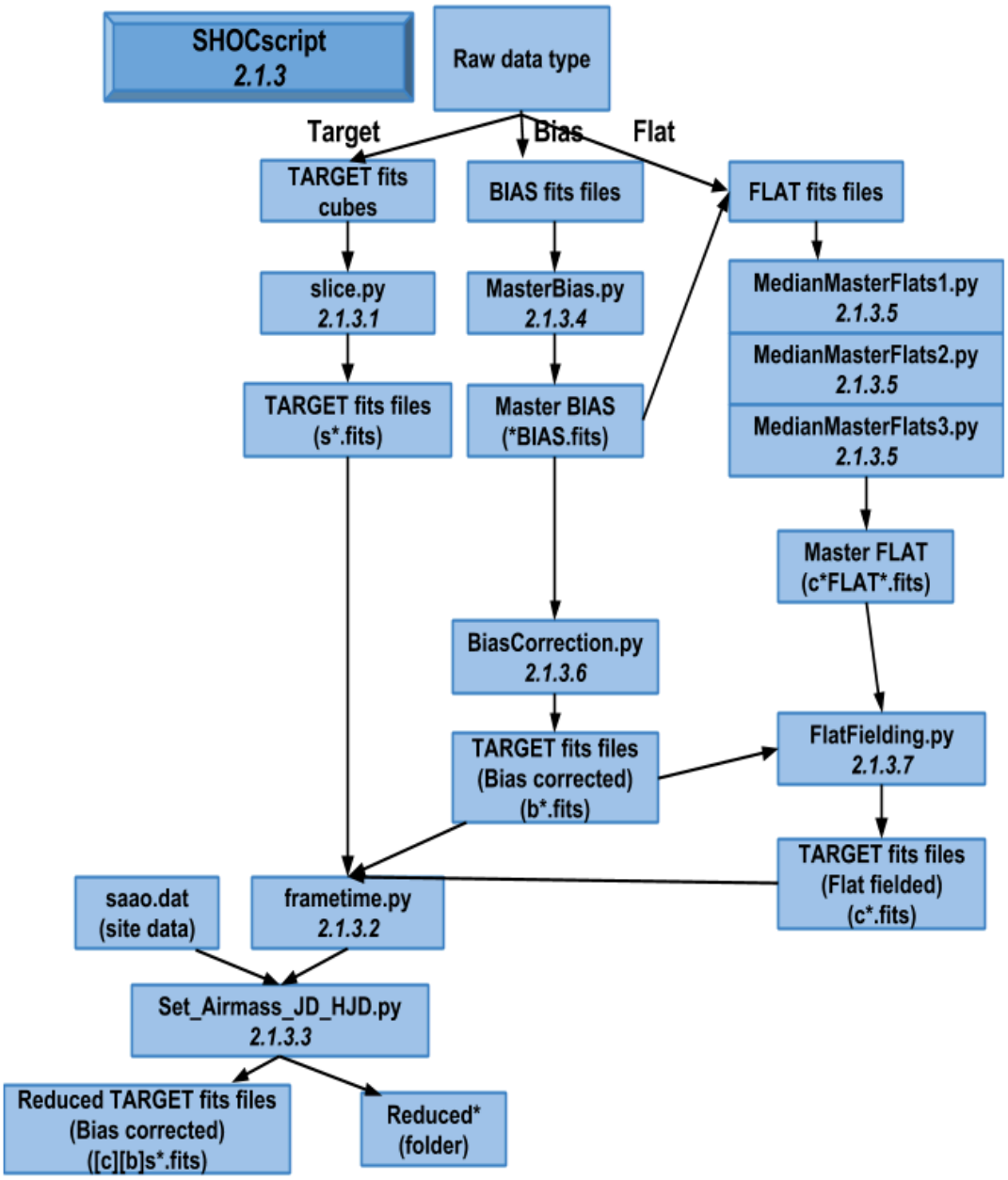

Figure 3: Flow chart of SHOCscript with section numbers (in italics) provided for reference to the corresponding script descriptions in this thesis.

The user is prompted to supply the SHOC pipeline with the start of the datacube (t_0) and the GPS integration time (t_{exp}), which corrects the "FRAME" and "EXPOSURE" headers during the SHOCpipeline.py script. The frametime.py script, together with the correct GPS information supplied by the user present in the "FRAME" and "EXPOSURE" headers enables the timing derivation of the consecutive FITS images by:

$$t_{external} = t_0 + t_{exp} \times (x + 1), \tag{2}$$

where the variables have the same meaning as before.

An observation could also be triggered to start through GPS, this is noted in the FITS headers as an "External Start". This triggering method serves as a combination between internal and external triggering modes. In this case the first trigger received from the GPS would cause the "keep-clean" cycle to finish after completion and rather start the exposure of the first frame following internal triggering methods than cause the camera to readout. This script therefore approaches this triggering version as follows:

$$t_{externalS} = t_0 + t_{exp} \times (x), \tag{3}$$

where the variables are represented in the same manner as for the internal triggering mode. For light curves, however, the midpoint of the exposure is a better representation of where in time the data were taken, this pipeline does not include this timing derivation and all times provided ($t_{internal}$, $t_{external}$ and $t_{externalS}$) represent the start time of the frame's exposure.

2.1.3.3 Set_Airmass_JD_HJD.py

When provided with the necessary header information, such as the information provided by some of the new as well as the corrected headers that resulted from the scripts mentioned above, the "AIRMASS", "JD" and "HJD" headers can be populated by making use of the IRAF package astutil, asthedit and setjd tasks (Davis et al., 1994). The site information for the SAAO is covered in the saao.dat file which is already included in the IRAF observatory database. These values have up to 8 decimals for accuracy if the user intends to do a separate airmass correction on the data outside of this pipeline.

2.1.3.4 MasterBias.py

This PYTHON script uses PyRAF to import the IRAF packages images[18], immatch (Phillips & Davis, 1995) and imutil[19] task imcombine[20] to median all of the raw bias frames into one master bias frame. If no raw bias frames are available then this script is omitted.

2.1.3.5 MedianMasterFlats(1,2,3).py

The three scripts' combined outputs are equivalent to the previous MasterFlats.py script as mentioned in http://shoc.saao.ac.za/Pipeline/SHOCpipeline.pdf, but with slight modifications (as done by myself to be incorporated into this pipeline) such as master bias subtracting the raw flat frames and median-combining instead of mean-combining the flat frames to produce a master flat frame. The PYTHON script calls on the IRAF packages images, immatch and imutil

[18] http://iraf.noao.edu/iraf/ftp/pub/beguide.pdf
[19] https://media.readthedocs.org/pdf/stak/dev/stak.pdf
[20] http://iraf.noao.edu/iraf/ftp/pub/beguide.pdf

tasks imarith[21] to bias subtract the raw flat frames, imstatistics[22] to normalize the calibrated flat frames respectively and the imcombine task to median-combine all of the normalized flat frames for a master flat frame.

2.1.3.6 BiasCorrection.py

This script subtracts the master bias frame from all of the respective data frames by way of the imarith task from the IRAF images and immatch and imutil packages that are prompted through PyRAF.

2.1.3.7 FlatFielding.py

This script is similar to the script in section 2.1.3.6 above, except it divides the individual bias-subtracted data frames with the master flat frame.

2.1.4 PHOTscript

This script is LINUX based and runs all of the photometry tasks that are contained within the Photometry.py script through PYTHON. A flow chart of the PHOTscript with section numbers in italics for reference is provided in Fig. 4.

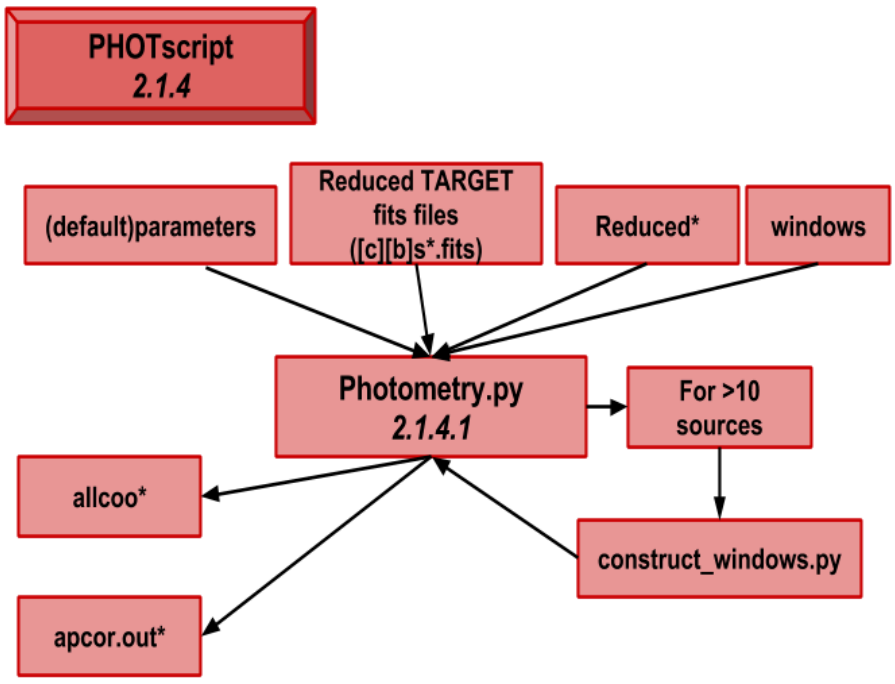

Figure 4: Flow chart of PHOTscript with section numbers (in italics) provided for reference to the corresponding script descriptions in this thesis.

[21] http://stsdas.stsci.edu/cgi-bin/gethelp.cgi?imarith
[22] http://iraf.net/irafhelp.php?val=imstatistics&help=Help+Page

2.1.4.1 Photometry.py

The photometry on the data frames can be done either by aperture-corrected photometry or by fixed-aperture photometry. But in order for any of the two photometry methods to be executable, the user must first define the position of the target source(s). This selection determines how the pipeline should "find" the sources or where the sources are allocated on the images. If the coordinates of the target sources are known, a "windows" text file is constructed. The "windows" file contains the X and Y coordinates of the source(s) of interest, in which each line contains one set of coordinates. In both cases where a "windows" file is either provided or not provided and one needs to be produced, the script prompts the user to define a star-free region on the first image of the cube as shown in Fig. 5.

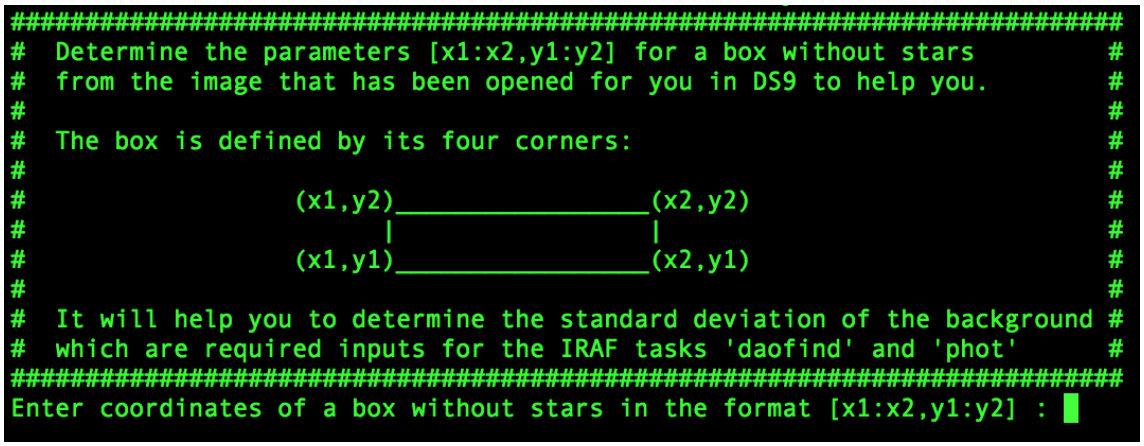

Figure 5: Defining the background threshold prior to photometry with PHOTscript.

From this defined background region the standard deviation of the background is determined using the imstat task from the imutil IRAF package. The user then defines the required significance level (n) needed for a valid detection. Any pixel value above this threshold $n\sigma$ value is then considered as a source by the pipeline. These two values, the standard deviation of the background and the required significance level, help setup the parameter files, datapars and findpars for the daofind task of the daophot, digiphot, noao package (Davis et al., 1994). The latter task determines the positions of all the sources that breach the threshold value (in the case where no "windows" file was provided). This step can either be done once or multiple times (for each frame) depending on whether the observations were guided or not. If the observations were guided, with no drifting of the sources throughout the frames, then it is only necessary to determine the source positions once on the first frame. If the observations were not guided and the sources do tend to drift over the frames, then the source positions are determined on each frame with a slightly longer run time associated with this script. Note that if no sources are found, the script prompts the user to lower the significance level in order to allow the detection of sources. In the case where more than 10 sources are detected with the parameters, the construct_windows.py script is automatically executed and it allows the user to eliminate any of the sources that are within close proximity to one another and sources that are too close to the edge of the frames. Note that a "windows" file bypasses this entire step to find the positions of sources, but the standard deviation of the background as well as the required significance level are still needed for the sources to be actually detected.

With the user's permission on the correct source positions, the respective "parameter" files are set up as a pre-photometry step. Now that the pipeline "knows" where the sources are located,

the instrumental magnitudes are determined by the IRAF packages noao, digiphot, daophot task phot, after the parameter files datapars, centerpars, fitskypars and photpars (Davis et al., 1994) have been altered or left in a default state. Each of these parameter files are necessary for successful photometry to commence and the default values are supplied within the "defaultparameters" text file that came with the SHOC pipeline. These "defaultparameter"-values can be altered if needed, for instance, the first entry of this text file is a list of aperture sizes which are used during aperture-corrected photometry. If this entry were to be changed to a single value, it would facilitate fixed-aperture photometry. Various parameters can be adjusted according to the user's preference. During PHOTscript the pipeline asks the user whether the default parameters should be used or if any changes need to be made to the respective entries, as seen in Fig. 6 (parameters should be changed to the appropriate values required by the users's field).

```
#########################################################################
CONTENTS OF THE 'parameters' FILE IN THIS DIRECTORY IS:
#########################################################################

#  List of trial apertures for aperture-corrected photometry [pixels]   -   Specify a single aperture for FIXED aperture photometry
#    these should be smaller than the largest star's aperture
0.5,1,1.5,2,2.5,3,3.5,4,5,6,7,8,10,12,15

#  Background : inner annulus [pixels]
#    should be at least 1 more than largest trial aperture
15

#  Background : outer annulus [pixels]
#    should at least 1 more than inner annulus, but preferably less than min separation distance between sources
20

#  Centroid box size [pixels]
#    it should preferably not exceed the maximum trial aperture or minimum separation distance between sources
15

#  Maximum shift for centroid [pixels]
#    it should not exceed the minimum separation distance between sources
5

#  Minimum distance for sources from the edge [pixels]
#    only used to eliminate edge sources if more than 10 sources are found
20

#  Minimum separation distance between sources [pixels]
#    only used if you want to eliminate crowding if more than 10 sources are found
10

#  The maximum magnitude error permitted [mag] for aperture-corrected photometry
#    points are ignorred if MagErr > this max limit
0.1

#  The maximum frame-to-frame drift allowed for centroids [pixels]
#    should not exceed the minimum separation distance between extracted sources
3

#  The FWHM of the PSF [pixels]
#    is 3 for good sampling and 1 for severe under-sampling (ideal sampling is PSF FWHM ~ 2.333 pixels)
3
#########################################################################

Do you wish to continue with the photometry using the parameters listed above (Y/N)?
```

Figure 6: Default parameters to be used by the various parameter files of the IRAF noao, digiphot, daophot task phot.

In the case where fixed-aperture photometry has to be done, the successive parameters need to be changed accordingly as described in the comments of the parameters text file. The background signal, which is present within the trial aperture, is defined as the region between an inner background annulus (to be at least 1 pixel more than the largest trial aperture) and an outer background annulus (smaller than the minimum separation distance between sources and at least 1 pixel larger than the inner background annulus). These sizes are radii in binned pixels just like the optimal aperture size(s). The fitskypars[23] uses an algorithm to determine whether the background counts are median or mean distributed and is the preferred mode for crowded stellar fields. This algorithm is iterated a maximum number of 10 times. The resultant background value within a pixel is then multiplied by the area of the aperture and subtracted from the summed counts contained within

[23] http://stsdas.stsci.edu/cgi-bin/gethelp.cgi?fitskypars

the photometric aperture of all the respective sources identified for a given frame.

The first step for photometry is to identify the "optimal" source with its given list of optimal apertures per frame responsible for the highest SNR. This is done by determining all of the respective instrumental magnitudes per source per frame for every aperture size listed in the aperture list. The latter information is used to generate the curve of growth (COG) and returns the smallest aperture (optimal aperture in radius) that maximizes the SNR (the inflection point in the curve of growth) per source per frame. All of the optimal apertures from all of the frames are averaged per source to return the average optimal aperture per source for the entire observation. These apertures tend to be floats even though in practice these decimal values would only contribute when rounding to the nearest integer. The "optimal" source with the smallest average optimal aperture over the entire observation can then be identified. This step is done so that the instrumental magnitude scale of daophot can be set up as it is directly dependent on this optimal aperture of the "optimal" source to derive the instrumental magnitude. The optimal aperture size together with the exposure time, the "zmag" parameter set in photpars and the zero point of magnitude scale value (set to 0 in the Photometry.py script) are used to compute instrumental magnitudes for the rest of the sources as discussed in the next paragraph.

With the instrumental magnitude scale now calibrated (in terms of the "optimal" source), the second step for photometry can now be executed by using these optimal apertures of the "optimal" source per frame as the new input apertures list for the IRAF noao, digiphot, photcal task mkapfile (Davis, 1999) to determine the corresponding instrumental magnitudes for all of the sources per frame. Even if the optimal aperture for the "optimal" source in a specific frame is not the smallest of all the source's derived optimal apertures, the "optimal" source's optimal aperture will still be used to determine all of the instrumental magnitudes for all the sources. These instrumental magnitudes are relative to the detection threshold and more could be read about this in "A Reference Guide to the IRAF/DAOPHOT Package" by Lindsey Davis (Davis et al., 1994). Since the detection threshold was already set as done in Fig. 5 the derived instrumental magnitudes for the remaining sources are all negative as they are several orders of magnitude brighter than this threshold as shown on the axes of the light curve plots in Fig. 8 and Fig. 9 below.

For example, let source A be the source that produced the smallest average optimal aperture size over the entire observation, i.e. the "optimal" source. The mkapfile is then used to determine the instrumental magnitudes of each source using source A's derived optimal aperture for that specific frame. Assuming that in frame 1 the optimal aperture for source A was derived to be 5.33 binned pixels in radius and two other sources, B and C, had optimal apertures of 3.7 and 6.2 binned pixels in radius. The instrumental magnitudes would be determined for all sources using an aperture size of 5.33 binned pixels in radius. This process would continue over all of the remaining data frames.

However, there are a few problems with this method. For instance what if the designated "optimal" source is not the target source in which you are interested? The pipeline would not use the correct aperture size that maximizes the SNR over the target source, but rather maximize the SNR of the designated "optimal" source within each frame. Therefore, where necessary, a "windows" file is used to bypass this problem, as the user can specify the coordinates of sources that produced a larger average optimal aperture (brighter sources within the field) than the user's source of interest. In the special case where only one other star is available for differential photometry, and it managed to produce the smallest average optimal aperture, a suggested method to bypass this

problem is to redo the photometry section with fixed-aperture photometry based on the average optimal aperture derived for the target source.

If an error does occur stating that the curve of growth failed to converge, the maximum-magnitude-error-permitted within the parameters file (as shown in Fig. 6) can be increased. Furthermore, the maximum-shift-for-centroid parameter and the maximum-frame-to-frame-drift-allowed parameter can be increased whilst still obeying some conditions as mentioned in the comments of the "parameters" file. If all of these attempts still manage to manifest the same error, a slightly larger fixed aperture size usually solves the problem.

2.1.5 PLOTscript

A flow chart of the PLOTscript with section numbers in italics for reference is provided in Fig. 7.

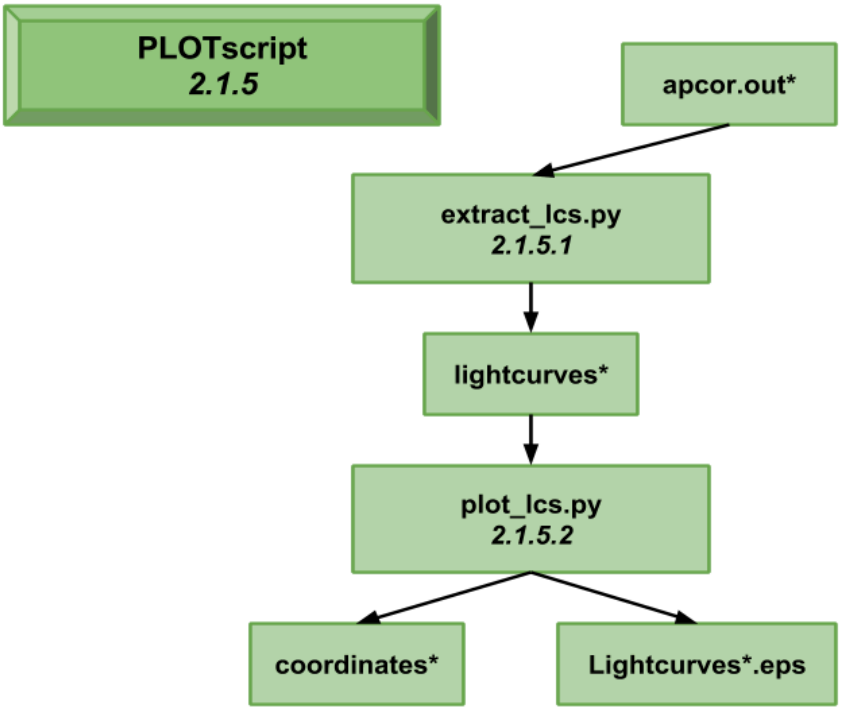

Figure 7: Flow chart of PLOTscript with section numbers (in italics) provided for reference to the corresponding script descriptions in this thesis.

2.1.5.1 extract_lcs.py

This PYTHON script extracts all the light curves for the desired sources that were detected or mentioned within the "windows" file. It is also used to extract the following information for each source on every frame in its output text file: source number, X-coordinate, Y-coordinate, seconds from midnight, instrumental magnitude, error in instrumental magnitude, optimal aperture size, file name, start of the exposure (UT) and HMJD. This output file is used to do differential photometry on the target source as described in section 2.2 below.

2.1.5.2 plot_lcs.py

This PYTHON script uses the output file from section 2.1.5.1 to produce GNUPLOT scripts. Plots are produced by using an appropriate magnitude range as defined by the user. This script's results serve as a quick way to visualize the raw light curves of the source(s) but were not included in any of the plots shown within this thesis as a separate PYTHON script was made specifically for this.

2.1.6 Differential photometry scripts

The original pipeline tar folder included two differential photometry scripts to produce differential light curves of the target source. However, the resultant differential light-curve plots were instrumental magnitude versus seconds from the start of the datacube. The desired result was a differential light-curve plot of the target source, but with the flux ratio versus seconds from the start of the datacube and not in units of instrumental magnitude. Hence these scripts were omitted during the pipeline process and additional PYTHON scripts were developed to replace these scripts for each event.

2.1.7 QuickLook.py

The sole purpose of this entire PYTHON script is to provide the user with a quick result that displays the data quality as well as the source variability in the form of a raw light curve. This script avoids the timely reduction processes and some header information is unpopulated to speed up the run time of this script. The SHOC-, PHOT- and PLOTscripts are automatically executed during this compact version and the user should be mindful that the raw light curves produced are not suitable for publication.

Also note that the original SHOC pipeline is designed to run with the dependencies as set up on the SAAO ASTRO servers and was used as the basis for the following pipelines.

2.1.8 MORIS

Due to the similarities between the SHOC instruments and the MORIS instrument as mentioned in section 1.3.2.2, the SHOC pipeline was altered to accommodate the MORIS instrument. The result is known as the MORIS pipeline. This pipeline was solely developed for the Orcus.20170307 event. The following changes or alterations were done to accommodate this instrument: firstly, to include the MORIS instrumentation specifications[24] in the "ReadoutNoiseTable" which is only used to extract the needed information when the "RON" and "SENSITIVITY" headers are missing. Other changes included supplying the pipeline with the correct deadtime for MORIS where needed (Gulbis et al., 2011), which was calculated by multiplying the number of rows in the CCD, 512 rows, with the vertical shift speed of the instrument, 3300 $\times 10^{-9}$ seconds, resulting in a deadtime of 0.0016896 seconds.

Another change that needed to be included was the site information of the IRTF which was covered in the irtf.dat file included in the IRAF observatory database. Also note that just like the SHOC pipeline, the MORIS pipeline is supported to run with the dependencies as set up on the SAAO ASTRO servers.

[24] http://occult.mit.edu/instrumentation/MORIS/Documents/Ixon_X3020_SpecSht.pdf

2.1.9 LCO

With the inclusion of the global telescope network of the LCO, there was a need to process data in a similar manner to ensure some consistency of the results across various instruments. By also including more instruments located all around the globe, we also increase the likelihood of a chord detection or even a multi-chord detection. In many cases, events were scheduled for observation on multiple instruments, for example LCO and SHOC. Thus the purpose of this pipeline was to treat the LCO data in a similar way as we do with the data from other instruments. This pipeline, however, does not include the reduction steps as mentioned in sections 2.1.3.4-2.1.3.7, as the data from the LCO guide cameras needs to undergo dark frame corrections. Neither the SHOC nor MORIS pipeline accommodates this reduction step. Hence the pipeline skips all of the reduction steps (as it was not seen as an impeding task at the particular time of development) by simply using the already BANZAI[25]-reduced images made available in the LCO data archive. The BANZAI pipeline calibrates the science frames by masking any bad pixels that the imagers might have and also reduces (bias, dark and flat) the science frames accordingly. Since most of the scripts from our LCO pipeline have their origin from the SHOC pipeline, a short discussion follows on how the data were prepared to be in the format needed by the LCO pipeline and what the LCO pipeline actually does.

Each of the BANZAI-reduced images is assigned a name that contains information about the site where the telescope is situated, the size of the telescope, which guider camera was used and a BANZAI-reduced extension (e91). This format is very different from the names allocated to the SHOC frames (instrument_YYYYMMDD.cubenumber.fits) which undergo the removal of extraneous prefixes to be replaced with shorter names for IRAF (e.g. sYYYYMMDD.cubenumber.imagenumber.fits) and serves as a standard procedure throughout all the data pipelines. The PYTHON script, LCOlist.py, executes this very task to decrease the lengthy names assigned to the LCO images and rename them in the correct format. It then provides an output text file, "LCOsorted", that lists all of the new names of the LCO images that are now ready to be run through the LCO pipeline.

The LCOpipeline.py script executes two things: it assigns the correct variables to the correct header information needed by the pipeline and it sets up the LCOscript, PHOTscript and PLOTscript. Since the LCO images are not supplied in the datacube format there was no need for sections 2.1.3.1, 2.1.3.2 and 2.1.3.3. However, the timing information needs to be converted into the right format and placed into a new header for photometry to commence. This is done in the frametime.py script which appends a new "UTC-OBS" header to each frame. Also note that the latter script is included in the LCOscript and is the only script of the entire pipeline that needs to be run on the SAAO ASTRO2015 server. Adding a new header keyword to an already header-altered FITS image seems to be problematic with the older versions of IRAF and requires some further investigation in the future.

PHOTscript and PLOTscript have had little to no alterations made to them.

The LCO pipeline needs to be run independently for each guide camera as the results from all of the guide cameras need to be combined afterwards for an increase in spatial resolution. For some consistency over the data from the respective guide cameras, the selection of comparison stars was chosen as such to be present on all of the frames from the various guide cameras.

[25] https://media.readthedocs.org/pdf/banzai/latest/banzai.pdf

2.2 Light curve production

Datasets that were acquired for each of the events listed in Table 1 were run through the relevant pipelines, where photometry was carried out to produce light curves of instrumental magnitude versus seconds from when the observation was started. Individual, differential-photometry scripts were then responsible for transforming the raw light curves into differential light curves by calibrating the target star with the combined signal of the comparison stars. Details on the instrument-specific, light-curve-production process of each event are discussed below, in order of past to most current events.

2.2.1 Pluto.20160719

2.2.1.1 Shocnawe on the 74"

The 8000-image datacube was run through the SHOC pipeline, where the information within the single datacube header was updated with the correct information due to the external GPS-triggering mode being activated during the observation. Consequently, new headers were created and assigned to their respective FITS images that were contained in the datacube. The newly, header-updated images were calibrated using bias frames taken on the night of the event and sky flat frames taken on August 8 2016 on the 40-in telescope with the Shocnawe instrument. The availability of comparison stars within the science frames was limited to a single on-chip star. The comparison star was brighter compared to the target star by about one order of instrumental magnitude, with the average magnitudes being -12.59 and -11.88, respectively. The SHOC pipeline was able to calculate all instrumental magnitudes for the two stars in the field using aperture-corrected photometry which optimizes the SNR as discussed in the previous section. The average optimal aperture for the target star was 6.9 binned pixels (4.20 arcsec), which was smaller than that of the comparison star's 9 binned pixels (5.47 arcsec) aperture. Thus, no fixed-aperture photometry was needed. Fig. 8 and Fig. 9 serve as a demonstration of the raw light curves produced by the SHOC pipeline for the target star and the comparison star.

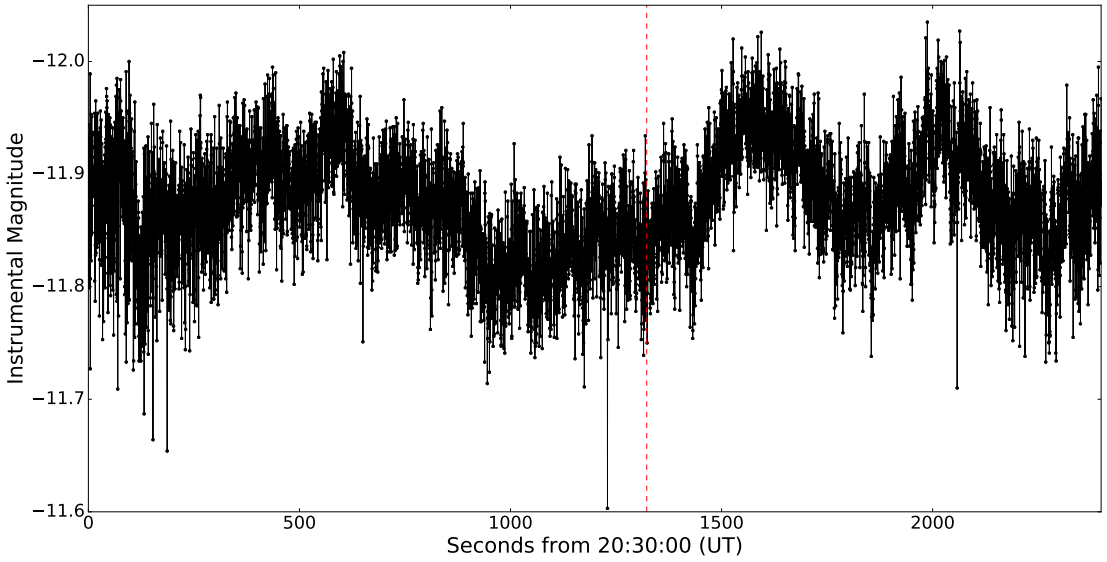

Figure 8: The raw Shocnawe light curve showing the instrumental magnitude versus time of the target star for the Pluto.20160719 event. The dashed line represents the predicted midtime, 20:53:03 UT, for this event.

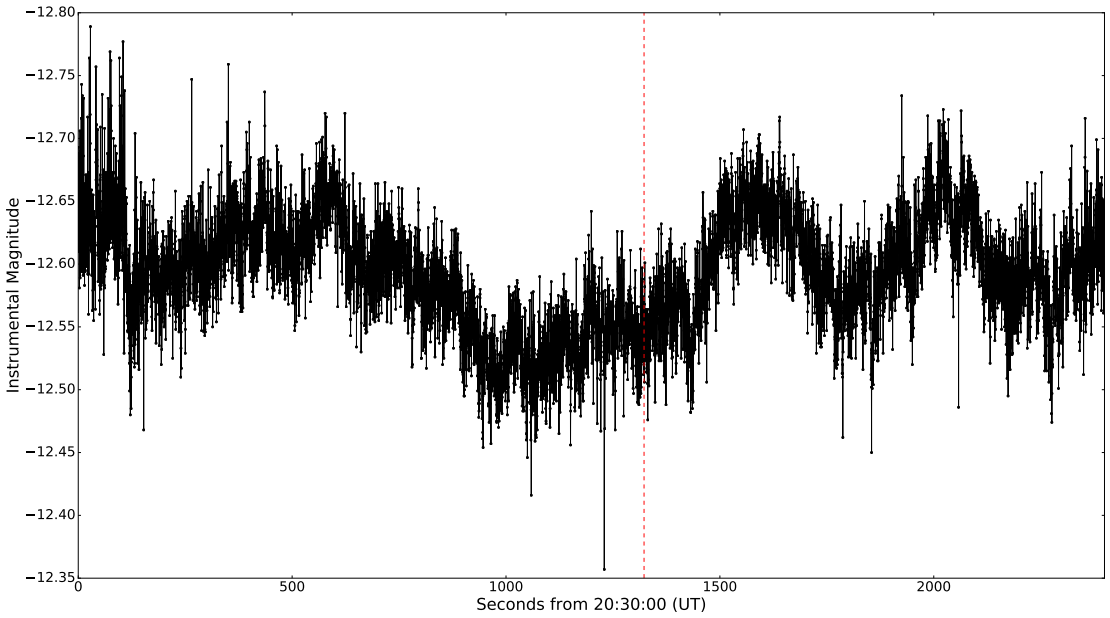

Figure 9: The raw Shocnawe light curve showing the instrumental magnitude versus time of the comparison star for the Pluto.20160719 event. The dashed line represents the predicted midtime, 20:53:03 UT, for this event.

Figure 10 is the differential light curve of the target star after it was calibrated by the comparison star's signal and demonstrates that no signature of a stellar occultation event was present. Only the differential light curve plots will be displayed for the remaining events in this section.

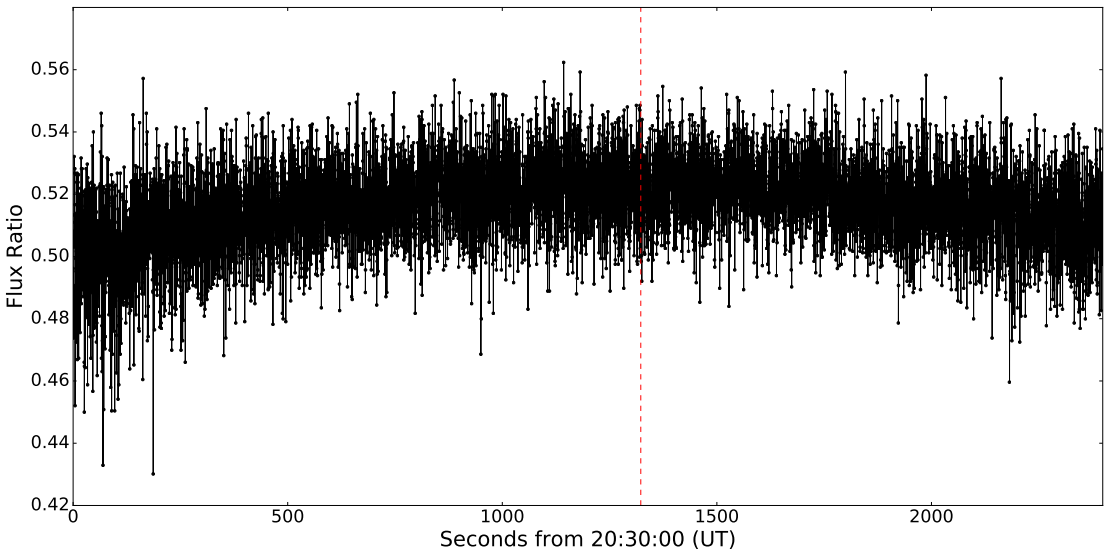

Figure 10: The Shocnawe differential light curve showing the flux ratio versus time of the target star for the Pluto.20160719 event. The plot above is the data shown in Fig. 8 divided by that shown in Fig. 9. The dashed line represents the predicted midtime, 20:53:03 UT, for this event.

2.2.2 Haumea.20170121

2.2.2.1 Shocnawe on the 74"

The predicted midtime of 02:52:51 UT for this event was particularly close to sunrise. Thus an increase of the background signal was to be expected during the entire observation. The event coordinates were just on the pointing limits of the 74-in telescope near the predicted midtime. With the 74-in positioned on the pointing limit, data were taken as soon as possible. Data collection however, could only be done at about 744 seconds after the predicted midtime. After a positive confirmation of the target field, the target as well as the only available comparison star were positioned accordingly on SHOC, where guiding could only commence from frame 80 onwards of the total 295-image cube. Sunlight was starting to saturate the last 8 images of the datacube and hence, the target star was lost during these frames and they were excluded from the light-curve-production process.

An initial trial run with the SHOC pipeline resulted in average optimal apertures of 7.34 binned pixels (5.58 arcsec) and 7.74 binned pixels (5.62 arcsec) for the target and comparison star, respectively. These results were then used as a guideline for fixed-aperture photometry as very few instrumental measurements were made while doing aperture-corrected photometry of the target star. Hence, the SHOC pipeline was supplied with calibration frames (bias and flat frames), a windows file that contained two sets of coordinates and a fixed-aperture size of 7 binned pixels (5.32 arcsec) to enable the determination of 197 instrumental magnitudes for the target star and 207 instrumental magnitudes for the comparison star. The reason for the inconsistency in measurements for the two sources is because the comparison star is almost 2 orders of instrumental magnitude brighter than the target star. The comparison star has an average instrumental magnitude of -9.23 and -7.77 for the target star. The increasing background essentially results in fewer measurements made for the fainter stars in the target field, which in this case is the target star. The length inconsistencies in the instrumental magnitude arrays of the two sources required a custom script for differential photometry. Fig. 11 is the resulting differential light curve for the target star and shows no signature of a stellar occultation event being captured.

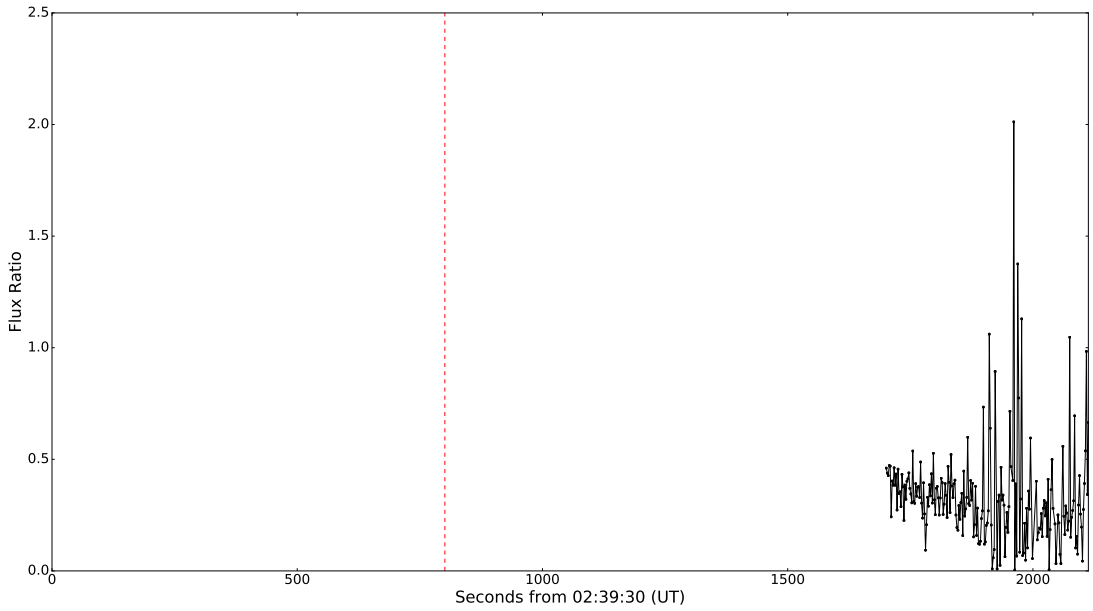

Figure 11: The Shocnawe differential light curve showing the flux ratio versus time of the target star for the Haumea.20170121 event. This event was missed due to telescope pointing constraints surrounding the predicted midtime of 02:52:51 UT, as shown here by the dashed line.

2.2.2.2 Shocndisbelief on Lesedi

The predicted midtime for this event, as mentioned above, was particularly close to sunrise, which caused the mirror cover of Lesedi (still under commissioning at that time) to close at around frame number 412, or, roughly, at 03:00:00 UT. Several images were lost during this period (frames 412 to 447) which lasted for ∼105 seconds. The background noise kept increasing towards the end of the observing cube as the Sun rose, resulting in the non-detection of our sources throughout several other frames. Of the 520 images taken, 36 images were lost due to the mirror cover closing and the last 20 frames were bordering on the non-detection of our sources due to sunrise.

The occultation datacube of 520 GPS-triggered images was run through the SHOC pipeline where several on-chip comparison stars were available for differential photometry. However, the combined signal of the two brightest comparison stars resulted in the highest SNR and were therefore selected to calibrate the target's signal to produce a differential light curve. The SHOC pipeline was supplied with calibration frames (bias and flats), a windows file that contained three sets of coordinates and the maximum-magnitude-error-permitted parameter was adjusted to 0.5 magnitude to enable the determination of 461 instrumental magnitudes for the target star, 484 instrumental magnitudes for the first comparison star and 485 instrumental magnitudes for the second comparison star. The number of measurements made for all three point sources were inconsistent and the reason for this was due to varying brightness between the individual sources. Fainter stars were harder to detect with an increasing background, while brighter stars were still detectable. The first comparison star had an average instrumental magnitude of -11.65, with -11.51 for the second comparison star and -7.52 for the target star. Therefore the increasing background resulted in fewer measurements made for the fainter stars, which in this case is the target star. A custom differential photometry script was developed to accommodate the length inconsistencies of the three instrumental magnitude arrays. The average optimal aperture for the target star was 3.96 binned pixels (5.31 arcsec) using aperture-corrected photometry and was the smallest between 9.14 binned

pixels (12.25 arcsec) for the first comparison star and 8.82 binned pixels (11.82 arcsec) for the last comparison star. Therefore, no fixed-aperture photometry was needed. Fig. 12 is the resulting differential light curve of the target star and requires further investigation on the possible pressence of a stellar occultation signature.

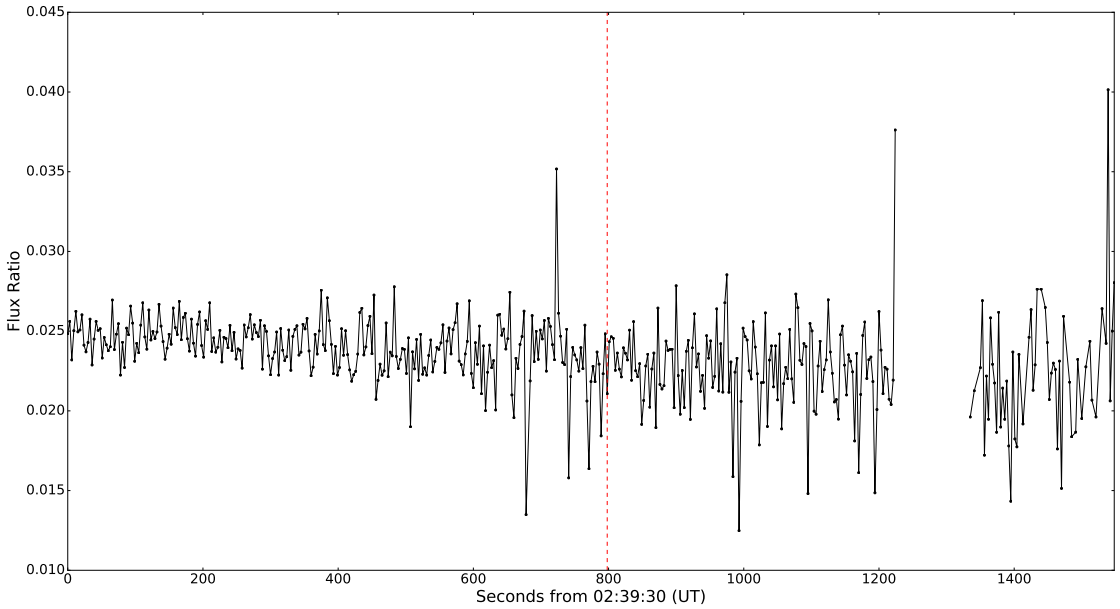

Figure 12: The Shocndisbelief differential light curve showing the flux ratio versus time of the target star for the Haumea.20170121 event. The high spike followed by a discontinuity in data to the right of the plot was due to a default setting on Lesedi's mirror covers to close at 05:00 SAST. The spike at 723 seconds and the spike at 1539 seconds from 02:39:30 UT are explained in the next few figures below. The dashed line represents the predicted midtime for this event, which was at 02:52:51 UT.

The spike that occurred at 723 seconds from 02:39:90 UT as shown in Fig. 12 above showed stable counts for the comparison stars over this period (frames 243, 244 and 245 as shown in Figs. 13, 14 and 15 below) while there was a slight change in background counts on frame 244, ∼20 counts. The increase in signal for only the target star on frame 244 of the cube is shown in Fig. 14. Although not visible on the images, the cursor was positioned on the pixel with the highest counts of the target star and the counts are shown in "Value" at the upper left corner on the images.

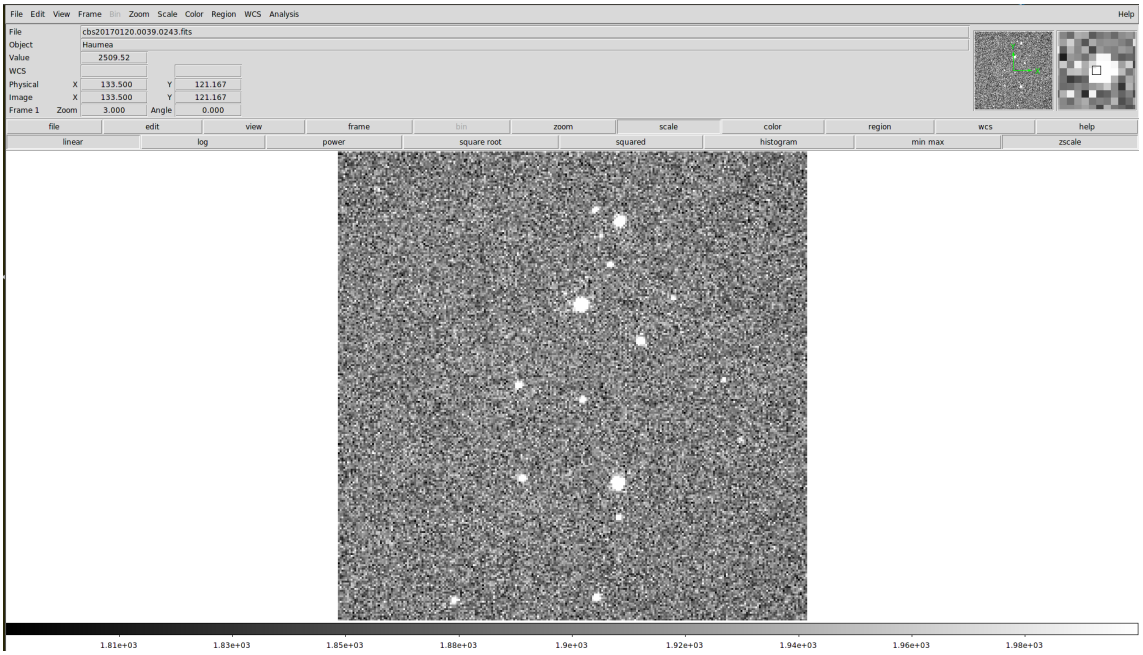

Figure 13: Frame 243 before the increase of the target star signal located in the center of the frame for the Haumea.2010121 event.

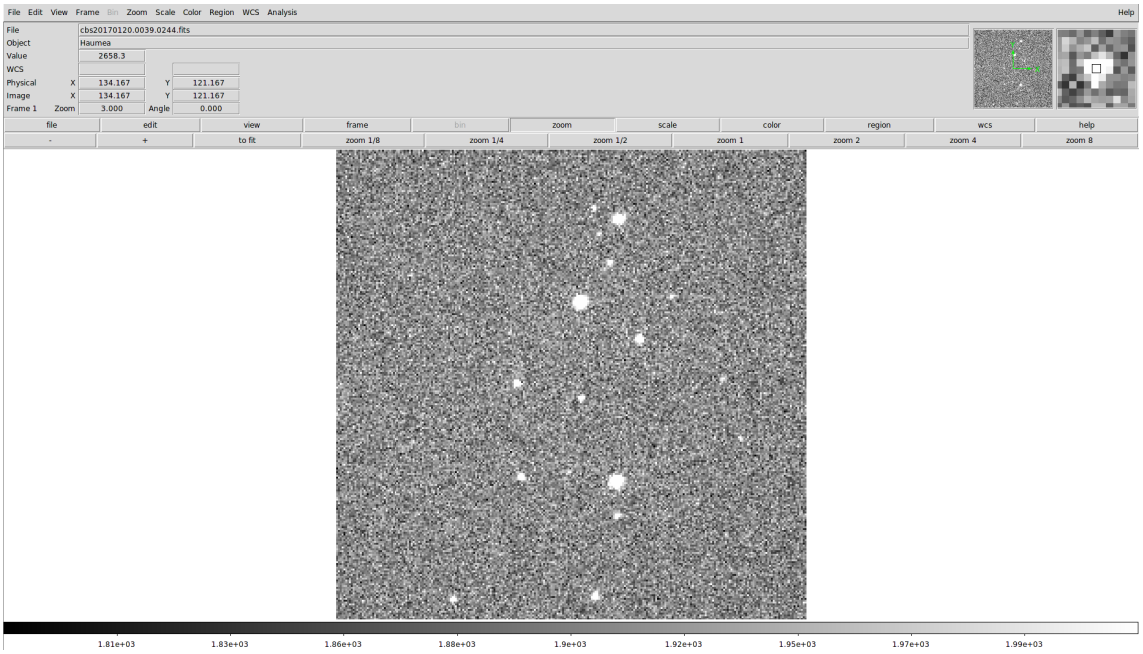

Figure 14: Frame 244 with an increase of the target star signal located in the center of the frame for the Haumea.2010121 event.

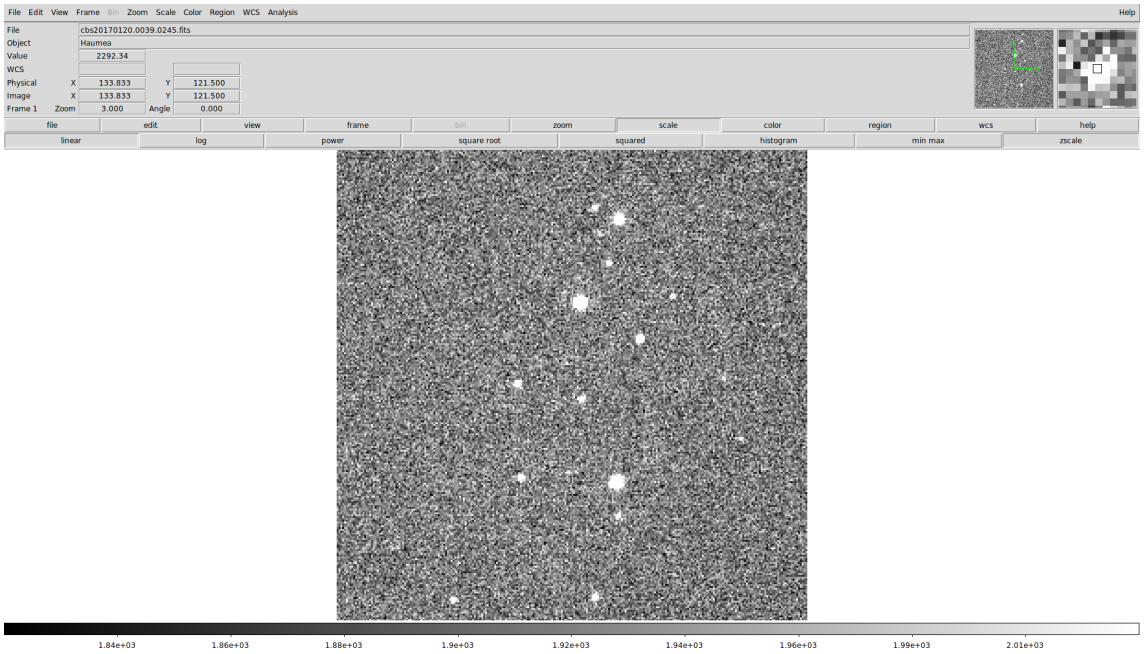

Figure 15: Frame 245 after the increase of the target star signal located in the center of the frame for the Haumea.2010121 event.

The same was done for the spike that occurred at 1539 seconds from 02:39:30 UT as shown in Fig. 12 above. This spike was due to an overall signal increase in the target star as well as the comparison stars on frame 516 of the datacube. The frame prior to frame 516 is shown in Fig. 16, Fig. 17 shows the overall increase in signal for frame 516 and Fig. 18 is the frame after frame 516. These frames were close to the end of the datacube and because the background was varying due to sunrise this spike in counts could be due to a darker background sky making the sources more visible and brighter on this particular frame.

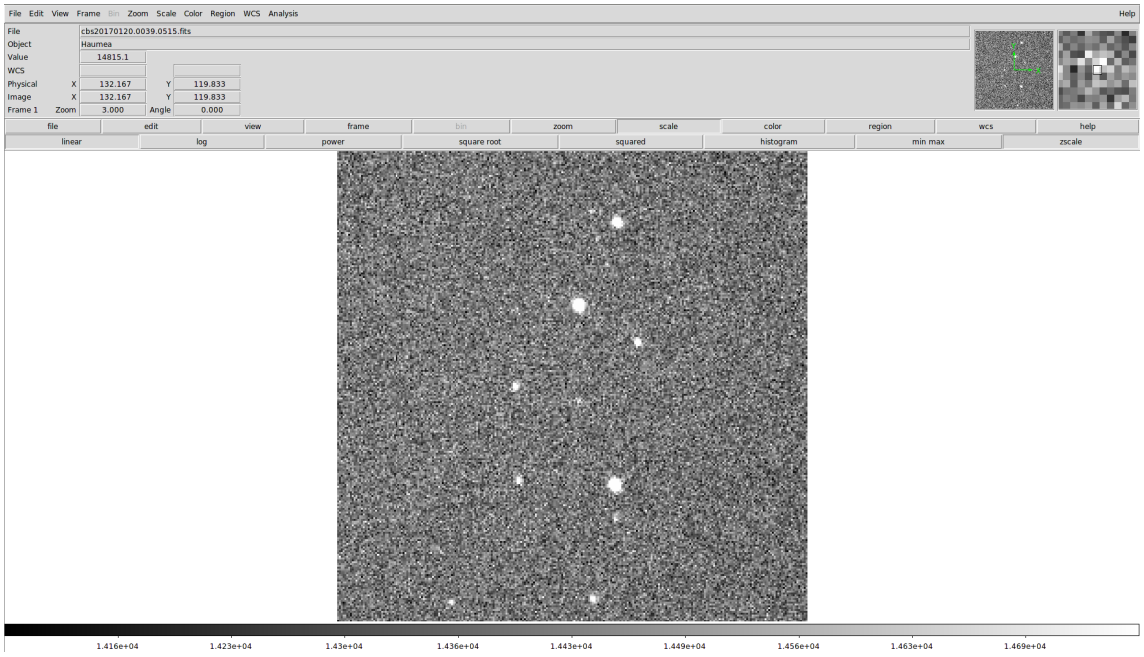

Figure 16: Frame 515 before the overall increase in source signal for the Haumea.2010121 event.

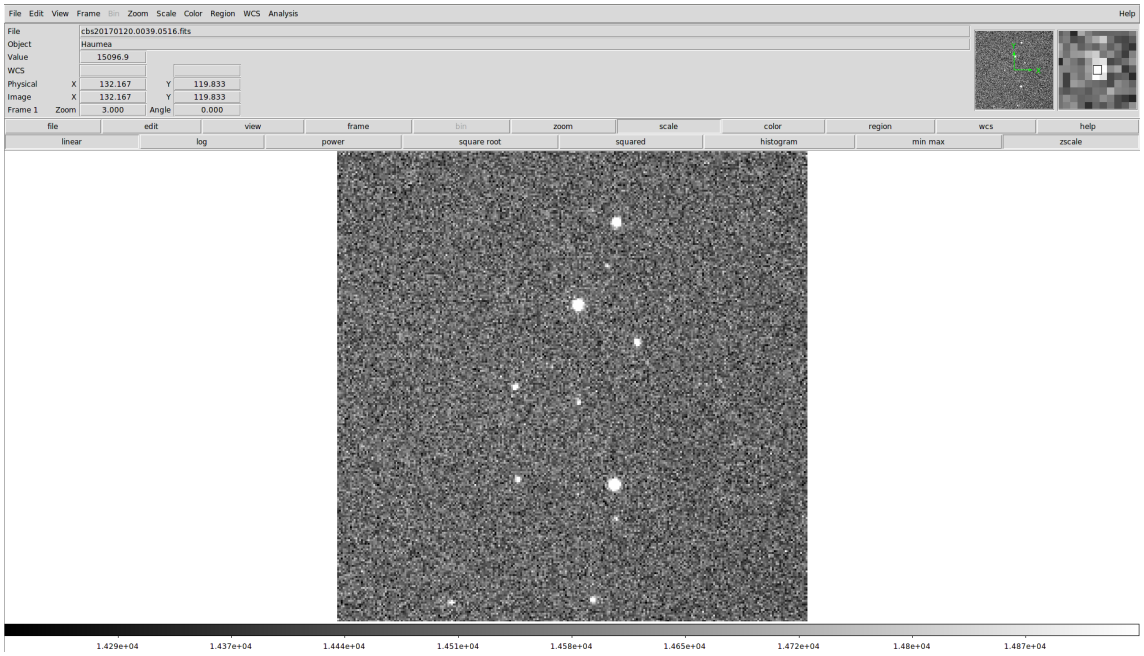

Figure 17: Frame 516 with the overall increase in source signal responsible for the spike to the right on Fig. 12 for the Haumea.2010121 event.

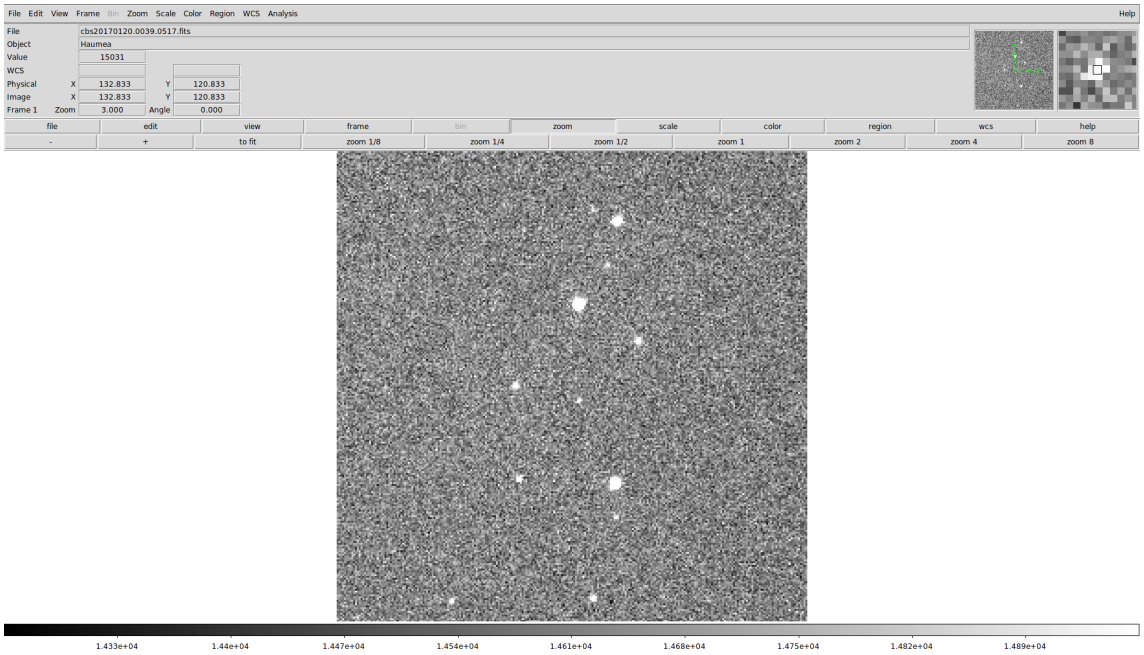

Figure 18: Frame 517 after the overall increase in source signal for the Haumea.2010121 event.

2.2.3 Orcus.20170301

2.2.3.1 LCO-ELP

All 366 BANZAI-reduced images from a single guide camera, ef01, were run through the LCO pipeline. Each image has its own individual header with its corresponding timing information being supplied within this header. The only change that the LCO pipeline does to the individual headers is to create a new header entry with the recorded observed time in the seconds-from-midnight format. The 5.7-arcminute field of view of the LCO guider cameras means that the target field contains multiple stars for differential photometry, but comparison stars were chosen based on how

close they were situated to the target star as well as their brightness while crowded stars were rejected as possible candidates. The LCO pipeline was supplied with a windows file containing two sets of coordinates (target and comparison star) and was able to calculate all instrumental magnitudes for the two stars, which was -10.01 for the target star and -11.63 for the comparison star. The average optimal aperture for the target star was 7.72 binned pixels (5.20 arcsec) and 14.8 binned pixels (9.98 arcsec) for the comparison star. Fig. 19 is the differential light curve of the target star and shows a flux-drop over two data points, indicative of a stellar occultation event being captured.

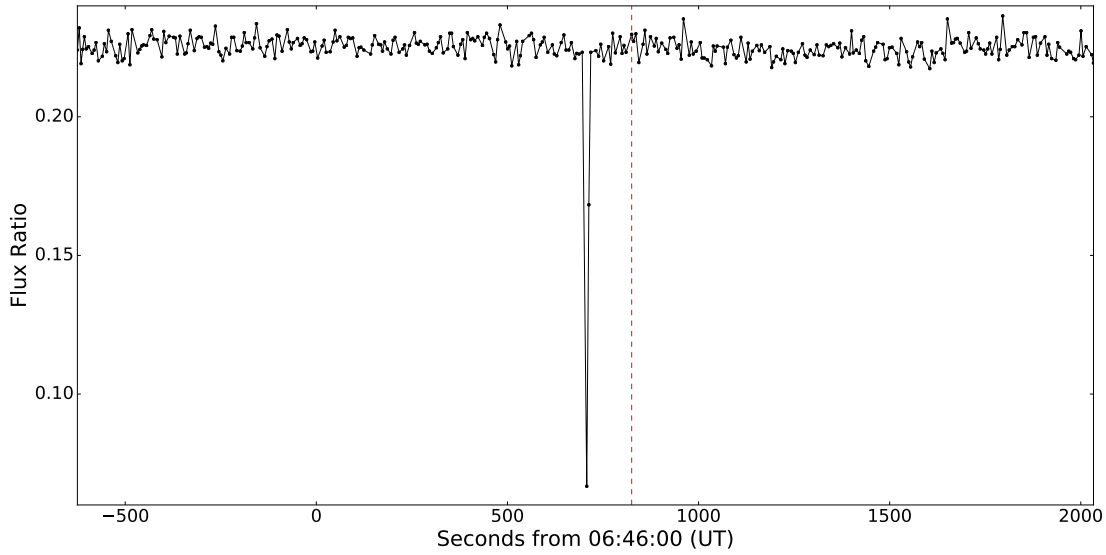

Figure 19: The LCO-ELP differential light curve showing the flux ratio versus time of the target star for the Orcus.20170307 event. The dashed line represents the predicted midtime for this event, which was 06:59:45 UT. As this plot shows, there is an offset of ∼116 seconds from the predicted midtime which will be discussed in the results section.

2.2.3.2 MORIS on the IRTF

A 26.2 MB storage restriction per file placed a constraint on the amount of images allowed per datacube, which meant that the raw MORIS data consisted of 13x 800 image datacubes and one 600-image datacube. Although the raw MORIS data taken at the IRTF were composed of several separate datacubes, the images were still taken in a successive manner. However, with the totality at 11 000 images, only a single FITS header was designated to all of the multiple datacubes. Hence all 14 of the 3D-datacubes have identical timing headers in their respective FITS header extensions. This information is only needed for the start of the observation. However, to ensure correct timing determinations for each image by the MORIS pipeline, the cubes needed to be split and then restacked to form a single 11 000 image, 3D-datacube. This was done in IRAF using the imslice and imstack commands (Barnes, 1993). With the majority of the information in the headers being the same, there is almost no loss of information during this process.

The 11 000-image datacube was run through the MORIS pipeline, where calibrations were executed by using bias and sky flat frames taken on the eve of the event. The timing information was derived by the MORIS pipeline for each individual image and supplied each of these images with a copy of the original FITS header of the datacube, but now with a newly updated timing header containing their respective timing information. With an initial trial run of the pipeline, the average optimal

aperture for the target star was 13.26 binned pixels (6.12 arcsec) and 12 binned pixels (5.54 arcsec) for the comparison star. In this case the comparison star produced the smallest average optimal aperture and was the only other star in the target field available for differential photometry. Hence, to avoid using the comparison star's optimal aperture determined for each image during aperture-corrected photometry, fixed-aperture photometry was done on both the sources. The MORIS pipeline was supplied with calibration frames (bias and flat frames), a windows file that contained two sets of coordinates and a fixed aperture size of 13 binned pixels (6 arcsec) to enable the determination of all the instrumental magnitudes for both point sources. It was also noted that the comparison star had an average instrumental magnitude of -10.06 and -10.57 for the target star. Fig. 20 is the resulting differential light curve of the target star and clearly shows a stellar occultation signature over multiple data points.

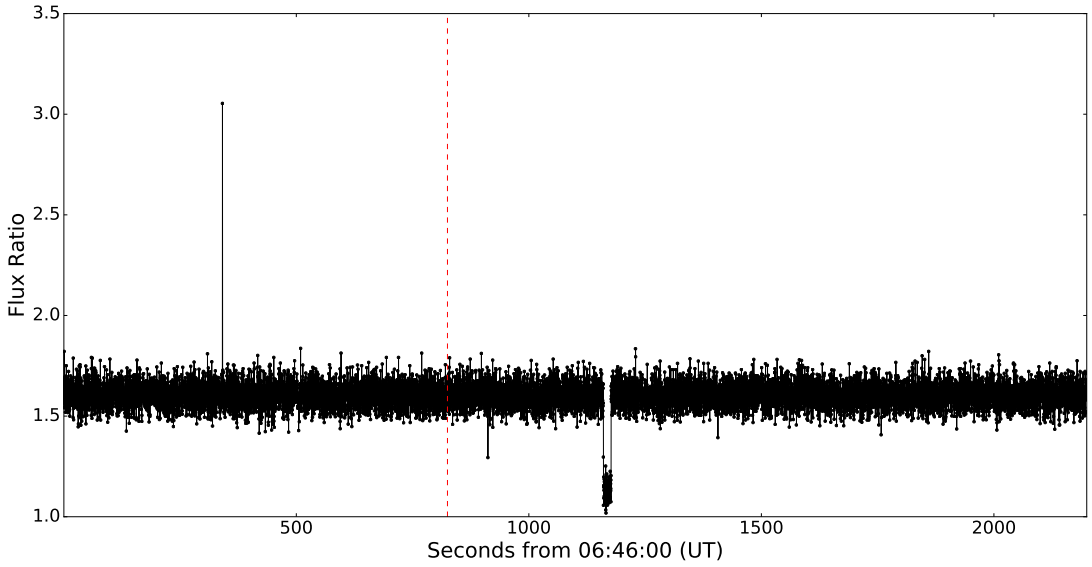

Figure 20: The MORIS differential light curve showing the flux ratio versus time of the target star for the Orcus.20170307 event. The dashed line represents the predicted midtime for this event, which was 06:59:45 UT. As this plot shows, there is an offset in the predicted midtime which will be discussed in the results section. The large spike on the left of this differential light curve plot was due to a cosmic ray being present within close proximity of the target star as shown in Fig. 21.

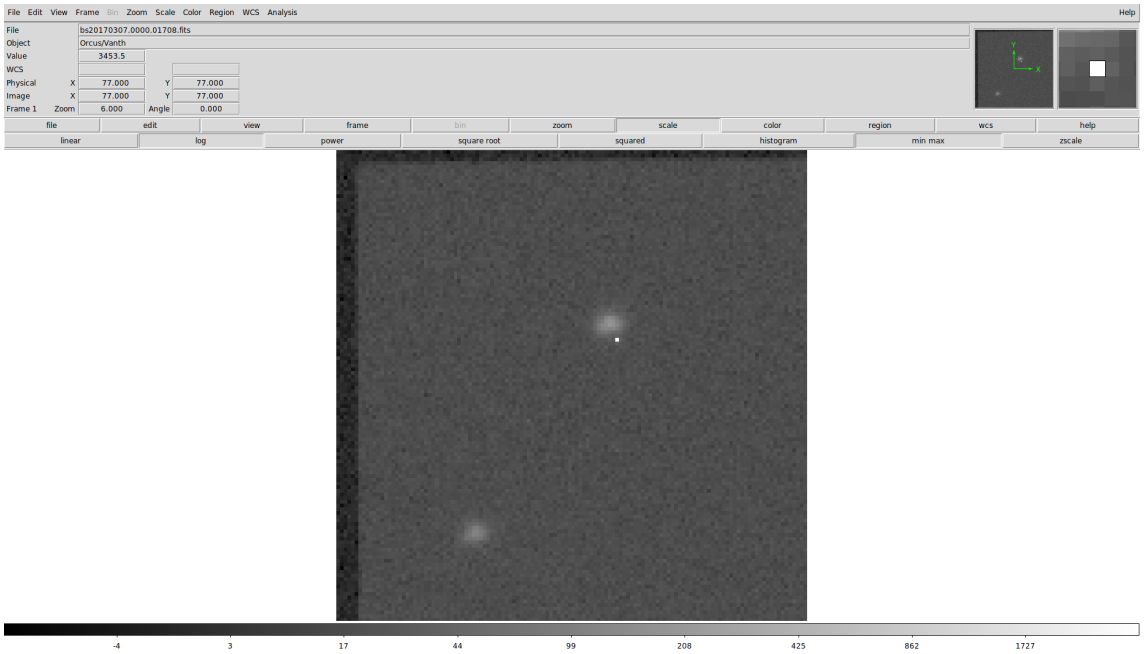

Figure 21: The cosmic ray responsible for the large spike on the left of differential light curve plot in Fig. 20 above.

NOTE: Fig. 19 and 20 show two occultation detections for this event at two different sites. The geometry and timing are currently under investigation (Sickafoose et al., 2017). More details are provided in the results section.

2.2.4 Ixion.20170505

2.2.4.1 LCO-LSC

The combined total of 1499 BANZAI-reduced images provided by three guide cameras (ef06, ef07 and ef08) were run through the LCO pipeline respectively. With a 5.7-arcminute field of view, the target field contains multiple stars for differential photometry, however the comparison stars were chosen to be within close proximity to the target star, uncrowded, bright stars that were present in the images of all three guide cameras. Only one such star was available as a comparison star. The LCO pipeline was supplied with a windows file containing two sets of coordinates (target and comparison star) and fixed aperture sizes of 16 binned pixels (10.754 arcsec), 14 binned pixels (9.436 arcsec) and 15 binned pixels (10.11 arcsec) for guide cameras ef06, ef07 and ef08 respectively. All of the instrumental magnitudes for the two stars for each guide camera were calculated respectively. The instrumental magnitude for the target star was -12.09, and -13.85 for the comparison star on guide camera ef06, -11.85 and -13.59 for the ef07 guide camera and lastly, -11.90 and -13.64 for the target and comparison star on the ef08 guide camera. The results from the three guide cameras were combined to construct a master differential light curve for this event. Fig. 22 is the resulting differential light curve of the target star and does not show the signature of a stellar occultation.

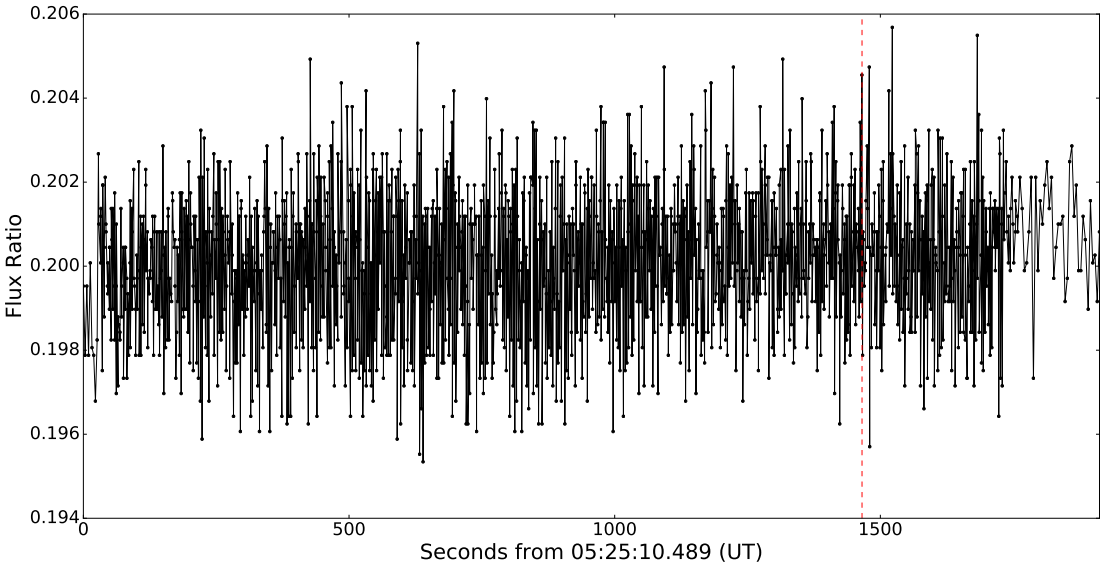

Figure 22: The LCO-LSC differential light curve showing the flux ratio versus time of the target star for the Ixion.20170505 event. The dashed line represents the predicted midtime, 05:49:36 UT, for this event. The three telescopes have staggered starting times and therefore ending times which means the data points are sparse at the start and end of the differential light curve.

2.2.5 2014MU$_{69}$.20170603

2.2.5.1 LCO-CPT

The combined total of 882 BANZAI-reduced images were recorded by two guide cameras, ef03 and ef04, and were run through the LCO pipeline respectively. With the criteria mentioned above, four comparison stars were specifically chosen that had larger average optimal apertures than the target star. The LCO pipeline was supplied with a windows file containing five sets of coordinates (target and four comparison stars) and all of the instrumental magnitudes for the five stars for each guide camera were calculated respectively. However, the combined light curve produced by (two brightest) comparison stars 2 and 4 resulted in the highest SNR and thus only their results were included here. The instrumental magnitude was -9.09 for the target star on both guide cameras, -9.37 and -9.39 for the second comparison star on guide cameras ef03 and ef04, respectively, and for the last comparison star, -10.41 and -10.42 on guide cameras ef03 and ef04. The average optimal aperture for the target star was 8.04 binned pixels (5.42 arcsec) for the ef03 guide camera and 7.06 binned pixels (4.76 arcsec) for the ef04 guide camera. For the second comparison star 9.62 and 8.02 binned pixels (6.48 and 5.41 arcsec) for guide cameras ef03 and ef04, and 11.16 binned pixels (7.52 arcsec) on guide camera ef03 and 9.9 binned pixels (6.67 arcsec) on guide camera ef04 for the last comparison star. As could be seen from these results, the average optimal aperture sizes for the target and the second comparison star on the ef03 guide camera were similar and hence the optimal aperture for the comparison on each frame was applied to all of the sources. In Fig. 23, the results from the two guide cameras were combined to construct a master differential light curve for this event with no stellar occultation signature being detected.

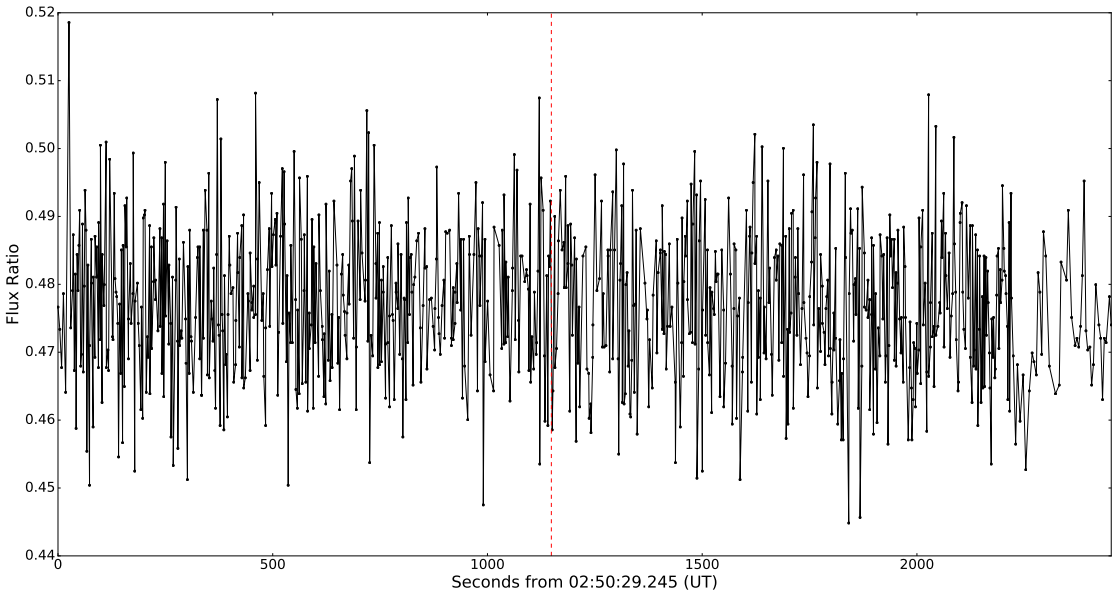

Figure 23: The LCO-CPT differential light curve showing the flux ratio versus time of the target star for the 2014MU$_{69}$.20170603 event. The dashed line represents the predicted midtime, 03:09:38 UT, for this event. The two telescopes have staggered starting times and therefore ending times which means the data points are sparse at the end of the differential light curve.

2.2.5.2 Shocndisbelief on the 74"

The datacube contained 27 000 GPS-triggered images that were initially run through the Quick-Look pipeline as a way to obtain the average optimal aperture for the target star which, was 6.16 binned pixels (3.75 arcsec). No comparison star was detected even when the significance level was decreased as suggested by the pipeline. This result was then used as a guideline for fixed-aperture photometry of the target star, as the curve-of-growth model did not converge when doing aperture-corrected photometry. The reason for this was that so many of the larger aperture sizes did not return instrumental magnitudes and would therefore prevent the calculation of optimal apertures for both of the sources. A single, on-chip comparison star was manually chosen, with its coordinates added to the windows file, as a candidate for differential photometry as no other comparison stars were detectable throughout the execution of both pipelines. Hence the SHOC pipeline was supplied with calibration frames (bias and flats), a windows file that contained two sets of coordinates (target and comparison star) and a slightly larger fixed aperture size of 8 binned pixels (4.86 arcsec) to enable the calculation of all the instrumental magnitudes for both sources. The instrumental magnitude for the target star was -10.18 and -11.42 for the comparison star. Fig. 24 is the resulting differential light curve of the target star that shows no sign of a stellar occultation being captured.

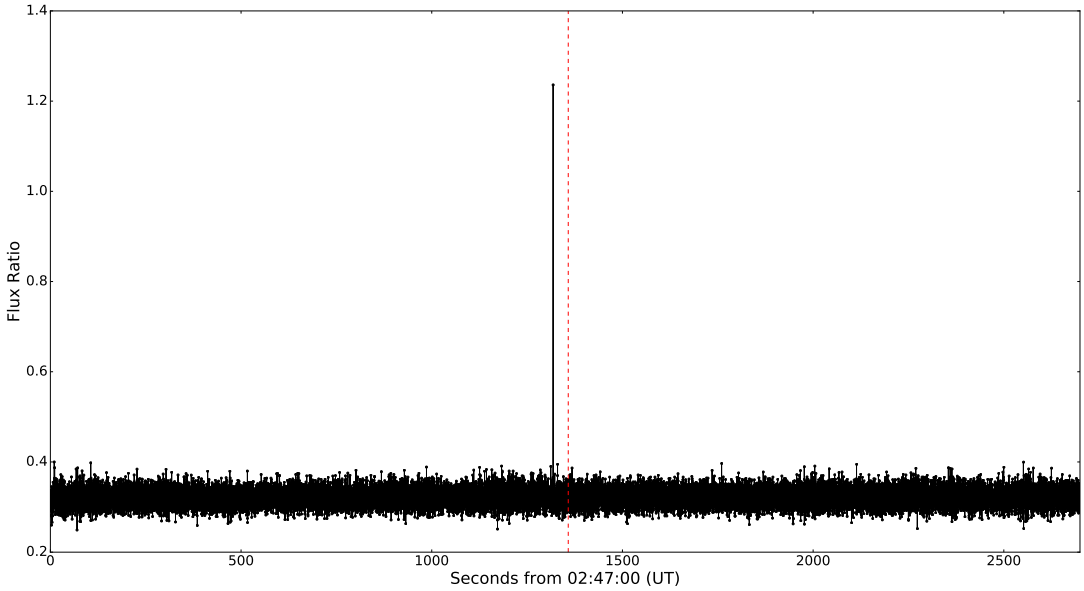

Figure 24: The Shocndisbelief differential light curve showing the flux ratio versus time of the target star for the 2014MU$_{69}$.20170603 event. The dashed line represents the predicted midtime, 03:09:38 UT, for this event. The large spike to the left of the predicted midtime was due to a cosmic ray being present within close proximity of the target star as shown in Fig. 25 below.

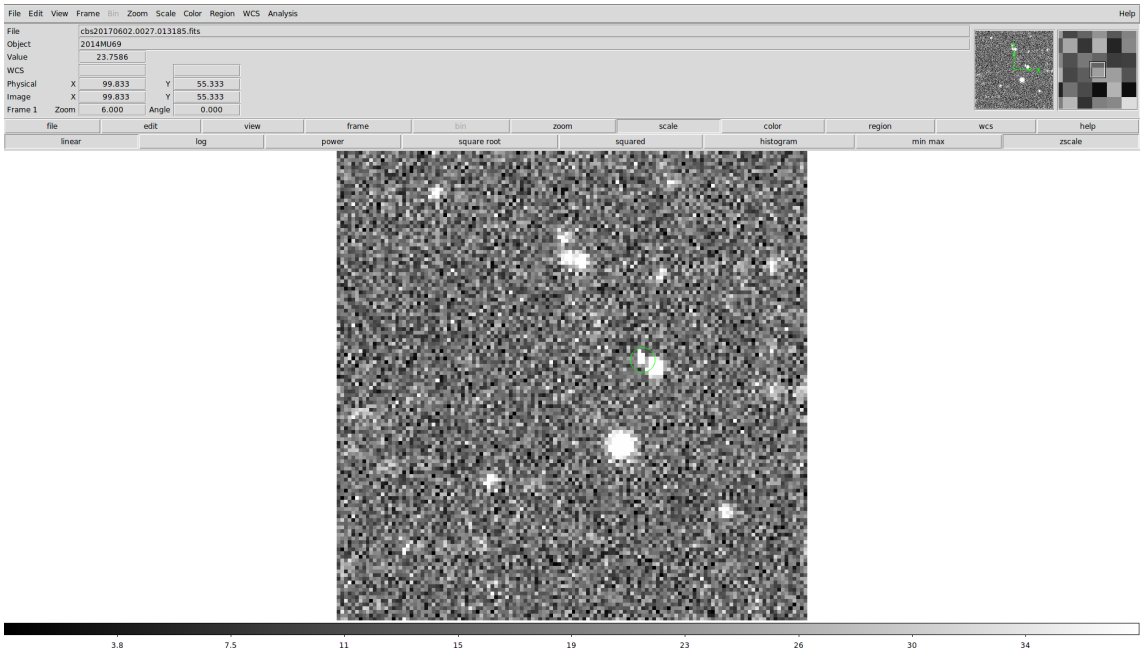

Figure 25: The cosmic ray responsible for the large spike to the left of the predicted midtime in Fig. 24 above. The green circle marks this occurrence.

2.2.6 Chariklo.20170622

2.2.6.1 Shocndisbelief on the 74"

The 7560 internally-triggered images contained within the datacube were run through the SHOC pipeline to undergo calibrations by using photometric correction frames (bias and flats) taken on the event night. Although several stars were seen on the images, most were fainter than the target star and were not chosen as comparison stars for this reason. Only a single, on-chip comparison

star was chosen for differential photometry. The SHOC pipeline was supplied with a windows file containing the coordinates for both the target star and the comparison star, an adjusted maximum-shift-of-the-centroid-box parameter of 10 pixels, a maximum-magnitude-error-permitted parameter adjusted to 0.6 magnitude and a changed maximum-frame-to-frame-drift-of-the-centroid-box parameter of 10 pixels. These parameters were slightly enlarged to ensure the tracking of the two targets over all of the images. The average optimal apertures were 13.2 binned pixels (6.01 arcsec) for the target star and 13.12 binned pixels (5.98 arcsec) for the comparison star. The comparison star was similar in instrumental magnitude (-10.7 versus -10.66) and had an average optimal aperture close to that of the target star. Because the average optimal aperture sizes were similar, the optimal aperture for the comparison star on each frame was supplied to the target. This process produced complete detection over all of the images and would not have been the case for fixed-aperture photometry. The internal-trigger mode was not designed for stellar occultations as there are some large timing errors associated with this mode of up to ±0.5 seconds as mentioned in section 2.1.3.2. However, a timing offset was recorded at 21:37 UT of -0.199534 seconds which is just a couple of minutes from when the last frame was taken at 21:34:37.69208 UT. From another offset of +0.057289 that was recorded about 15 minutes later than the first, the timing offset does not appear to have an obvious increasing or decreasing trend as it was negative closest to the end of the observation and then positive 15 minutes later. Because of the unpredictability in these offsets the first recorded timing offset of -0.199534 was subtracted from all of the times as it was only about 142 seconds late and was thus likely to be more correct than the timing offset recorded about 1042 seconds from the end of the datacube. This timing offset was only an estimate and would need further investigation for accurate timing errors. Fig. 26 is of the resulting differential light curve of the target star with no stellar occultation signature being present.

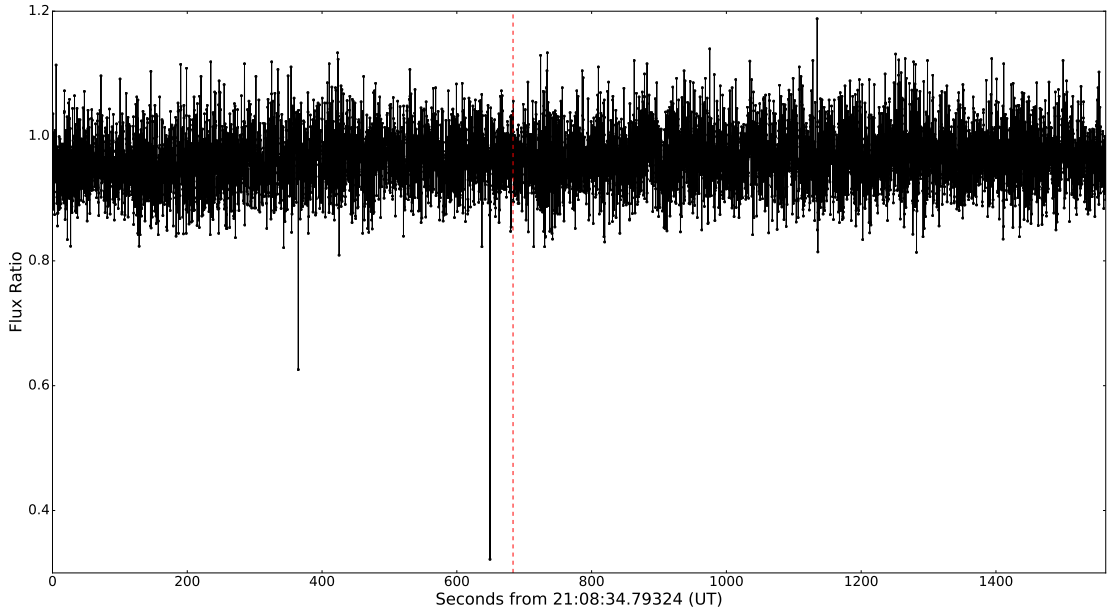

Figure 26: The Shocndisbelief differential light curve showing the flux ratio versus time of the target star for the Chariklo.20170622 event. The dashed line represents the predicted midtime, 21:19:58 UT, for this event. The two dips situated at ∼ 375- and ∼650 seconds (cosmic ray frame 1 and 2 hereafter) were due to the background subtraction of a cosmic ray present within the background annulus of the target star.

The two dips situated at ∼375s and ∼650s in Fig. 26 are due to cosmic rays and are referred to as cosmic ray frame 1 and 2 hereafter. The cosmic rays were present in frames 1765 and 3140 of the datacube. Fig. 27 shows the frame prior to cosmic ray frame 1 which is shown in Fig. 28. Similarly, Fig. 29 is the frame prior to cosmic ray frame 2 which can be seen in Fig. 30 below.

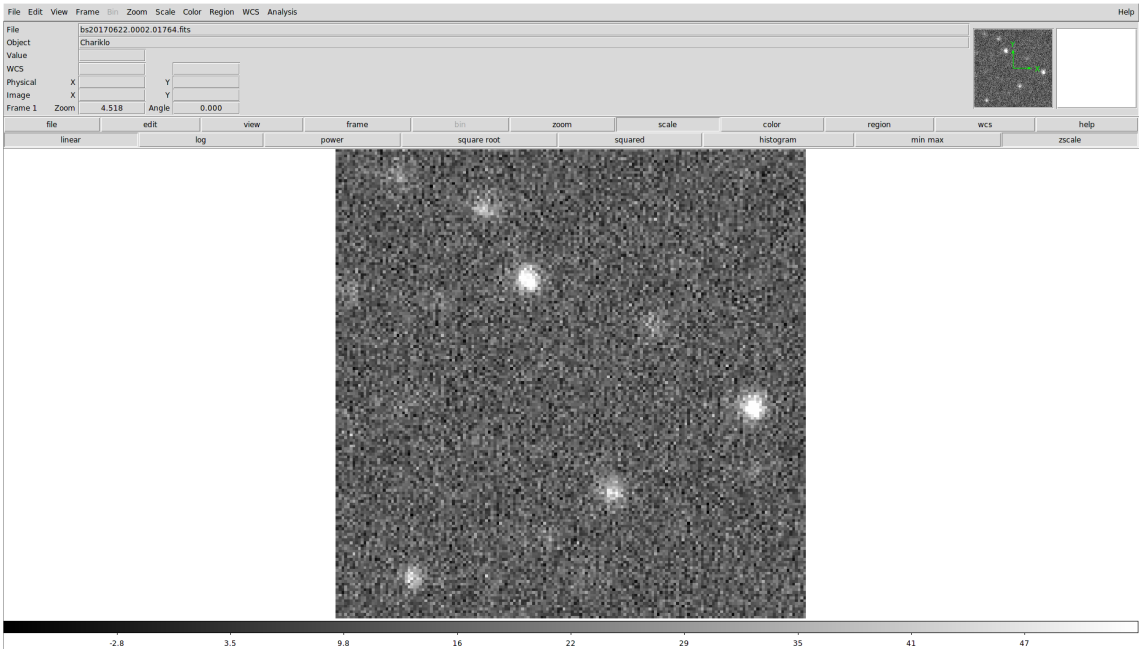

Figure 27: The frame prior to cosmic ray frame 1 as shown in Fig. 28 below.

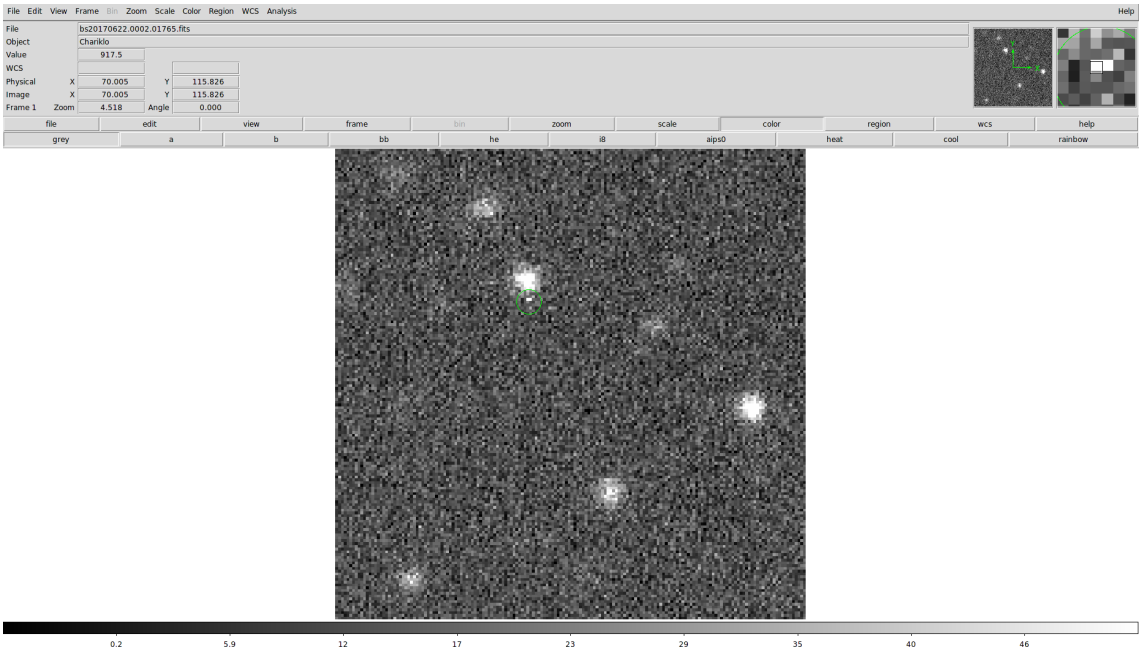

Figure 28: The frame of the cosmic ray responsible for the dip at ∼375s in the differential light curve as shown in Fig. 26 above. The green circle marks this occurrence.

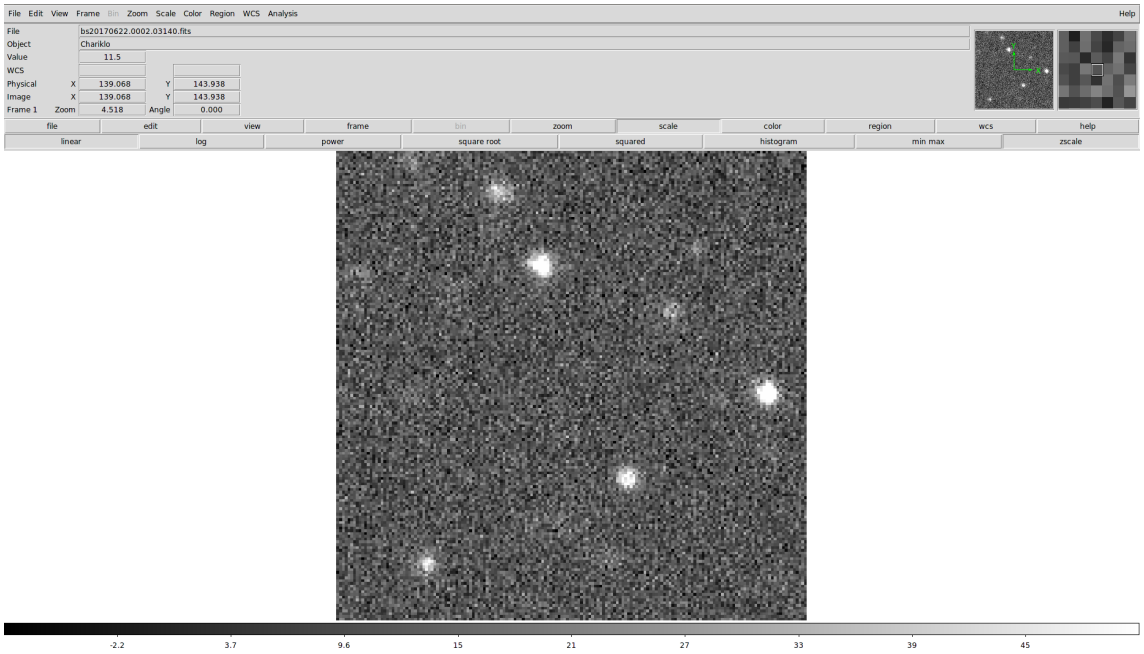

Figure 29: The frame prior to cosmic ray frame 2 as shown in Fig. 30 below.

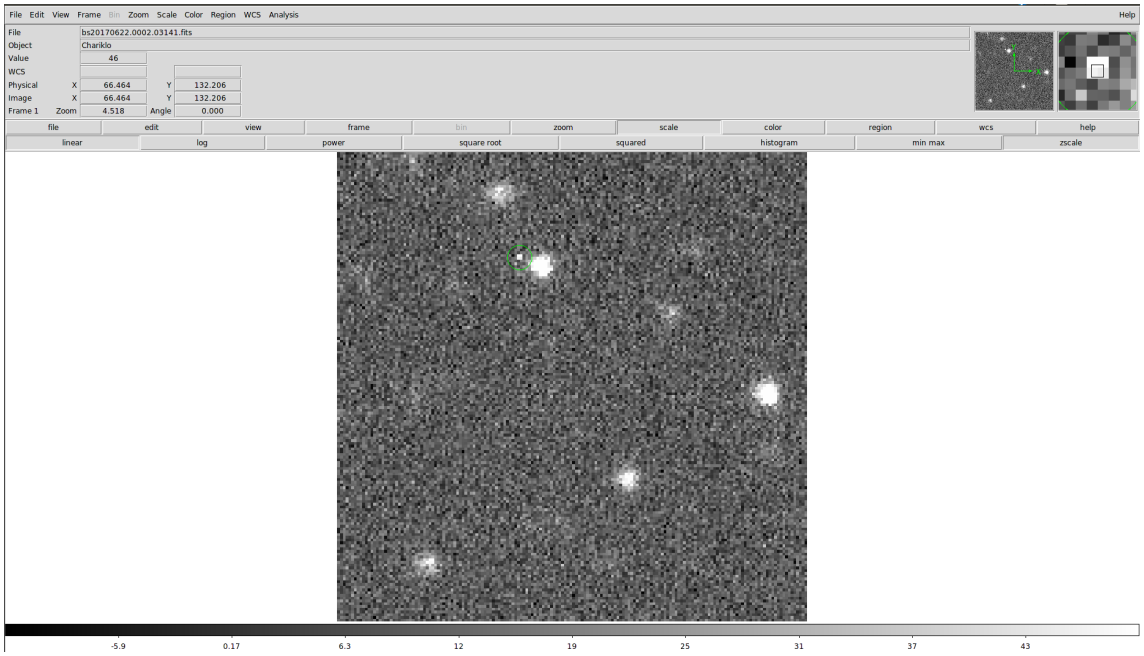

Figure 30: The frame of the cosmic ray responsible for the dip at ∼650s in the differential light curve as shown in Fig. 26 above. The green circle marks this occurrence.

2.2.7 Varda.20170629

2.2.7.1 LCO-CPT

The combined total of 603 BANZAI-reduced images from the three guide cameras ef02, ef03 and ef04, were run through the LCO pipeline respectively to undergo timing conversions into the required format for plotting. As mentioned before, the target field contains multiple comparison stars, but only two suitable comparison stars were chosen and both had bigger average optimal apertures than the target star. The LCO pipeline was supplied with a windows file containing three sets of coordinates (target and two comparison stars) and the maximum-magnitude-error-permitted parameter was altered to 0.3 magnitude. These inputs enabled calculation of all the instrumental magnitudes for the three stars of the various guide cameras respectively. The instrumental magnitudes for the target were, in the order of ef02, ef03 and ef04 guide cameras: -7.81, -7.89 and -7.8, and for the first comparison star, -9.58, -9.54 and -9.52, and lastly for the second comparison star the instrumental magnitudes were -9.19, -9.25 and -9.22. The average optimal apertures for the target star in the order of ef02, ef03 and ef04 guide cameras were 8.64, 8.34 and 7.68 binned pixels (5.82, 5.62 and 5.18 arcsec),12.88, 13.02 and 11.76 binned pixels (8.68, 8.78 and 7.93 arcsec) for the first comparison star, then the last comparison star had average optimal apertures of 11.78, 12.26 and 11.02 binned pixels (7.94, 8.26 and 7.43 arcsec). The differential light curve results from all three guide cameras were combined to construct a master differential light curve for this event. Fig. 31 is the resulting differential light curve for the target star and shows that no stellar occultation signature was observed.

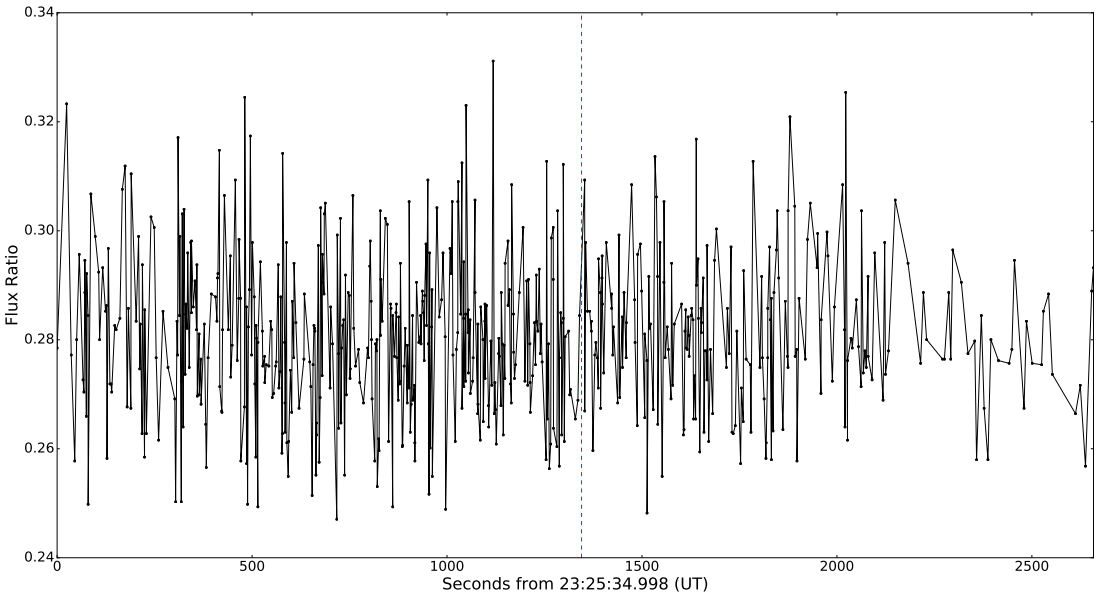

Figure 31: The LCO-CPT differential light curve showing the flux ratio versus time of the target star for the Varda.20170629 event. The dashed line represents the predicted midtime, 23:44:58 UT, for this event. The three telescopes have staggered starting times and therefore ending times which means the data points are sparse at the end of the differential light curve.

2.2.7.2 Shocndisbelief on the 74"

The datacube contained 6000 GPS-triggered images that were run through the SHOC pipeline. Bias and flat-fielding corrections using the photometric calibration frames taken on the given event night were done. The target field presented a total of three comparison stars that were chosen as

possible candidates to do differential photometry. From these three comparison stars, two were selected for differential photometry as the combined light curve resulted in the highest SNR of the target differential light curve. Only the results from these two comparison stars will be included here. An initial trial run of the SHOC pipeline produced average optimal aperture sizes of 7.14 binned pixels (4.34 arcsec) for the target star and 11.22 binned pixels (6.82 arcsec) for the first comparison star and 9.32 binned pixels (5.67 arcsec) for the second comparison star. However, fixed-aperture photometry was needed to have complete detection of all sources. The SHOC pipeline was supplied with a windows file containing the coordinates of all four point sources in the field, a fixed aperture size of 7 binned pixels (4.26 arcsec), the maximum-shift-for-centroid parameter was adjusted to 10 binned pixels and the maximum-frame-to-frame-drift was altered to 10 binned pixels. The instrumental magnitude for the target star was -8.83, -10.54 for the first comparison star and -9.92 for the second comparison star. Fig. 32 is the resulting plot of the differential light curve with no signs of the target star being occulted by Varda.

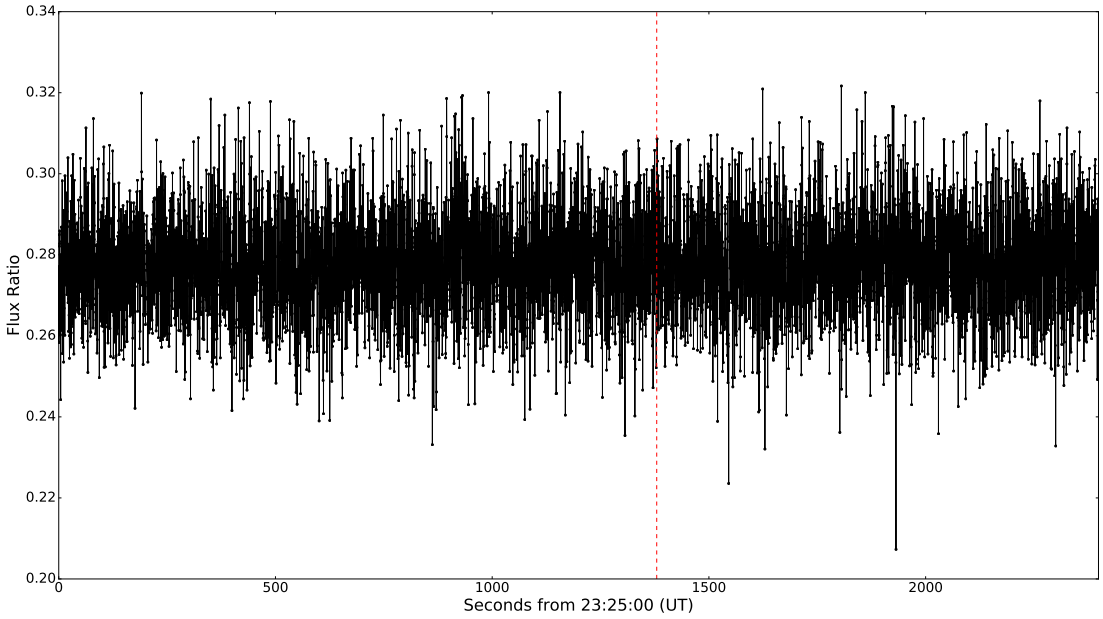

Figure 32: The Shocndisbelief differential light curve showing the flux ratio versus time of the target star for the Varda.20170629 event. The dashed line represents the predicted midtime, 23:48:00 UT, for this event.

2.2.8 $2014MU_{69}$.20170717

2.2.8.1 LCO-LSC

The combined total of 1056 BANZAI-reduced images was provided by the two guide cameras (ef06 and ef08) and were run through the LCO pipeline respectively. The large field of view of these guide cameras provides plenty of possible comparison star candidates, but they had to satisfy previously mentioned criteria before being used for differential photometry. Two stars were chosen as suitable comparison stars as both had larger average optimal aperture sizes than the target star. The LCO pipeline was supplied with only a windows file containing three sets of coordinates (target and two comparison stars) and was able to calculate all instrumental magnitudes for the three stars for each guide camera respectively. The second comparison star was responsible for producing the highest SNR for the differential light curve and hence only the results from this comparison star was noted here. The average optimal aperture for the target star was 16.58 binned pixels (11.17

arcsec) and 14.14 binned pixels (9.53 arcsec) for guide camera ef06 and ef08. The comparison star had average optimal apertures of 17.84 and 18.92 binned pixels (12.02 and 12.75 arcsec) for guide cameras ef06 and ef08. The instrumental magnitudes for the target star in order of guide cameras ef06 and ef08 were: -11.84 and -11.7, and for the comparison star -12.18 and -12.03. The results from the two guide cameras were combined to construct a master differential light curve for this event. Fig. 33 is the resulting differential light curve for the target star with no indication of a stellar occultation signature.

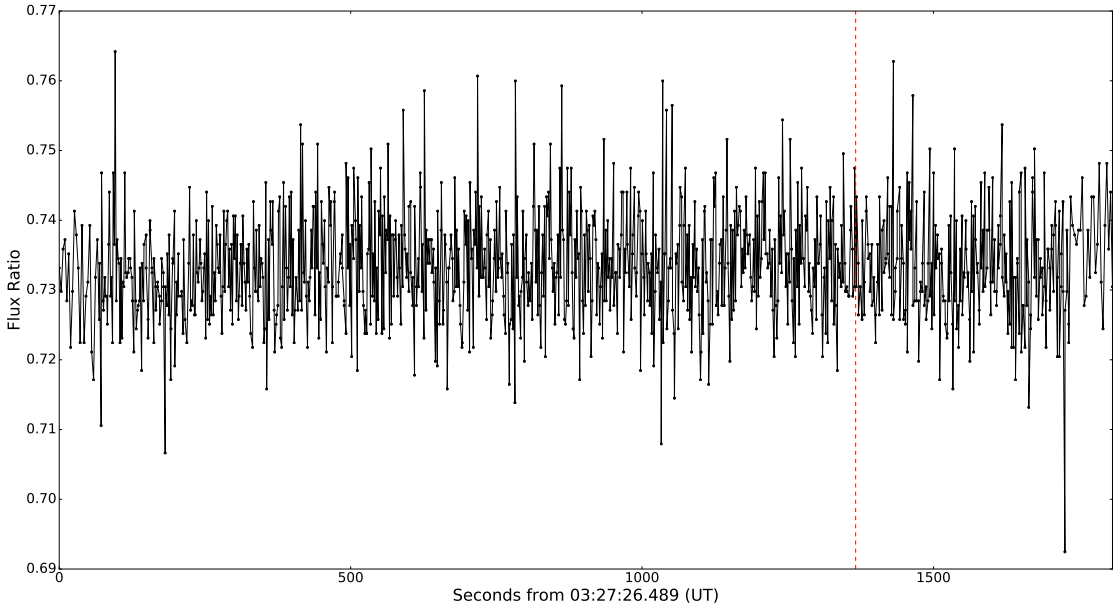

Figure 33: The LCO-LSC differential light curve showing the flux ratio versus time for the $2014MU_{69}$ event. The dashed line represents the predicted midtime, 03:50:13 UT, for this event. The two telescopes have staggered starting times and therefore ending times which means the data points are sparse at the end of the differential light curve.

2.2.9 Chariklo.20170723

2.2.9.1 LCO-LSC

Due to strong winds reaching telescope limits, only 219 images were taken in total by the two guide cameras, ef06 and ef08. Observational data was discontinued around 05:30 UT with the predicted midtime being scheduled for 05:54:48 UT. Hence only a couple of data frames were taken on the two guide cameras at LSC. The total 219 BANZAI-reduced images from the ef06 and ef08 guide cameras were run through the LCO pipeline respectively. Only a single, on-chip comparison star was suitable to be a comparison star satisfying all of the necessary criteria. The LCO pipeline was supplied with a windows file containing a pair of coordinates (target and the comparison star), an adjusted maximum-shift-of-the-centroid-box parameter of 10 pixels and a changed maximum-frame-to-frame-drift-of-the-centroid-box parameter of 10 pixels. All of the instrumental magnitudes for both stars from each guide camera were calculated respectively. The average optimal aperture for the target star was 21.08 and 18.7 binned pixels (14.21 and 12.60 arcsec) for guide cameras ef06 and ef08 with the comparison star's average optimal apertures as 22.84 and 21.02 binned pixels (15.39 and 14.17 arcsec). In the order of ef06 and ef08 guide cameras, the instrumental magnitude for the target star was -12.21 and -12.04, with -12.08 and -11.93 for the comparison star. The results from the two guide cameras were combined to produce a master differential light curve for

this event. Fig. 34 is the resulting differential light curve for the target star and shows no signs of a stellar occultation being observed for this event.

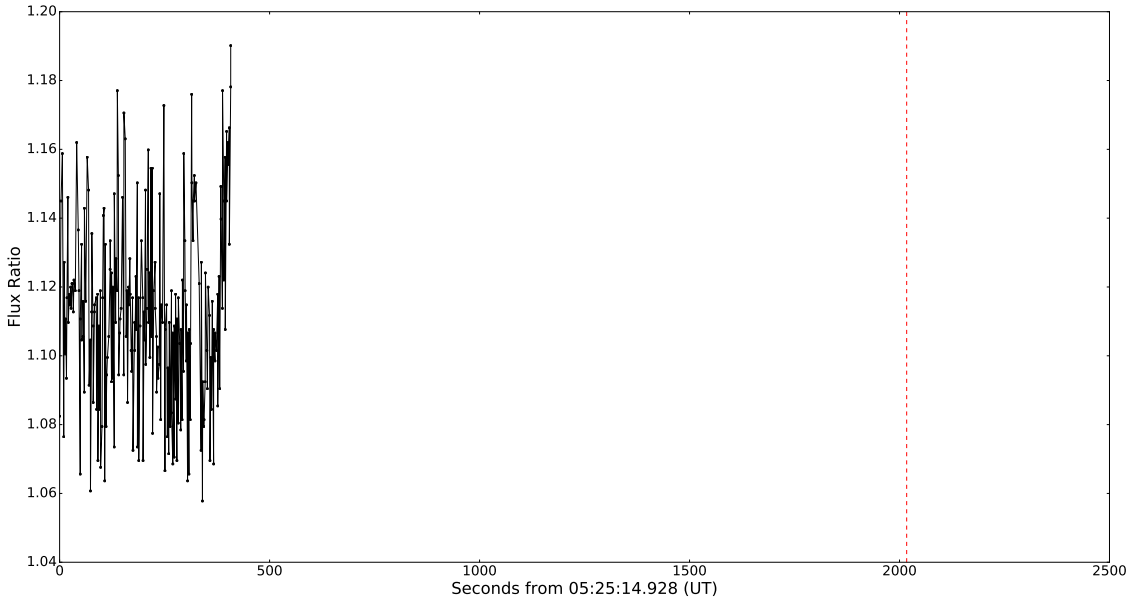

Figure 34: The LCO-LSC differential light curve showing the flux ratio versus time for the target star of the Chariklo.20170723 event. This event was stopped due to wind speed limits being reached at the telescopes long before the predicted midtime, 05:58:52 UT, which is represented by the dashed line for this event.

3 Results

The results from the all of the events include various calculations. Hence, each of these individual calculations are discussed separately in the following sections. Each subsection includes a discussion on how the calculations were made, using the Orcus event as a demonstration. After using the Orcus event as an example to explain each of the calculations, the same calculation methodology is applied to the remaining events. If a specific event deviates from the "general" methodology it is discussed separately in this subsection. At the end of each subsection, a table is included to summarize the results for all of the events for the given calculation.

3.1 Normalized light curves

Identifying a positive detection of a stellar occultation can only be described as comparing the extent of signal deviation to the signal equilibrium. When an occultation of the target star does occur, its light is essentially "turned off" during this occulting period, that is, the signal drops to the same value as that of the background, where the background includes the signal from the occulting body (and perhaps surrounding satellite(s)) as defined by the background fraction in Eq. 5 below. The normalization of the event's resulting differential light curve would be done using the following equation:

$$\mathrm{F}_n = \begin{cases} \dfrac{\mathrm{F}_d - (\mathrm{bf} \times \mathrm{fs})}{(1 - \mathrm{bf}) \times \mathrm{fs}} \ , & \text{Occultation} \quad (4a) \\ \dfrac{\mathrm{F}_d}{\overline{F}_d} \ , & \text{No occultation} \quad (4b) \end{cases}$$

where F_n is the normalized flux and F_d is the differential flux. The background fraction, bf is defined as

$$\text{bf} = \frac{\text{Occulted Signal}}{\text{Unocculted Signal}} \ , \tag{5}$$

and the full scale, *fs*, is the mean of the unocculted signal or also known as the baseline. However, if the event were a miss i.e. if the differential light curve were a flat, straight line, the normalization is done by using Eq. 4b where $\overline{F}_d$ is the mean of the differential flux's baseline well outside of the expected occultation region.

An important calculation that is directly made from a normalized light curve, whether it was done with Eq. 4a or 4b, is the SNR. This ratio tells how the signal from the target star compares to that of the noise. The preferred SNR value usually depends on the scientific goal for each event but to detect a stellar occultation by a solid body, it is usually on the orders of tens and in some cases even less than 10.

The SNRs for all of the events were determined in the following manner:

$$\text{SNR} = \left(\frac{\overline{F}_{n_b}}{\sigma_{\overline{F}_{n_b}}} \right) \times \sqrt{\frac{\left(\frac{d_s}{v}\right)}{\text{T}}} \tag{6}$$

where $\overline{F}_{n_b}$ is the mean of the normalized flux's baseline, $\sigma_{\overline{F}_{n_b}}$ is the standard deviation of the normalized flux's baseline, d_s is the distance scale which was chosen to be 10 kilometers and v is the occultation velocity. Including this previous variable puts a more physical measure on the SNRs over 10 kilometers in terms of measurement and is appropriate for measurements done close to the surfaces of bodies that lack an atmosphere. The cycle time, T, is the median integration time between data points and is therefore inherent to the observational data.

These calculations are implemented below on the Orcus.20170307 differential light curve.

3.1.1 Orcus.20170307

The Orcus.20170307 occultation event had a predicted geocentric midtime of 06:56:48±00:05:58 UT and was observed from 5 stations: the 0.6-m Astronomical Telescope of the University of Stuttgart (ATUS) at Sierra Remote Observatories (SRO), California; the 1-m Las Cumbres Observatory's telescope (ELP) at McDonald Observatory, Fort Davis, Texas; NASA's 3-m InfraRed Telescope Facility (IRTF) on Mauna Kea, Hawaii; the 0.6-m Southeastern Association for Research in Astronomy telescope (SARA-CT) at Cerro Tololo, Chile; and the 4.1-m Southern Astrophysical Research telescope (SOAR) on Cerro Pachón,Chile.

The occultation was detected at two of the five sites. With the observed midtime still being within the predicted midtime timing errors as noted in Table 1 above, suggests that the occultation observed at ELP seems to be that of Orcus. This, however was not the case at the IRTF as the observed midtime had a timing offset larger than the prediction timing error and resulted in the geometry suggesting that an occultation of a secondary star close to the target star was observed. The discrepancies in the timing offset and the geometry implies the predicted midtime to be suspect. Hence, with the uncertainty of an unknown secondary star being occulted, the differential light curve was normalized as shown in Eq. 4b.

The differential light curves as shown in the previous section for this event showed an obvious positive occultation, spanning over a pair of data points for LCO-ELP and many data points for IRTF-MORIS, which was discernible in the target and not in the comparison star. To follow here, is thus a discussion on the data analysis done on the normalized light curves for each of the two sites involved in the Orcus.20170307 event and follows here in order from the most Northern to Southern sites.

3.1.1.1 LCO-ELP

As the geometry suggested a flux contribution from an unknown secondary star, the residual flux prevents the observed flux from ever reaching zero during the occultation and, hence, was normalized using Eq. 4b from above. The two lower-flux data points were excluded in determining the mean of the baseline, which was 0.23 and the resulting normalized light curve plot is shown in Fig. 35.

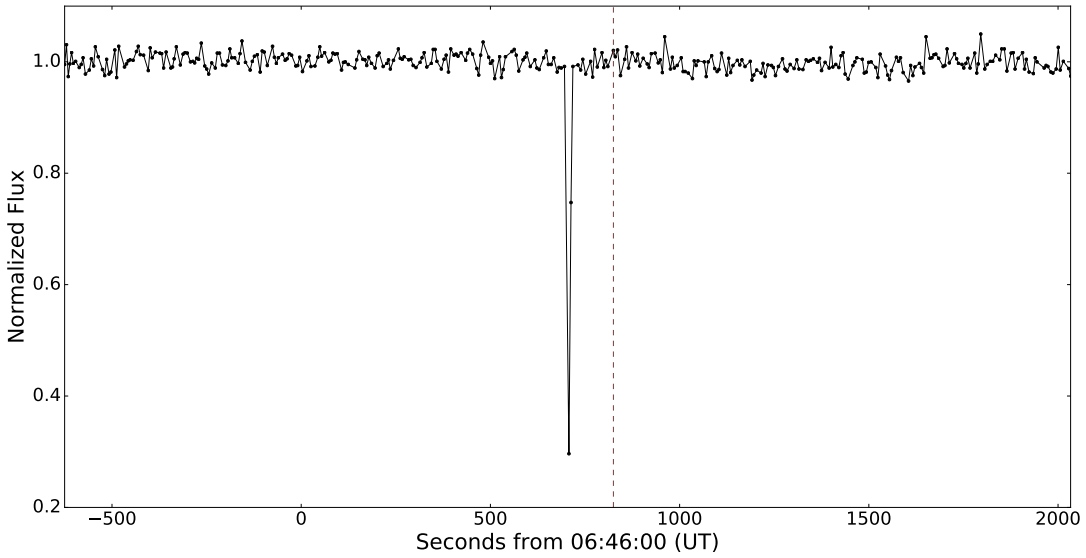

Figure 35: The LCO-ELP normalized light curve showing the normalized flux versus time for the target star for the Orcus.20170307 event. The dashed line represents the predicted midtime for this event, which was 06:59:45 UT. The exact offset from this predicted midtime will follow below.

Further analysis considers the noise of the baseline (the standard deviation) to be the most reliable error in flux. For this normalized light curve the standard deviation is 0.015. Note, that the results obtained here differ from that in Sickafoose et al. 2017 as the data analysis for the LCO data was done by another co-author (C. Zuluaga).

The accuracy on the range of times probed by a single exposure between consecutive data points is half of the exposure time, which is 1.25 seconds, but when calculated directly from the normalized light curve, the median cycle time is 5.906 seconds. This means that with an exposure time of 2.5 seconds, the median readout time is 3.406 seconds. The time recorded in the LCO header is at the start of the exposure and hence the midtime for that given exposure would be the time recorded in the header plus 1.25 seconds. The timing accuracy for that midtime would be ± 1.25 seconds and any excess time between two data point's timing accuracy range is deadtime.

Smaller errors can be derived on partially occulted data points, if instantaneous flux change is assumed: immersion occurred either between two exposures (assuming the first occulted data point reached zero flux) or occured in the same manner as with emersion where it is assumed that the partial-flux data point consists of a fraction of signal at either zero or one.

If it is assumed that the first occulted data point reached zero flux, instantaneous immersion would happen somewhere between the end of the last data point's exposure in the baseline and the start of the exposure for the first occulted data point. Thus between 698.16 and 707.48 seconds from 06:46:00 UT. Instantaneous immersion would thus occur at 702.82±4.66 seconds from 06:46:00 UT. This is during the deadtime between the two consecutive data points and therefore the error on the instantaneous immersion is half of the deadtime.

Looking at the light curve in the Fig. 35 above, the emersion time would have happened during the exposure that started at 712.96 seconds from 06:46:00 UT as the data point is a partial flux value. In order to accurately determine the instantaneous emersion time, the amount of time spent at zero flux and full flux needs to be brought into consideration.

On emersion, the data point was started at 712.96 seconds and had a signal of 0.747 (±0.015) in flux. This indicates that the time spent at 0, zero flux, was between 0.238 and 0.268 of the integration, while the corresponding time spent at full flux was between 0.732 and 0.762 of the integration. This returns an emersion time of 712.96+(1-0.747)×2.5=713.59 seconds (start of the integration + the fraction spent at zero flux) with a range from 713.56 and 713.63 seconds (712.96+0.238×2.5 to 712.96+0.268×2.5). Thus this equated to ± 0.037 seconds error around the instantaneous emersion time at 713.59 seconds from 06:49:00 UT.

With respect to Orcus, the relative velocity of the star was 26.316 km.s^{-1}. This equates to a chord length between 6.08 seconds (707.48 to 713.56) and 15.47 seconds (698.16 to 713.63) or 283.56±123.56 kilometers. The error on the chord length is so large because of a large recorded deadtime between the last baseline data point and the occulted data point of 9.3 seconds.

The predicted midtime for this event was 06:59:45±00:05:58 UT. Subtract the start of the cube, 06:46:00 UT, and this results to the predicted midtime of 825±358 seconds from 06:46:00 UT. By using the chord lengths reported above the observed midtime was at 708.21±2.31 seconds from 06:46:00 UT. Which equates to an offset between 477.10 seconds (705.90 to 1183) and 243.52 seconds (467 to 710.52) or 360.31±116.79 seconds from 06:59:45±00:05:58 UT. The offset in midtime equates to a distance offset of 9481.92±3073.45 kilometers. The significance of this would be explored in the discussion and conclusions section.

The median cycle time was 5.906 seconds for this event and thus the SNR over 10 kilometers for this normalized light curve is calculated using Eq. 6. The SNR is 17.16.

3.1.1.2 IRTF-MORIS

Now following the same method as with the LCO-data above, the normalized light curve from the IRTF was determined by using Eq. 4a above. This assumes that the normalized light curve does go to zero flux even though the specifics surrounding the actual occulted target star had some uncertainties. The mean of the baseline of the differential light curve is 1.61, which excluded the occulted data points and a background fraction of 0.71. With these values known the normalized

light curve is shown in Fig. 36 and for more detail a zoomed-in plot is shown in Fig. 37.

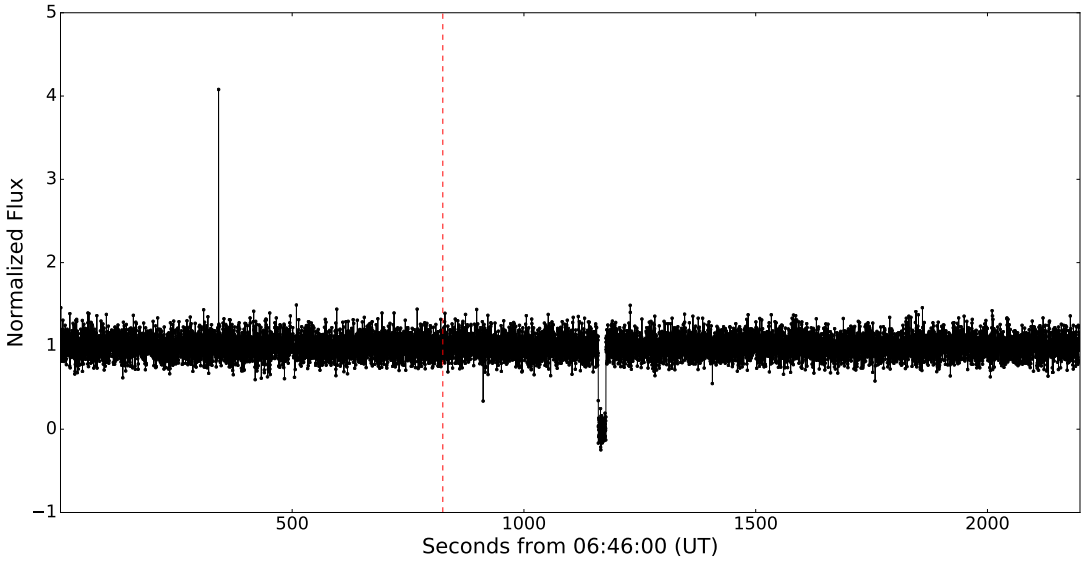

Figure 36: The IRTF-MORIS normalized light curve showing the normalized flux versus time for the target star for the Orcus.20170307 event. The dashed line represents the predicted midtime for this event, which was 06:59:45 UT. The exact offset from this predicted midtime will follow below.

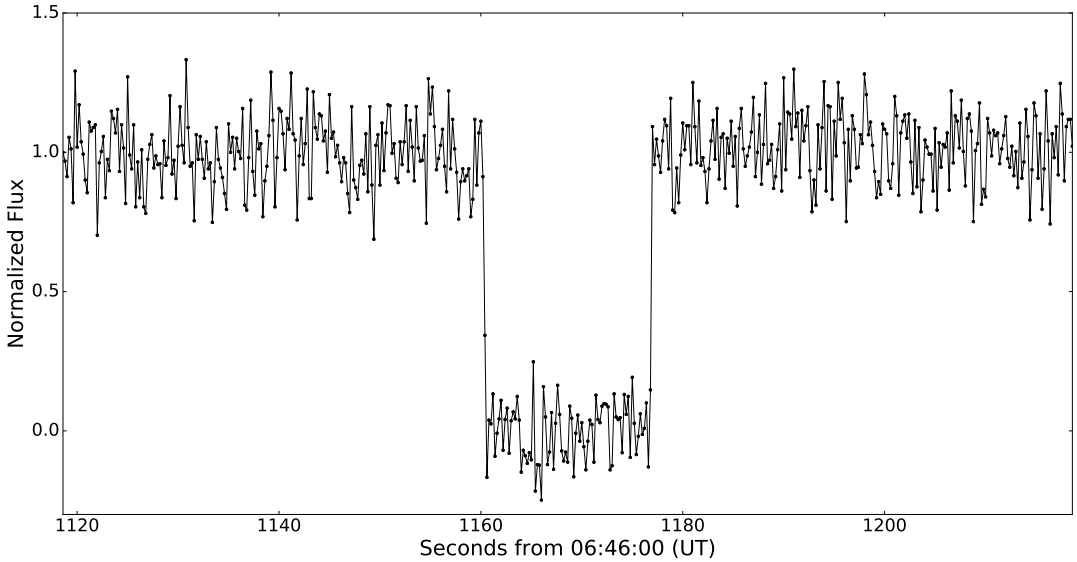

Figure 37: A zoomed-in plot of the IRTF-MORIS normalized light curve for the Orcus.20170307 event to show more detail of the occultation event.

As seen in Fig. 37, there was one partially-immersed data point. Hence the instantaneous immersion occurred somewhere between 1160.20 and 1160.40 seconds from 06:46:00 UT. The standard deviation of the normalized light curve is 0.12, which is used to determine the immersion time. The timing accuracy for anything occurring within an exposure between consecutive data points is half of the exposure time which was 0.1 seconds.

Now, the amount of time spent at full flux and zero flux was brought into consideration with the data point being centered at 1160.30 seconds and had a signal of 0.343 (±0.12) in flux. Time spent at zero flux was between 0.537 and 0.777 of the integration, whilst the corresponding time spent at full flux was between 0.223 and 0.463 of the integration. This equates to an immersion midtime of 1160.3+(0.343×0.2)=1160.37 seconds (start of the integration + the fraction of time spent at full flux). The midtime ranges between 1160.34 seconds and 1160.39 seconds (1160.3+0.223×0.2 to 1160.3+0.463×0.2) from 06:46:00 UT. Supplying a timing error of ±0.03 seconds, immersion occured at 1160.37±0.03 seconds from 06:46:00 UT.

The instantaneous emersion happened between the two data points (the last one at 0 flux and the first one at 1 flux). Based on the flux error determined for the instantaneous immersion, the timing would be the same for the emersion point, but now there were two points to consider, hence again, the error doubles. The instantaneous emersion was therefore between 1176.80 and 1177.00 seconds from 06:46:00 UT. Including the timing error calculated for the instantaneous immersion time the instantaneous emersion time was at 1176.90±0.06 seconds from 06:46:00 UT.

With respect to Orcus, the relative velocity of the star was 26.271 km.s^{-1}. With this, the chord length was determined to be between 16.44 seconds (1160.40 to 1176.84) and 16.62 seconds (1160.34 to 1176.96) or 434.26±2.36 kilometers.

The predicted midtime for this event was 06:59:45±00:05:58 UT. Subtract the start of the cube, 06:46:00 UT, and this results in the predicted midtime of 825±358 seconds from 06:46:00 UT. By using the chord lengths reported above the observed midtime was at 1168.64±0.07 seconds from 06:46:00 UT. Which equates to an offset between 701.71 seconds (467 to 1168.71) and 14.43 seconds (1168.57 to 1183) or 358.07±343.64 seconds from 06:46:00 UT. The offset in midtime equates to a distance offset of 9406.86±9027.77 kilometers. The significance of this will be explained in the discussion and conclusions section.

The median cycle time was 0.2 seconds for this event and thus the SNR over 10 kilometers for this normalized light curve is calculated using Eq. 6 to be 38.97.

3.2 Normalized light curve results for all events

The differential light curves produced by the various pipelines are normalized in the same manner as discussed for the Orcus event above, i.e. rescaling flux to 1 by using the mean of the baseline.

The SNRs were determined for all of the events whether reduced, bias corrected or unreduced. The reason for considering all cases is because the highest SNR is not always produced by the reduced data, as sometimes doing the reductions is found to add noise. For LCO data the SNRs were only determined for the reduced data as the data was already fully reduced by their pipeline. Table 4 shows all of the SNRs as calculated with Eq. 6 for the various cases and events.

Table 4: SNR results for all events.

Event	Instrument	Reference Distance (km)	SNR					
			Unreduced		Bias Corrected		Reduced	
			Result	n_{data}	Result	n_{data}	Result	n_{data}
Pluto.20160719	SHOCA	60	108.55	7997/7998	106.90	7995/7998	109.10	ALL
Haumea.20170121	SHOCA	10	0.27	184/295	0.36	186/295	0.84	198/295
	SHOCD	10	7.03	275/520	7.01	273/520	4.29	462/520
Orcus.20170307	LCO-ELP GC	10	-	-	-	-	17.16	ALL
	MORIS	10	33.75	ALL	37.65	ALL	38.97	ALL
Ixion.20170505	LCO-LSC GC	10	-	-	-	-	81.40	ALL
$2014MU_{69}$.20170603	LCO-CPT GC	10	-	-	-	-	17.86	ALL
	SHOCD	10	38.38	ALL	38.71	ALL	38.76	ALL
Chariklo.20170622	SHOCD	10	28.59	ALL	-	-	29.00	ALL
Varda.20170629	LCO-CPT GC	10	-	-	-	-	7.04	ALL
	SHOCD	10	21.66	ALL	21.59	ALL	21.76	ALL
$2014MU_{69}$.20170717	LCO-LSC GC	10	-	-	-	-	45.76	ALL
Chariklo.20170723	LCO-CPT GC	10	-	-	-	-	19.56	ALL

SHOCA - Shocnawe
SHOCD - Shocndisbelief
LCO GC - The LCO 1 meter telescopes's respective FLI guide cameras

3.3 Statistical outliers

The statistical significance of every data point from a given dataset could be tested by using Poisson statistics. This associates a detection limit with every data point and identifies any statistically significant outliers present in the dataset.

Hence, it is assumed that the data were normally distributed and the upper limits are placed. This is demonstrated by the Orcus event.

3.3.1 Orcus.20170307

3.3.1.1 LCO-ELP

This dataset had 364 data points (excluding the two-point occultation) with a standard deviation of 0.015. Therefore, 0.02 individual points should have a value beyond 4σ from the mean and zero such points were found. Hence this verifies that the assumption made on the statistical distribution of the data being normally distributed is correct.

3.3.2 IRTF-MORIS

This dataset had 10914 data points (excluding the occultation and cosmic ray); therefore, 0.69 individual points should have a value beyond 4σ from the mean and 3 such points were found. It was expected to find 0.1 and 0.00002 individual points to have values beyond 5σ and 6σ from the mean respectively. Only one data point was found to be beyond 5σ from the mean and zero data points were found beyond 6σ from the mean. Hence the statistical outliers detected at both the 4σ and 5σ standard deviation levels are more than expected from Poisson statistics and suggests further investigation of those frames or an error in the data analysis. Fig. 38 shows these three outliers.

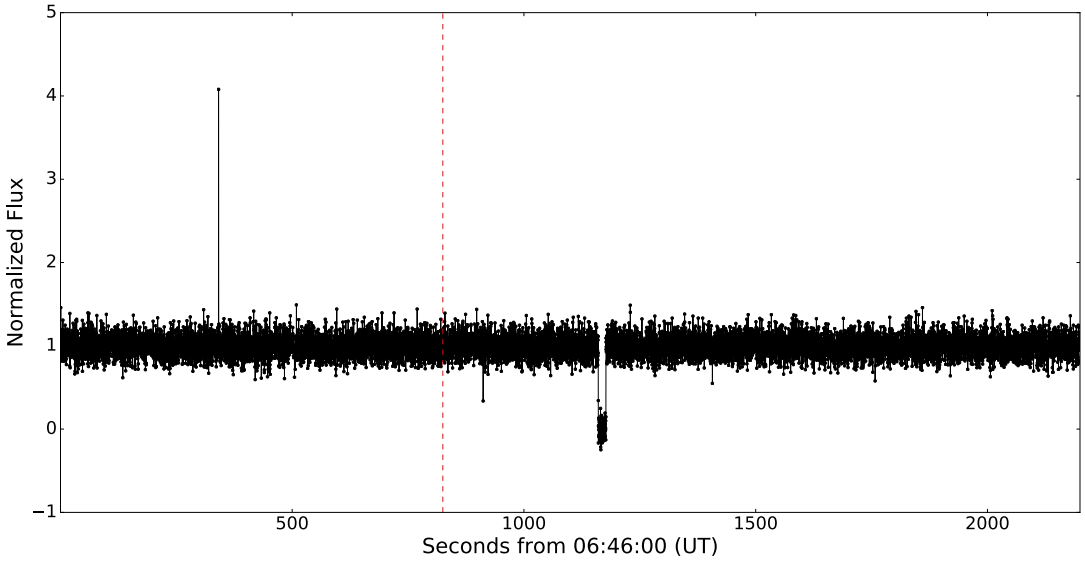

Figure 38: IRTF-MORIS normalized light curve for the Orcus.20170307 event showing the statistically determined outliers for this dataset. The data that have values beyond 4σ and 5σ from the mean are identified.

3.3.3 Statistical outliers for all events

Table 5 shows the statistical outliers found at various standard deviation levels as mentioned above for all of the events.

Table 5: Observed statistical outlier results for all events.

Event(Instrument)	$\mathbf{n_{data}}$	σ	**Observed statistical outliers**			
			$\mathbf{3\sigma}$	$\mathbf{4\sigma}$	$\mathbf{5\sigma}$	$\mathbf{6\sigma}$
Pluto.20160719 (Shocnawe)	7998	0.03	56	14	2	2
Haumea.20170121 (Shocnawe)	198	0.70	5	2	1	1
Haumea.20170121(Shocndisbelief)	462	0.11	9	4	2	1
Orcus.20170307(LCO-ELP GC)	364	0.01	3	0	0	0
Orcus.20170307(MORIS)	10914[a]	0.04	43	3	1	0
Ixion.20170505(LCO-LSC GC)	1499	0.01	2	0	0	0
2014MU69.20170603(LCO-CPT GC)	882	0.02	1	0	0	0
2014MU69.20170603(Shocndisbelief)	26998	0.06	71	7	1	1
Chariklo.20170622(Shocndisbelief)	7560	0.05	33	3	2	2
Varda.20170629(LCO-CPT GC)	603	0.05	3	0	0	0
Varda.20170629(Shocndisbelief)	5998	0.05	24	2	0	0
2014MU69.20170717 (LCO-LSC GC)	1056	0.01	11	1	1	0
Chariklo.20170723 (LCO-CPT GC)	219	0.02	0	0	0	0

LCO GC - The LCO 1 meter telescopes's respective FLI guide cameras.
[a] Excluding the occultation and cosmic ray.

3.4 Optical depth

The optical depth (τ) was calculated by measuring the flux for each event and applying the following:

$$I = I_0 \exp -\frac{\tau}{\mu}, \tag{7}$$

$$\tau = -\mu \ln\left(\frac{I}{I_0}\right) \tag{8}$$

where I is the incident flux and I_0 is the transmitted flux received from the target star. Essentially, this fraction of incident flux to transmitted flux is equivalent to the normalized light curve data since the mean value of the differential light curve has been fixed at 1.

The cosine of the ring opening angle, μ, describes the angle at which this event was observationally viewed at the time of the event. In most cases there are no known ring systems present around the body and the pole orientation is also most likely to be unknown. In the latter cases, μ is chosen to be equal to 1, and therefore, essentially does not contribute to the optical depth calculations. However, in the cases where ring systems are known to exist, like Chariklo, μ=1 indicates that a ring system is viewed fully open and μ=0 indicates that a ring system is viewed edge on. The minimum, maximum and average line-of-sight optical depth limits were calculated for each event. Table 6 summarizes the optical depth results for all of the events.

Table 6: Line-of-sight optical depth limits for all events.

Event	Instrument	Optical Depth			
		Ave.	Med.	Max.	3σ
Pluto.20160719	shocnawe	0.022	0.017	0.183	0.084
Haumea.20170121	shocnawe	0.660	0.330	4.354	1.133
	shocndisbelief	0.096	0.054	0.629	0.412
Orcus.20170307	LCO-ELP GC	0.020	0.011	1.216	0.045
	MORIS	0.033	0.024	0.455	0.112
Ixion.20170505	LCO-LSC GC	0.008	0.007	0.024	0.026
2014MU69.20170603	LCO-CPT GC	0.019	0.016	0.070	0.072
	shocndisbelief	0.044	0.037	0.254	0.188
Chariklo.20170622	shocndisbelief	0.040	0.33	1.096	0.165
Varda.20170629	LCO-CPT GC	0.040	0.33	0.128	0.168
	shocndisbelief	0.038	0.032	0.261	0.152
2014MU69.20170717	LCO-LSC GC	0.008	0.007	0.057	0.033
Chariklo.20170723	LCO-CPT GC	0.019	0.017	0.051	0.077

LCO GC - The LCO 1 meter telescopes's respective FLI guide cameras

3.5 Deadtime calculations for LCO data

The MORIS and SHOC instruments were built to observe stellar occultations with very accurate cycle times and minimal deadtime. The non-standard LCO observations make use of the guide cameras and thus are not as reliable in terms of timing. Here, the median deadtime for each LCO instrument at every site is calculated. In the case of the LCO guider cameras, when multiple instruments were used, the results include the combined median deadtime for different combinations of the guider cameras at the specific site. The median deadtime for the Chariklo.20170622 event was determined because of the time-triggering-mode used during this event. This event was not externally triggered by GPS but internally triggered using the time from the local computer clock, hence the timing of this event was not as accurate as the other events on the SHOC instruments.

Table 7: Deadtime results for LCO events

Event	Site	Instrument	t_{exp} (s)	Deadtime (s)			Combined cycle times (s)*			
				GC 1	GC 2	GC 3	GC 1+2	GC 1+3	GC 2+3	GC 1+2+3
Orcus.20170307	LCO-ELP	GC (ef01)	2.5	Min: 1.466 Med: 3.406 Max: 16.452	-	-	-	-	-	-
Ixion.20170505	LCO-LSC	GC (ef06, ef07, ef08)	(2, 2, 3)	Min: 1.145 Med: 1.240 Max: 3.681	1.142 1.240 2.568	1.149 1.25 3.887	0.002 1.666 4.254	0.002 1.976 5.364	0.001 1.95 5.364	0.001 1.113 5.364
2014MU69.20170603	LCO-CPT	GC (ef03, ef04)	(3, 3)	Min: Med: Max:	1.143 1.197 18.147	1.143 1.246 20.876	-	-	0.00 2.887 14.368	-
Varda.20170629	LCO-CPT	GC (ef02, ef03, ef04)	3.5	Min: 1.148 Med: 4.693 Max: 58.512	1.149 2.676 38.479	1.149 5.199 60.629	0.010 4.655 59.353	0.051 4.652 59.353	0.023 4.651 33.875	0.010 3.210 59.353
2014MU69.20170717	LCO-LSC	GC (ef06, ef08)	2.0	Min: 1.141 Med: 1.240 Max: 4.47	-	1.142 1.240 8.325	-	0.001 1.700 4.607	-	-
Chariklo.20170723	LCO-LSC	GC (ef06, ef08)	2.0	Min: 1.144 Med: 1.241 Max:6.201	-	1.166 1.241 14.004	-	0.003 2.032 7.693	-	-

t_{exp} - exposure time

GC - Guide camera

*The time differences calculated between the consecutive data points of the combined light curves from the various LCO telescopes. The normalized flux and time arrays of the respective LCO cameras were combined into respective master arrays for the combined normalized flux and the combined times. The time difference between time various entries in the master time array was determined. This was done for different combinations of the guider cameras to give an idea of what combination of guider cameras provide the best combined cycle times for a given exposure time. As some individual cameras have very long median deadtimes associated with them.

4 Discussion and Conclusions

The aim of the work was to present the telescopes, instruments and data analysis pipelines that are used for the SAAO stellar occultation program together with the results from stellar occultations by bodies in the outer Solar System during the period of July 2016-2017. The arrival of the SHOC instruments for use on the 74-in, the 40-in and the 1.0-m SAAO telescopes, enabled stellar occultations to be observed locally, which was not the case prior to SHOC. But even with the correct equipment for the job, the actual detection of a stellar occultation has proven to be quite a rare occurrence. With the inclusion of a single IRTF-event and several LCO-events, in addition to the already proposed SAAO-events, only a single stellar occultation was detected out of a total of 22 proposed stellar occultations. Since 1988, the first definitive detected stellar occultation by the TNO Pluto, only about a couple of dozens of stellar occultations have been successfully recorded, making non-detections the norm in stellar occultation events. The (expected) poor success rate should not diminish the results that were obtained during this period, as any new information gathered is gained and any additional information builds on present information. All of the information gathered in this thesis would not have been possible without optimizing the SHOC pipeline (as developed by Dr. Marissa Kotze) for stellar occultations done by the SAAO. Therefore, an important result is the availability of three data pipelines (see section 2.1) that are optimized and developed for a well-established stellar occultation observing program on SAAO, LCO and the IRTF telescopes. The data analysis information gathered by these pipelines will be discussed here, followed by the conclusions.

4.1 Orcus.20170307 event

As reported in section 2.2, two chords were measured for this event. One was measured at ELP with a length of 283.56±123.56 kilometers and a midtime offset from the prediction of 360.31±116.79 seconds. The chord measured at the IRTF was 434.26±2.36 kilometers and had a midtime offset from the prediction of 358.07±343.64 seconds. The midtime offsets from the prediction recorded at both sites could suggest an occultation by Orcus' satellite, Vanth. With a recorded semimajor axis of 9030±89 kilometers (e.g. Carry et al., 2011) and with an almost completely frontal view of the system, the stellar occultation is suggesting to have been that of Vanth. Previous thermal measurements derived approximate sizes of 900 and 280 kilometers (Brown et al., 2010) for Orcus and Vanth, with a more recent publication (Fornasier et al., 2013) declaring sizes of 917±25 kilometers and 276±17 kilometers, respectively.

The chord length derived at the ELP is on the order of Vanth's recorded size estimates and thus a lower limit is placed on this satellite's size of 283.56±123.56 kilometers even though the extent of the error does not enable a better constraint on the body's size to previous observations made. The chord length derived at the IRTF, however, is too large for Vanth and hence this chord is assumed to belong to Orcus, placing a lower limit on its diameter of 434.26±2.36 kilometers. While this seems to be the solution for the recorded chord lengths, there are a few contradictions: if Orcus was observed at the IRTF why is there such a large timing offset from the predicted midtime and why was an occultation of Vanth observed at ELP when Vanth's known location at the time was South of Orcus? A solution to likely confirm these discrepancies in both timing and geometry is that of a secondary star situated within close proximity of the target star, the combined center of light would have a slight offset (depending on its location relative to that of the target star) and could account for the Vanth occultation at the ELP and the large timing offset of the Orcus occultation

at the IRTF as well as the different occultation depths (the amount of flux blocked as a fraction of normalized flux) recorded at the IRTF and ELP. The various limits that were placed in this thesis for this event (diameter and optical depths) also suggests that no atmosphere was detected. A few scenarios to possibly explain the exact details behind these observations are currently under investigation (Sickafoose et al., 2017).

4.2 Haumea.20170121

Even though this dataset has not received as much attention as that of Orcus, a recent paper (Ortiz et al., 2017) was published during the preparation of the work presented in this thesis. A positive stellar occultation of this event observed the main body as well as a newly discovered ring feature. Looking at Fig. 12, a few symmetric dips in signal could be seen surrounding the predicted midtime and could be under suspicion of possible ring features. According to the corrected shadow path calculated in Ortiz et al. 2017 based on observations, an extrapolated shadow path might suggest the possibility of observing the ring structure (and not of the main body). Further investigation is therefore needed to verify or discard a possible ring occultation from Sutherland. The depths of these seemingly symmetric dips are suspect as the increasing background signal (due to sunrise) causes the signal from the sources, as well as the SNR, to decrease. But useful information was still extracted. The two deepest dips, at ∼678- and ∼993 seconds, equates to a separation distance of ∼4498 kilometers. Both of these dips are noted to be beyond the detection limit of 3σ, together with 4 other dips. However, these two dips were the deepest and line-of-sight optical depth results are 0.55 and 0.63 for the two respective dips. The single ring as reported by Ortiz et al. 2017 has an opacity of 0.5, width of 70 km and a radius of 2287 km. Even though the second suspect dip recorded in this dataset has a 2σ data point 9 seconds prior to it but equates to a ring width inconsistent with that reported by Ortiz et al. 2017. The results reported here do show similarities to the results reported by Ortiz et al. 2017.

4.3 SNR calculations

As mentioned before, stellar occultations push the lower limit of SNRs. As seen in Table 4 above, ∼70% of the highest SHOC SNRs are produced by fully reduced data as opposed to data that have not been bias subtracted and flat-fielded. Reduced data also resulted in the most usable frames, detecting point sources on more frames than the other cases. The Haumea event is the exception to the rule as it was observed close to sunrise which weakened the already poor incoming signal and caused many frames to be unusable due to high background counts.

Hence, it is suggested to take adequate calibration frames when doing these type of observations as it could be the difference between a detection or non-detection of a solid body when close to the lower SNR boundary. Each observation has a specific lower SNR boundary which is dependent on what has been detected during the stellar occultation for example a solid body, a ring system, an atmosphere etc. Table 8 is a reference table for the expected SHOC SNRs for the various exposure times (or cycle times in the case of the Chariklo.20170622 event), stellar magnitudes and instrument settings used throughout this thesis as noted in Table 1 and 3. Eq. 6 together with the online SHOC signal-to-noise ratio calculator[26] was used to determine the given values. This was only done for the SHOC events as it is the only system that has an online calculator in the mode used for the observations done in this thesis.

[26] http://shoc.saao.ac.za/SHOCsnr.html

Table 8: Reference SNRs for SHOC events

Event	Telescope	Instrument	Theoretical	Observational
Pluto.20160719	74-in	SHOCA	64.75	109.10
Haumea.20170121	74-in	SHOCA	3.85	0.84
	Lesedi	SHOCD	2.85	4.29
2014MU69.20170603	74-in	SHOCD	7.55	38.76
Chariklo.20170622	74-in	SHOCD	30.46	29.00
Varda.20170629	74-in	SHOCD	8.41	21.76

As can be seen from Table 8 above, most of the observational SNRs are higher than the expected, theoretical SNRs. The Chariklo.20170629 event resulted in a slightly lower SNRs than expected and could be due to bad weather or incorrect instrument settings. The Haumea.20170121 event was out of pointing limits on the 74-in and the data was taken close to sunrise resulting in a low SNR.

4.4 Statistical distribution of data

The distribution of a dataset is informative on how the data are spread around the mean value. A normal distribution was assumed for all the datasets, which is the accepted distribution when working with point sources. With the uncontrollable appearance of cosmic rays within the photometry apertures it skews the mean from its real value, the median of the point source is the more trusted value. However, cosmic rays are seldom seen within the photometric apertures and suggests statistical outliers to be the reason for spreading the data. The number of statistical outliers expected were calculated for each dataset and the majority of the datasets provided more outliers than were expected for a given standard deviation level.

The statistical distribution of the data is a measure of the quality of the observations made, as observational parameters could directly influence the number of outliers in the data, like seeing, binning and exposure time. If more and more outliers are detected on each sigma level, that is indicative of: incorrect observing parameters, too long exposures reaching the saturation limit of the detector, large binning causes incoming signal to be spread and thus causing non-detections, etc. Hence, adequate attention should be given to these parameters when observing stellar occultations as data gathered in an insufficient way can change the distribution of data from normal to non normal.

4.5 Optical depth

Optical depth measurements are indicative of how much material is possibly present in the system. With values « 1 indicating no substantial material and values » 1 indicating a substantial amount of material blocking incoming signal. For a body to have material within close proximity to its surface (e.g. atmosphere or rings) and effectively dimming the background star's flux, a large enough optical depth value must be recorded over a minimum of a single-point drop with consecutive multiple-point drops also being telling of a more prominent ring feature. Referring

back to Table 6 from the previous section, some general remarks would be that all of the optical depth values were calculated to be those of the line-of-sight optical depth as stated in section 3.4 and unlike normal optical depth takes the possible ring-orientation into consideration. Also, the maximum values have been confirmed to only be associated with one data point and even with a large distance scale involved, a single-point detection would be unlikely. However, with regards to the Haumea event, as mentioned in section 4.2 above, this event had two single-point dips with optical depths higher than the median optical depth for this event (0.33) and returned results that are very similar to those mentioned in Ortiz et al. 2017. So it could be possible to detect ring features whilst an occultation by the main body was missed. But besides the Orcus event, and the possible Haumea event, a single-point drop due to rings on missed events is unlikely. Surrounding data points (that did not share a high optical depth value) were investigated per frame together with the frame which was under suspicion and it was found that they showed no signs of abnormality and therefore no further investigations were done. Further investigations on these singular data points were not carried out as most of these events were misses. Further investigation would require geometry reconstruction for all of the events as the extent of the proximity to the nucleus is unknown, which is beyond the scope of the work done in this thesis.

The optical depth values provided in this thesis are diverse and - except for a few high values as shown in Table 6 - suggest that very little light-blocking material was observed while probing these various systems. If geometry reconstruction for the missed events were to commence in the future, all of the optical depths recorded in Table 6 are on the same order of what is to be expected around TNOs. For example, Chiron's proposed ring has an optical depth of around 0.7 to 1 (Ortiz et al., 2015), 0.4 and 0.06 for Chariklo's rings (e.g. Braga-Ribas et al., 2014). The optical depth results obtained here are comparable to optical depth limits from ground-based occultation data of Pluto's rings and are on the order of $< 5\times10^{-3}$ for rings with a width of 1500 km (e.g. Throop et al., 2015).

4.6 Deadtimes

Table 7 summarizes the effective deadtimes associated with the various guider cameras of the 1-m LCO telescopes at each site. The median readout times recorded are extremely important and should be contemplated when applying for LCO-time in proposals. A previously used deadtime of 2 seconds was the main reason for staggering the start times of the three cameras in order to not miss anything important during the 40-minute occultation window. However, often the observations were not centered on the predicted midtime, stopping the observations either ahead or behind of schedule on the account of the varying readout times for the guider cameras.

Observations are scheduled by supplying the start time of the observation and the number of frames that should be taken. Hence, for a 2 s exposure with the assumed 2 s readout time, 600 frames would need to be taken to fill the 40-minute occultation window. But after looking at Table 7 the range of deadtimes for each guide camera goes from as little as less than a second to as much as dozens of seconds.

The best estimate on which to base future observations is that of the median deadtimes. The LSC and CPT cameras were used a sufficient number of times that the average of the median deadtimes for each camera could be trusted and used to calculate the number of frames needed for a 40-minute observation as well as the corresponding exposure time. However, it is suggested

to confirm whether the target star is bright enough for shorter exposure times or not. Essentially, the results from this thesis can be used to increase the efficiency of planning and executing LCO observations and should help improve the scientific output.

4.7 Future plans

Future predictions are improved with each stellar occultation event, whether a detection was made or not, from the occultation frames and, if adequate, from the astrometric frames; however, that is not the work of this thesis. The ephemerides of the occulting bodies become more accurate with new observations and soon the success rate will increase as a result of our ever growing knowledge of these bodies and because of understanding the instruments that are involved in observing stellar occultations. Instruments can be optimized for stellar occultations probing the spatial environments in more detail than ever before. Even telescopes and instruments that were never intended for stellar occultations can now be used in new and creative ways (e.g. LCO), providing more possibilities to detect these events and increasing the chances of a successful observation. Even data pipelines can be further refined for their respective instruments to make sure scientists can get the most out of their data (e.g. as discussed here for the SHOC pipeline).

Future plans therefore include incorporating the newly-derived median deadtimes for the LCO guider cameras into proposals, to spend the allocated time given efficiently. The LCO pipeline could also be altered to re-include the reduction processes that the original SHOC pipeline provided, as the latter is only equipped to deal with datacubes and not individual images. Lastly, a general differential flux and plotting script needs to be incorporated into each pipeline. Although the SHOC pipeline does offer this functionality to its users, it provides differential photometry results in units of instrumental magnitude and compressed plots onto a portrait-layout, too small to show any significant details and not suggested for use in publications. A Python script was developed as part of this project but is not yet included in the data pipelines as it still needs event- and data-specific alterations to be made by the user.

The aim of the work presented here is to showcase the stellar occultations carried out at the SAAO together with any results that were gathered from these observations over a 12-month period in 2016-2017. Although more calculations are being done with differential light curves from the positively detected stellar occultation, i.e. atmospheric models, albedo, density, temperature and pressure profiles etc. (Sickafoose et al., 2017), this work has shown that the SAAO has a strong occultation observing program spanning a number of global locations. Access to these telescopes allows us to try a relatively large number of predicted occultation observations, which is particularly important given the large errors on TNO positions and thus low success rate. It is also clear from the results that different instruments return different data quality (with those that have been optimized for occultations being the best, as expected), but this work can be used to inform and improve future observations.

The work done here can also serve as a recommendation to perhaps utilize already existing telescopes and instruments in new ways for these observations in the future, therefore, increasing the number of telescopes and sites at our disposal. Whilst having instruments optimized for these observations ensures great data quality, they are location-fixed and therefore limit the number of events that can be observed. Rather obtain more assets that are spread across the globe than tying all future observations to a single location. As the success rate of stellar occultations improves

together with future predictions, better quality instruments could be developed for the sites that have the highest success rate or a whole new system could even be developed for a new site.

In conclusion, the stellar occultation community situated in various countries all over the world have established strong occultation programs capable of exploiting all of the observational opportunities available to them whilst collaborating with one another (e.g. Southwest Research Institute, Observatory of Paris and MIT), in a common goal to unravel the mysteries surrounding the small bodies of the Solar System.

Bibliography

Assafin, M., Camargo, J., Martins, R. V., et al. 2010, Astronomy & Astrophysics, 515, A32

Bannister, M. T., Kavelaars, J., Petit, J.-M., et al. 2016, The Astronomical Journal, 152, 70

Barnes, J. 1993, Beginner's Guide to Using IRAF: IRAF Version 2.10 (Associacion of Universities for Research in Astronomy)

Barry, M. T., Gault, D., Pavlov, H., et al. 2015, Publications of the Astronomical Society of Australia, 32

Barucci, M., & Peixinho, N. 2005, Proceedings of the International Astronomical Union, 1, 171

Bérard, D., Sicardy, B., Camargo, J., et al. 2017, arXiv preprint arXiv:1706.00207

Bosh, A. S., Person, M., Levine, S., et al. 2015, Icarus, 246, 237

Braga-Ribas, F., Sicardy, B., Ortiz, J., et al. 2013, The Astrophysical Journal, 773, 26

—. 2014, Nature, 508, 72

Brown, M., Ragozzine, D., Stansberry, J., & Fraser, W. 2010, The Astronomical Journal, 139, 2700

Brown, M. E. 2012, Annual Review of Earth and Planetary Sciences, 40, 467

Brown, M. E., & Batygin, K. 2016, The Astrophysical Journal Letters, 824, L23

Brown, T., Baliber, N., Bianco, F., et al. 2013, Publications of the Astronomical Society of the Pacific, 125, 1031

Bus, S. J., Buie, M. W., Schleicher, D. G., et al. 1996, Icarus, 123, 478

Carry, B., Hestroffer, D., Demeo, F. E., et al. 2011, Astronomy & Astrophysics, 534, A115

Coppejans, R. 2013, M.Sc. thesis, University of Cape Town

Coppejans, R., Gulbis, A., Kotze, M., et al. 2013, Publications of the Astronomical Society of the Pacific, 125, 976

Davis, A. B., Pasachoff, J., Babcock, B., et al. 2014, in American Astronomical Society Meeting Abstracts# 223, Vol. 223

Davis, L. E. 1999, in Astronomical Society of the Pacific Conference Series, Vol. 189, Precision CCD Photometry, ed. E. R. Craine, D. L. Crawford, & R. A. Tucker, 35

Davis, L. E., et al. 1994, IRAF Programming Group, NOAO, Tucson

Delsanti, A., & Jewitt, D. 2006, Solar System Update, 267

Elliot, J., Dunham, E., Bosh, A., et al. 1989, Icarus, 77, 148

Elliot, J., Olkin, C., Dunham, E., et al. 1995, Nature, 373, 46

Elliot, J. L., Person, M., Gulbis, A., et al. 2007, The Astronomical Journal, 134, 1

Elliot, J. L., Person, M. J., Zuluaga, C., et al. 2010, Nature, 465, 897

Fornasier, S., Lellouch, E., Müller, T., et al. 2013, Astronomy & Astrophysics, 555, A15

Fukugita, M., Ichikawa, T., Gunn, J., et al. 1996, The Astronomical Journal, 111, 1748

Greenfield, P., Hsu, J., & Hack, W. 2002, Space Telescope Science Institute

Grundy, W., Porter, S., Benecchi, S., et al. 2015, Icarus, 257, 130

Gulbis, A., Emery, J., Person, M., et al. 2015, Icarus, 246, 226

Gulbis, A., Bus, S., Elliot, J., et al. 2011, Publications of the Astronomical Society of the Pacific, 123, 461

Gulbis, A. A., Elliot, J., & Kane, J. F. 2006, Icarus, 183, 168

Jewitt, D., & Luu, J. 1993, Nature, 362, 730

Jewitt, D., Luu, J., & Chen, J. 1996, The Astronomical Journal, 112, 1225

Kenyon, S. J., & Bromley, B. C. 2004, The Astronomical Journal, 128, 1916

Lacerda, P., Jewitt, D., & Peixinho, N. 2008, The Astronomical Journal, 135, 1749

Leiva, R., Sicardy, B., Camargo, J., et al. 2017, The Astronomical Journal, 154, 159

Lellouch, E., Sicardy, B., De Bergh, C., et al. 2009, Astronomy & Astrophysics, 495, L17

Lellouch, E., Santos-Sanz, P., Lacerda, P., et al. 2013, Astronomy & Astrophysics, 557, A60

Lim, T., Stansberry, J., Müller, T., et al. 2010, Astronomy & Astrophysics, 518, L148

Lockwood, A. C., Brown, M. E., & Stansberry, J. 2014, Earth, Moon, and Planets, 111, 127

Nimmo, F., Umurhan, O., Lisse, C. M., et al. 2017, Icarus, 287, 12

Olkin, C. B., Young, L. A., French, R. G., et al. 2014, Icarus, 239, 15

Ortiz, J., Sicardy, B., Braga-Ribas, F., et al. 2012, Nature, 491, 566

Ortiz, J., Duffard, R., Pinilla-Alonso, N., et al. 2015, Astronomy & Astrophysics, 576, A18

Ortiz, J., Santos-Sanz, P., Sicardy, B., et al. 2017, Nature, 550, 219

Pasachoff, J. M., Souza, S. P., Babcock, B. A., et al. 2005, The Astronomical Journal, 129, 1718

Person, M., Elliot, J., Gulbis, A., et al. 2008, The Astronomical Journal, 136, 1510

Person, M. J., Bosh, A., Levine, S., et al. 2012, in AAS/Division for Planetary Sciences Meeting Abstracts, Vol. 44

Phillips, A. C., & Davis, L. E. 1995, in Astronomical Data Analysis Software and Systems IV, Vol. 77, 297

Porter, S. B., Spencer, J. R., Benecchi, S., et al. 2016, The Astrophysical Journal Letters, 828, L15

Rayner, J., Toomey, D., Onaka, P., et al. 2003, Publications of the Astronomical Society of the Pacific, 115, 362

Ruprecht, J. D., Bosh, A. S., Person, M. J., et al. 2015, Icarus, 252, 271

Santos-Sanz, P., Ortiz, J., Barrera, L., & Boehnhardt, H. 2009, Astronomy & Astrophysics, 494, 693

Santos-Sanz, P., French, R., Pinilla-Alonso, N., et al. 2016, Publications of the Astronomical Society of the Pacific, 128, 018011

Sicardy, B., Widemann, T., Lellouch, E., et al. 2003, Nature, 424, 168

Sicardy, B., Bellucci, A., Gendron, E., et al. 2006, Nature, 439, 52

Sicardy, B., Ortiz, J., Assafin, M., et al. 2011, Nature, 478, 493

Sicardy, B., Talbot, J., Meza, E., et al. 2016, The Astrophysical journal letters, 819, L38

Sickafoose, A. A., Bosh, A. S., Levine, S., et al. 2017, in AAS/Division for Planetary Sciences Meeting Abstracts, Vol. 49

Sickafoose, A. A., Bosh, A., Person, M., et al. 2015, in AAS/Division for Planetary Sciences Meeting Abstracts, Vol. 47

Souza, S. P., Babcock, B. A., Pasachoff, J. M., et al. 2006, Publications of the Astronomical Society of the Pacific, 118, 1550

Stansberry, J., Grundy, W., Brown, M., et al. 2008, University of Arizona Press, Tucson, AZ, 161

Stern, S., Bagenal, F., Ennico, K., et al. 2015, Science, 350, 292

Throop, H. B., French, R. G., Shoemaker, K., et al. 2015, Icarus, 246, 345

Vilenius, E., Kiss, C., Müller, T., et al. 2014, Astronomy & Astrophysics, 564, A35

Young, E., French, R., Young, L., et al. 2008, The Astronomical Journal, 136, 1757

Zuluaga, C., Person, M., Bosh, A., et al. 2011, in EPSC-DPS Joint Meeting 2011, 1866